MULTISCALE SIMULATION OF PLATELET AGGREGATION AND ADHESION UNDER FLOW IN 3D

A Dissertation

Presented to the Faculty of the Graduate School

of Cornell University

in Partial Fulfillment of the Requirements for the

Degree of

Doctor of Philosophy

By

Weiwei Wang

May, 2014

MULTISCALE SIMULATION OF PLATELET AGGREGATION AND ADHESION UNDER FLOW IN 3D

Weiwei Wang, Ph.D.

Cornell University 2014

Hemostasis is a self-defensive mechanism that prevents injured blood vessels from excessive bleeding. Its initiation is mediated by physical contact between flowing platelets, which are ellipsoid-shaped cell fragmentations from megakaryocytes, and the injured vessel surface, where the extracellular matrix is exposed to the blood flow. Such physical contacts—either short-term tethering, intermediate translocation (rolling) or permanent attachment, are primarily mediated by the interaction between GPIbα receptor presented on the platelet surface and immobilized von Willibrand Factor (vWF) recruited to the injured vessel surface.

GPIbα-vWF bond was known to exhibit kinetics that follows the classical Bell Model, where the slip bond behavior (bond lifetime reduces with increasing bond force) was well studied. Recently, a catch bond (bond lifetime increases with increasing bond force) regime was discovered and scientists believed that the combination of slip-catch behaviors is a better way to characterize the bond kinetics.

Other blood components, including red blood cells (RBCs) and vessel geometry also play important roles in the initiation of hemostasis. RBCs are known to be enriched at the center region of the vessel lumen due to their rheological properties. This results in a margination effect where smaller platelets are pushed towards the vessel wall. Such margination effect combines with the geometrical aspect of the thrombotic / stenotic region to enhance potential platelet-wall interaction once vessel injury occurs.

Platelet interaction with an injured vessel is a complicated physiological process and is challenging to study thoroughly in experiments, either *in vitro* or *in vivo*. Simulation studies overcome many experimental restrictions, such as environmental condition control, physiological prediction and multiscale observation. It has been more than a decade since computational methods were first applied to study hemostasis and the field is developing rapidly. In this thesis, two computational models are built, modified and applied. One focuses on the close interaction between platelets and a plane vessel wall mediated by GPIbα-vWF bond. The other model emphasizes hydrodynamic interactions between deformable RBCs, platelets, a developing thrombus and cylindrical vessel geometry. These models are validated by experimental results, either published *in vitro* results or new *in vivo* data. Author expects that by establishing these models to simulate the initiation of hemostasis, more quantitative insight of this delicate process can be revealed.

BIOGRAPHICAL SKETCH

The author was born in Hangzhou, Zhejiang Province, P. R. China on Nov. 23rd, 1985. He attended Zhejiang University in his hometown from 2004 to 2008 and graduated with a Bachelor of Science degree in Biological Science in June, 2008. During his four years of undergraduate study, he received "Outstanding Student Award", "Merit Student Award" and "Second Class Scholar for Excellent Student Award" with a major GPA of 3.97/4.00 (overall GPA rank: top 5%). He established a solid background not only in biology, but also in mathematics and computer programming. Beside course work, he devoted a lot to scientific research. He successfully applied to a scientific project in the National Undergraduate Innovation Program and received 10,000 RMB ($1,400) funding. He also spent a total of six months in exchange to UCLA and worked under Professor Samson A Chow's lab in the Department of Pharmacology.

Weiwei Wang joined Cornell University in the fall of 2008 and began his graduate study in the field of Biochemistry, Molecular and Cellular Biology (BMCB). In summer 2009, he transferred to the field of Biomedical Engineering to start his PhD project under the guidance of his advisor, Professor Michael R. King. His research is focused on the multiscale simulation of platelet aggregation and thrombus growth. He prepared for his the new field by perfectly completing two graduate level fluid mechanics classes. He received the Master of Science degree from Cornell University in August, 2011. Weiwei was a teaching assistant for the course "Biomedical Computation" in the fall semester, 2011. At this time, Weiwei has four first-author journal publications.

DEDICATION

This Thesis is dedicated to my parents Xianghuo Wang and Suzhen Wu for their selfless support all the way since the beginning of my PhD study.

Also, this thesis is dedicated to my friends who helped me and supported me for the past six years.

Finally, this thesis is dedicated to those who have strong wills, clear aims and are willing to spend great amount of effort to achieve them.

ACKNOWLEDGEMENT

Firstly, I would like to thank my research advisor Dr. Michael R. King for his long-term trust, support and guidance. For over four years, Dr. King has been a role model to me. He delivered knowledge, introduced concepts, gave numerous suggestions. Further, he evoked my motivation to the simulation and math modeling, created a research environment full of freedom. He showed me how to achieve work-life balance. Unlike some faculties, Dr. King focus more on development of students' future career rather than simply make students more productive. As a result, Dr. King would encourage me to take classes that will bring long term benefit, even in my last semester of PhD study.

Secondly, I would like to thank Dr. Nipa Mody for her detailed guidance and explanation of the simulation code, as well as the general ideas and significance of the project. I would also thank Dr. Johathan B. Freund for teaching me his computation methods in University of Illinois, Urbana Champaign and Dr. Thomas G. Diacovo for preparing animal data. These interactive collaborations are very important of my academic achievement.

Thirdly, I would like to thank my committee members Dr. Donald L. Koch and Dr. Joseph M. Scandura. Don has taught me two courses and his patience of answering my every question helped me develop a more thorough understanding about fluid mechanism. Joe's suggestions on research topics and his kind willingness to drive all the way from Manhattan to Ithaca to participate my A and B exams helped me a lot.

I would also thank Dr. Volker Vogt in Department of Molecular, Biochemistry and Genetics as well as Dr. Peter Doerschuk for recruiting me to Cornell as well as helping me make the field transfer smooth. I would thank Belinda Floyd for helping me about administrative and documentation stuff throughout the four and half years.

Last, I would like to thank Kuldeepsinh Rana, Jiahe Li, John P. Lindsey and all other former or current lab mates for creating such a joyful environment in the office and I really enjoy working with them for these years.

TABLE OF CONTESTS

LIST OF TABLES

LIST OF FIGURES

LIST OF SYMBOLS

Roman Letters

a particle radius

E_B bending modulus

F surface deformation tensor

f bond force

F_0 empirical parameter of units force · length used in the mathematical expression for short-range repulsive force

F_s drag force of fluid acting on platelet

G point-force singularity solution

H height of thrombus

$\mathbf{i}_r$ unit vector in the radial direction

$\mathbf{i}_\theta$ unit vector in the theta direction

K double-layer kernel

k_B Boltzmann constant

k_f forward rate constant used in Monte Carlo probability formulations (s^{-1})

k_{on} 3-D overall forward rate constant

k^0_{on} 3-D intrinsic forward rate constant

$k^0_{f,2\text{-}D}$ crosslinking forward rate constant (s^{-1})

k_r dissociation rate constant

k^o_r unstressed dissociation rate constant

$k^0_{I,off}$ Intrinsic dissociation constant for IG state

$k^0_{N,off}$ Intrinsic dissociation constant for NG state

l characteristic length

l_b equilibrium bond length

M bending moment

N in-plane tension tensor

N_{Re} Reynolds Number

n surface normal vector

$\dot{n}$ volume concentration of particles

p fluid pressure

$\bar{P}_n^m$ associated Legendre polynomials

Q surface transverse tensor

r radial distance in cylindrical coordinates

S Surface area

T torque

T temperature

t time

U translational velocity vector of a rigid particle

u fluid velocity

u_∞ bulk flow

W energy

X position vector

x position vector

x_b stressed bond length

x rectangular coordinate

y rectangular coordinate

y_I force compliance for intermediate state (slip bond)

y_N force compliance for native state (catch bond)

z rectangular coordinate

Greek Letters

δ minimum instantaneous particle-surface gap

ρ fluid density

γ reactive compliance

$\dot{\gamma}$ shear rate

Δt small time step

μ fluid viscosity

$\boldsymbol{\omega}$ rotational velocity vector of a rigid particle

ω angular velocity of a platelet flipping over a surface

θ angular position in cylindrical coordinates

Ψ stream function

Φ catch-slip ratio

φ orthonormalized null solutions

η_c collision efficiency

η_h hydrodynamic efficiency of collision

η_b binding efficiency of collision

$\boldsymbol{\sigma}$ stress tensor

σ_s spring constant

$\boldsymbol{\tau}$ viscous stress tensor

λ particle aspect ratio

$\boldsymbol{\Sigma}$ stress tensor associated with singularity solution **G**

$\boldsymbol{\zeta}$ position vector

$\boldsymbol{\phi}$ surface density

$\boldsymbol{\Gamma}$ eigenvector of the adjoint operator $\mathcal{K}^{\dagger}$

ε surface-to-surface separation based on the distance between the tips of the opposing surface roughness layers

χ empirical parameter of units length^{-1} used in the mathematical expression for short-range repulsive force

Special Symbols

∇ gradient operator

∇^2 Laplacian operator

$\mathcal{K}$ double-layer surface integral operator

$\mathscr{D}$ fluid domain of interest

CHAPTER 1: BRIEF VIEW OF SIMULATION IN HEMOSTASIS

Platelet adhesion and thrombus formation are critical, self-defensive mechanisms during the hemostatic response to prevent excessive blood loss during body injuries. When an unactivated, flowing platelet encounters an elevated local concentration of soluble platelet activators (e.g. thrombin or ADP, released at the site of vessel injury[1]), or physically contacts an exposed subendothelial layer through formation of surface receptor-ligand bonds (e.g. GPIbα-vWF-A1 bond[2]) it initiates translocation on an injured vessel wall, platelet activation, and ,subsequently, firm adherence to the vessel wall. Further development of a thrombus involves platelet-platelet interaction via GPIbα-fibrinogen/vWF bridging[3], as well as formation of a fibrin network[4]. Defects in hemostasis arising from genetic mutations or environmental stress can result in bleeding disorders (failure to stop bleeding) or thrombosis (undesirable blood clotting), with symptoms ranging from mild to life threatening[5]. Pathologies of hemostasis affect more than 2% of the US population. Computer simulations of hemostasis have been developed to supplement knowledge gained through experimental and clinical research. For more than a decade, simulation studies have evolved to study platelet aggregation and thrombus formation under increasingly realistic conditions (e.g. complicated vascular geometry, multiple ligand-binding kinetics, and comprehensive coagulation cascade system[6]). Though model simplification, assumption, and approximation remain

unavoidable, researchers are building more accurate models with the aid of enhanced computing power and an improved understanding of the underlying biological processes.

Current multiscale, computational methods applied to study these delicate physiological processes utilize different compositions of several fundamental yet important modules, such as fluid mechanics, coagulation cascade, cell mechanics and receptor-ligand binding. Each of these modules focuses on a specific range of the length/time scales (Figure 1). More detailed description of each module can be seen in Table 1.1. A reasonable platelet aggregation model usually comprises two or more of these inter-correlated modules to achieve the multiscale model structure, and such inter-correlation is usually achieved by variable transmission. For example, Alber and colleagues have established a 2D thrombus development model[7], which considers both the hemodynamics and coagulation cascade reactions, but is not involved in cell mechanics and receptor-ligand binding. Pivkin et al. have developed a 3D model that incorporates fluid mechanics and physical cell particle modules where a platelet-rich thrombus is growing inside a cylindrical vessel[8], but the adhesion model is based on threshold assumptions that have not been experimentally supported. Fogelson et al. developed a continuum platelet aggregation model by considering only the fluid phase[9,10], where the effect of platelet adhesion was simulated by a force distribution generated from elastic linkage between cells onto the fluid (plasma). The model was later modified to incorporate the platelet-wall interaction[11] and a partial coagulation cascade[12]. Our group has constructed a 3D platelet aggregation model (Platelet Adhesive Dynamics, or PAD) with ellipsoid platelet particle aggregates via receptor-ligand binding under simple shear flow[13,14].

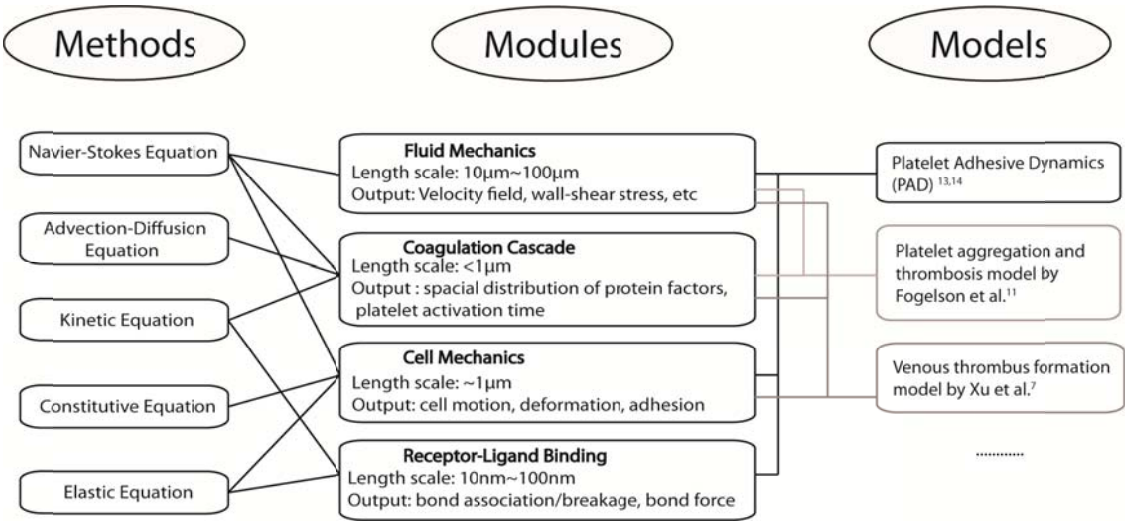

Figure 1.1 The summary of the systematic structure of different methods, modules and models in current studies of multiscale modeling of platelet aggregation and thrombus development. Here, each module utilizes a group of selected methods (usually representative governing equations), and one computational model usually contains several organized modules.

Validation of these mathematical models is often done by comparing simulation results with in-vivo/in-vitro experimental data. The experimental observations can cover a wide range of types, including cellular response to signal molecules, visualization of cell motion in microfluidic devices and confocal microscopy of in-vivo thrombus development.

1.1 Hydrodynamics

Hydrodynamics and blood rheology are critical for maintaining normal hemostatic function. The margination of platelets, dependent on factors such as finite platelet size[15], large volume fraction of red blood cells (RBCs), the relatively high stiffness of platelets (compare to highly deformable RBCs)[16] and physiological shear stress in the blood flow[17], tends to cause platelets to be concentrated in the peripheral region near the vessel wall. This enables efficient attachment of platelets onto the injured vessel wall which results in reduced bleeding time. The non-Newtonian nature of blood, primarily resulting from fibrinogen in the plasma[18] and deformable RBCs[19], may also entrap activated platelets in vortices and recirculation regions to form clots[20]. These effects are all consequences of hydrodynamics.

Hydrodynamics modules directly determine the level of realism of the physical model. Though most existing methods utilize the Navier-Stokes Equation as the governing equation, different model settings greatly affect the simulation power to recreate the realistic physiological environment. Commercially available software packages are usually designed based on computational fluid dynamics (CFD) methods, which were

Table 1.1 Example applications with their length scales for each module.

Simulation Modules	Applications	Example References	Scale
Fluid Mechanics	CFD	21~23	Tissue/vessel/cell
	SDM	24~26	Tissue/vessel/cell
	DPD	30~32	Tissue/vessel/cell
	CDL-BIEM	13, 14	Tissue/vessel/cell
Coagulation Cascade	ODEs/PDEs sets describing space-time concentration fields of chemicals	12, 46	Vessel/Cell
Cell Mechanics	Membrane mechanics combined with elastic and viscous fluid	75~77	Cell
Platelet Activation	ODEs/PDEs sets describing space-time concentration fields of different type of cells	67~69	Vessel/Cell
Receptor-ligand Binding	Voigt's model for cell-cell interaction	25	Cell
	Monte Carlo method used to determine the bonding profile	14	Protein/Molecule

introduced in the 1990s[21] and are potentially powerful tools to elucidate some of the hemodynamic challenges. Nowadays, CFD has evolved to be combined with image-based[22], personalized[23] techniques to study individual symptoms. However, when studying flow-induced blood clotting, an approach based on a single-phase continuum assumption such as that employed by many commercial CFD packages may inaccurately represent the nature of blood flow during hemostasis. It may also fail to model the multiscale nature when characterizing blood constituents (soluble proteins and cells), which change their properties in response to biochemical/mechanical signals. Recent progress on advanced computational methods as well as high-performance computing has aided researchers in developing more versatile approaches such as Stokesian Dynamics Methods (SDM), Dissipative particle dynamics (DPD) and Complete Double Layer Boundary Integral Equation Method (CDL-BIEM).

SDM was developed by Brady and coworkers[24] and is capable of simulating the motion of a group of highly concentrated, finely-shaped (mostly spheres) solid particles in a low Reynolds number suspension fluid while accurately accounting for the hydrodynamic interaction between them. Yamaguchi's group developed a thrombus development model based on SDM and successfully confirmed that development of thrombus formation in height requires not only von Willebrand factor, but also fibrinogen[25]. Later, they incorporated the presence of RBC's and argued that the RBCs play a role in hemostasis by promoting horizontal spreading of the growing thrombus[26]. Another method that is also capable of dealing with a large number of suspension particles, but not limited to the Stokes flow condition, is the Lattice Boltzmann Method

(LBM). LBM relates to the Molecular Dynamics (MD) method and has successfully simulated multiphase blood flow with a hematocrit value of 40% and platelets[27-29], though no effort has been devoted to thrombus formation yet.

The DPD method, on the other hand, simulates both plasma and platelets as virtual discretized particles that move according to Newton's Law, thus sharing similarities with MD as well. Though discretization of the continuum Navier-Stokes equation is used, the DPD method has been shown to compare well with Navier-Stokes solutions[30]. Tsuda and colleagues applied the DPD method to construct the thrombosis development process through platelet accumulation onto the vessel wall[31]. Pivkin et al. also utilized DPD to study the enhanced diffusivity of platelets caused by RBCs on platelet aggregation[32].

CDL-BIEM is a boundary integral method that is used to solve the integral form of Stokes equation under low Renolds number flow. Kim and Karilla discuss the theory detailing the development of this technique in their text[33] and the derivation of this solution method as applied to particulate flow in a half space is fully described by Phan-Thien et al. As a boundary integral method, CDL-BIEM is specialized to solve the mobility problem for arbitrarily-shaped solid particles represented by mesh-grid structures, for instance, when an ellipsoid platelet is flowing close to the vessel wall. As a result, CDL-BIEM is able to explore the shape factor of a platelet during thrombosis[34]. Further, Mody et al. conclude that the platelet-platelet hydrodynamic collision patterns are significantly different when implementing platelets in their natural ellipsoid shape rather than a spherical shape[14].

1.2 Coagulation Cascade

The blood coagulation cascade is an essential component of hemostasis reactions. It has two initially independent pathways, namely the contact activation pathway (intrinsic pathway) and the tissue factor pathway (extrinsic pathway) [35-37]. These two pathways merge at the point of activating procoagulant protein factor X into factor Xa, which forms the tenase complex and mediates thrombin generation. Thrombin in turn acts as a serine protease that converts soluble fibrinogen into insoluble strands of fibrin leading to formation of fibrin network. Fibrin, together with platelets, support the mechanical structure of a thrombus[38].

Over the past two decades, the systems biology approach has thrived and become a common tool in studying blood coagulation and thrombosis. Ataullakhanov classified coagulation models into two sub-categories: 1) the reaction sub-model and 2) the physical sub-model[39]. The reaction sub-model is composed of independent reactions (represented by a list of ODEs and PDEs) that when combined, encompass the entire coagulation cascade, while the physical sub-model contains the spatial properties that take the mass transport under flow dynamic into consideration. The reaction sub-model has been widely studied by computational biologists[40]. For example, tissue factor initiated blood coagulation was explored[41], and the kinetics of thrombin generation was revealed and compared with high throughput experimental results[42]. The systems biology approach is also capable of identifying potential “fragile points” inside the cascade which serve as good targets for therapeutic strategies[43] despite the remaining

parametric and structural uncertainty of the model[43,44]. In order to study thrombus development, both sub-models should be incorporated into the coagulation module. Though most researchers using the systems biology approach to study the coagulation cascade don't consider the physical existence of the developing thrombus, and most researchers studying platelet aggregation/thrombus formation do not take into detailed consideration either thrombin-mediated platelet activation or the fibrin network, there are some groups that attempt to couple those two complex systems together.

One of the first models that incorporated the coagulation cascade (especially the extrinsic pathway in the following cases) and platelet deposition was introduced by Kuharsky et al.[12] in 2001. The model contains both plasma-phase and membrane-phase reactions, and accounts for chemical and cellular transport by flow and diffusion[12]. It predicts the threshold manner of change of thrombin production due to the increasing number of tissue factor binding sites. It also argues that the inhibition of the activity of TF;VIIa enzyme complex is dominant by physical blockage of platelets onto the subendothelium, rather than chemical inhibitors[12]. By using a similar approach, Fogelson et al. studied the influence of flow-mediated transport on the initiation and inhibition of coagulation[45]. Later, Leiderman and Fogelson established a spatial-temporal model to study platelet activation and blood coagulation under flow[46] and they discovered the dependence of FXI dependent thrombin generation on platelet count[47]. The above models treat different status of platelets (activated, non-activated, subendothelium bound, etc) as "chemical-like", which describes the physical existence of platelets by their spatial concentration profile.

On the other hand, Xu et al. implemented the tissue factor pathway described in Jones & Mann[48] for the generation of thrombin involving the activation of factors IX, X, V, VIII, VIIIa–IXa, and factors Va–Xa (prothrombinase) into their thrombosis model[49]. In 2010, Xu et al. extended their coagulation model into both solution-phase and membrane-phase reactions[7], the total number of factors being considered in the model also increased by several-fold. Their model considers the coagulation process as a source of cell status change[49] but no detailed mechanical properties of the fibrin network were considered.

Though all the existing coagulation modules remain within 2D space, they are to be extended into 3D. Further, they will be more commonly applied to future simulation studies of thrombosis, as the importance of the mechanical structure of fibrin network to the mature thrombus function is being revealed and receiving more attention[50,51].

1.3 Receptor-Ligand Binding

The initiation of thrombus development starts with tethering of circulating platelets onto the exposed subendothelial layer at the site of a blood vessel injury via bonding between the α subunit of GPIb receptors on the platelet surface and the A1 domain of subendothelial collagen-bound multimeric plasma glycoprotein von Willebrand Factor (vWF)[3,52]. Such GPIbα-vWF-A1 tethering leads to platelet translocation on the subendothelial surface, which prolongs the duration of the platelet-vessel contact; helping platelets gain a sufficient number of biological/ biochemical signals to trigger platelet activation[1,2]. This leads to the formation of other receptor-ligand bonds such as

integrin $\alpha_2\beta_1$ with subendothelial collagen to support firm adhesion of the platelet[53] or $\alpha_{IIb}\beta_3$ to another $\alpha_{IIb}\beta_3$ molecule on the surface of other platelets via fibrinogen or vWF to promote platelet aggregation[54].

Most existing thrombus development models have oversimplified this critical module either using "guessed" values for non-experimentally measured quantitative parameters, or defining threshold judgments for qualitative status changes (e.g. platelet activation, etc). For example, Pivkin et al. treated platelets as having three possible biological states: passive and non-adhesive, triggered, and activated and adhesive[8]. However, as mentioned above, non-activated platelets also interact with injured vessel walls and translocation cannot be recovered in this model.

Mori et al. applied Voigt's model to calculate the binding force between platelets, where the aggregation of platelets is mediated by both vWF and fibrinogen[25]. In their model, the association of GPIIb/IIIa-fibrinogen-GPIIb/IIIa and GPIbα-vWF-GPIbα between two platelets is determined by judging the difference in the platelets' velocities. The binding force is unbiased for the possible receptor configurations on the cell membrane between two platelets.

On the other hand, Monte Carlo simulation of receptor-ligand binding between surfaces (known as adhesive dynamics, or AD)[55] treats individual receptors on the cell membrane as separate units and the rate of formation/breakage of each receptor-ligand bond is determined by the Bell Model[56]. The Bell Model calculates the probability of

the association/dissociation event occurring over a specific timespan based on the stretched distance between the roots of the target receptor and the ligand, which is deviated from the relaxed form. As a result, AD can recover complex cell-cell interaction behavior, including translocation, temporary tethering and adhesion. In 1992, AD succeeded in simulating the rolling and adhesion of neutrophils mediated by CD62/ LECAM-1[55]. AD was later applied to reveal the hydrodynamic interaction between stably rolling cells, and between rolling and flowing cells as well[57,58]. AD was first applied to platelets in 2007, where Mody et al. assessed the influence of Brownian motion on platelet transport and single-bond adhesion behavior near wall[59]. AD also successfully recovered the shear-induced platelet aggregation mediated by GPIbα-vWF bridging[13].

It is interesting to note that, though computational models are constantly being improved, experimental results that assign measured values to model parameters are sometimes prone to revision as well. For instance, the dissociation kinetics of the platelet GPIbα-vWF bond was first determined to rely on the Bell Model, which posits a “slip-bond” [60]. The unstressed dissociation constant was also determined by a cell-tethering assay[60]. Later, optical tweezer techniques were applied to single-molecule experiments to obtain a more precise measurement of the dissociation constant[61]. In 2008, researchers discovered that the dissociation of GPIbα-vWF demonstrates a “catch-bond” regime, similar to that of selectins[62,63]. To reflect the “catch-bond” properties, the governing kinetic equations were modified from the original Bell Model[64]. In 2010, a novel experimental technique called ReaLiSM was described, which allows repeated

measurements of the binding and unbinding of a receptor and ligand in a single molecule. ReaLiSM revealed that, instead of "slip-bond" and "catch-bond" transition, GPIbα-vWF has two "slip-bond" regimes, termed a "flex-bond"[65]. Though it is still a controversial topic, it is important to be aware of possible changes in the currently accepted experimental data, which serves as the most convincing method of validation for simulation studies.

1.4 Platelet Activation

Platelet activation is also an essential process during hemostasis. Numerous studies have demonstrated that when a resting platelet encounters agonists such as collagen, thrombin, thromboxane, or ADP, it undergoes a change in shape (from ellipsoid to spheroid), degranulation and becomes fully adherent[66]. Munnix et al. summarized current evidence of the heterogeneity of platelet response to various environmental factors and intrinsic differences (e.g. protein expression level, platelet aging) during thrombus formation[67]. They classified deposited platelets inside a thrombus into three subpopulations, namely "aggregating platelets with reversible integrin activation", "procoagulant (coated) platelets exposing phosphatidylserine and binding coagulation factors", and "contracting platelets with cell-cell contacts", with each subpopulation possessing unique morphology, surface characteristics and functionality[67]. Heterogeneity is also exhibited by suspended platelets in the plasma as well[67]. Purvis et al. developed a molecularly detailed, bottom-up ordinary differential equation (ODE) model that simulates ADP-mediated activation[68,69]. Sorensen et al. utilized a coupled set of convection-diffusion-reaction equations to describe thrombin-induced platelet

activation and deposition[70,71]. These platelet activation models have not yet been combined with the real physical models, but there is growing expectation that they should be included in thrombus growth simulations because of the significant behavioral differences between non-activated and activated platelets.

1.5 Cell Mechanics

In different computational models, the mechanical properties of platelets are usually approximated in one way or another: platelets are treated either as possessing a spherical shape, solid texture, uniform size distribution, or any combination of these. The size of a platelet, commonly represented by the variable mean platelet volume, was found to be associated with a higher risk of thrombosis, stenosis, and cardiovascular disease[72]. The shape factor of platelets has also been shown to be associated with normal platelet function, and the resulting transient tethering due to simple-shear flow has been explored[14,73]. While it is relatively easy to adjust the size and shape of a platelet in simulations, it is somewhat more challenging to incorporate realistic deformability of these cells into the model. Since the stiffness of blood cells greatly influences a cell's ability to marginate[74] and the mechanical properties of the encompassing thrombus, it is important to not only consider the other blood constituents with relatively large volume fractions (e.g. RBCs), but also to treat them as deformable particles. Pozrikidis developed the membrane constitutive equations for deformable RBCs[75]. Membrane in-plane tension, transverse shear tension, and membrane bending moments are added to the cell membrane force and torque balance to conserve the deformable biconcave shape of RBCs[76] and the cell volume. Based on Pozrikidis's membrane mechanics, Zhao et al.

established a spectral boundary integral method that is able to simulate deformable RBCs flowing inside vessels[77]. An similar approach can also be applied to simulate a deformable thrombus or individual platelet.

The structural properties and contractile force of a clot have been known for decades[78]. Recently, single platelet mechanics and contraction dynamics were experimentally determined by atomic force microscopy, which can provide insights into the clot stiffening process[79]. Experimentally determined mechanical parameters of platelets and thrombus provide solid background for simulation studies.

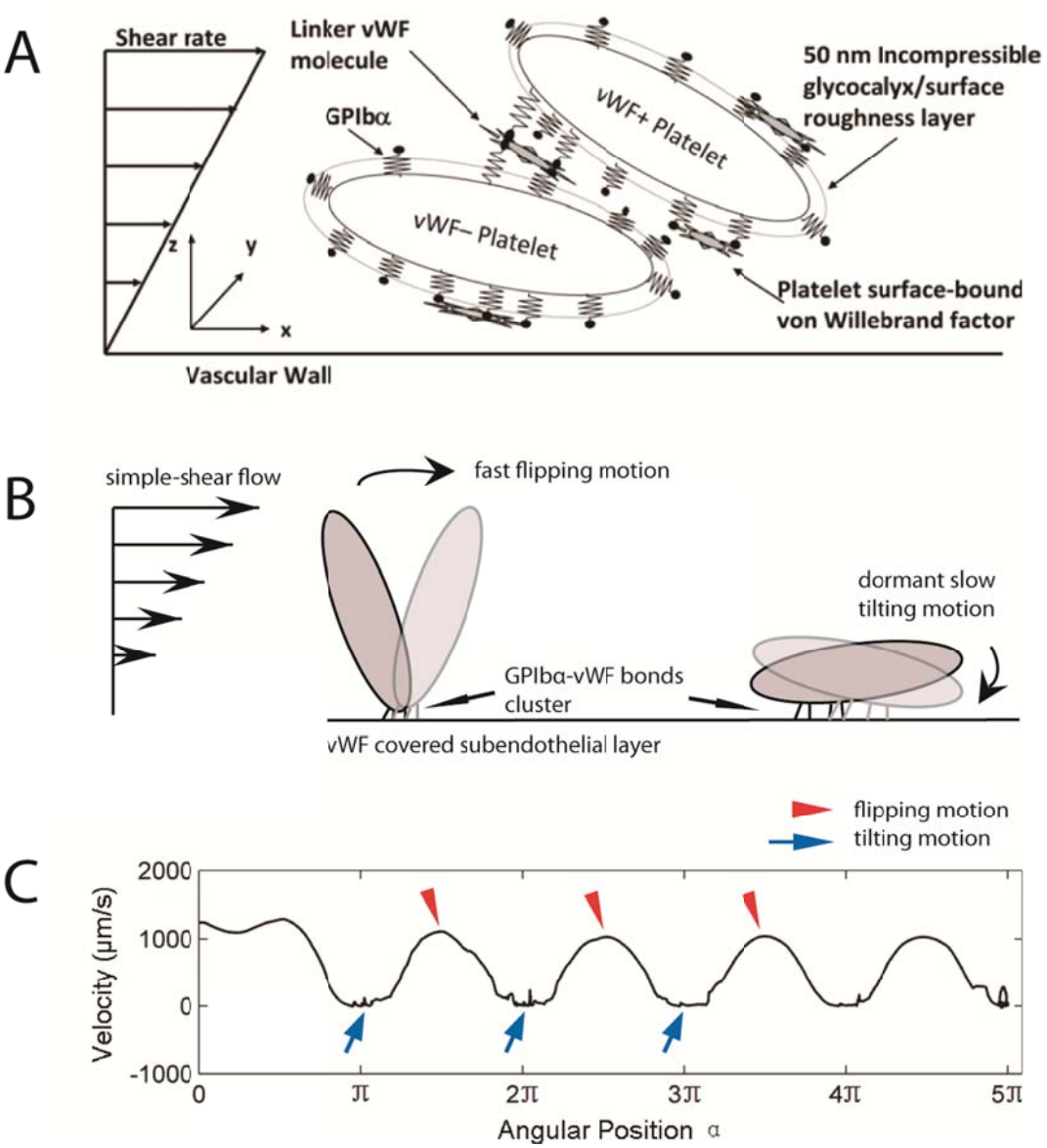

Figure 1.2 A: Schematic diagram of the platelet-platelet bridging that depicts two platelets transiently aggregating in linear shear flow via GPIbα-vWF-GPIbα bonds. B: Diagram showing translocation of a platelet under linear shear flow via repeated bond dissociation from the upstream side and bond formation at the downstream side. C: The linear velocity of the center of the platelet at a shear rate of $1250s^{-1}$. The components of the depicted diagram are not drawn to scale.

1.6 Platelet Adhesive Dynamics (PAD)

PAD, defined by Mody and King[13,14], combines a Monte Carlo simulation of receptor-ligand binding (i.e., called Adhesive Dynamics, or AD) and hydrodynamic calculations with CDL-BIEM. This model has been applied to the scenario where ellipsoid platelets are flowing/tethering close to the vessel wall. The study of platelet aggregation under high shear via GPIbα-vWF-GPIbα bridging contained details such as the physical structure of large multimer protein vWF (Figure 2A). The PAD model successfully explained the mechanisms of Type 2 von Willibrand Disease (vWD), where the subgroups of either large or small vWF multimers are absent. Mody and King discussed that an increase in vWF ligand size in plasma strongly influences the equilibrium binding kinetics and correspondingly increases platelet-platelet binding efficiency. PAD was also able to explore the complex and nonlinear, force loading curve for each individual GPIbα-vWF-GPIbα bond during two-platelet aggregation. Recently, PAD demonstrated the periodic translocating motion of a platelet on an injured vessel surface, where a fast flipping period and a slow tilting period were shown for the ellipsoid-shaped platelet (Figure 2B, 2C). By combining with other type of receptor-ligand binding pairs such as integrin $\alpha_2\beta_1$-collagen, and $\alpha_{IIb}\beta_3$-fibrinogen, PAD will be able to recover the transition from translocation on the sub-endothelial surface to firm adhesion, as well as platelet aggregation after activation. Thus, PAD has the potential to reveal the complete biophysical role of platelets during hemostasis/thrombosis.

1.7 Future Directions

While increasing knowledge of biochemical/biophysical mechanisms of hemostasis and thrombosis has been revealed, computational models are being built towards more comprehensive settings to simulate more realistic physiological processes. However, such model improvement often prohibitively increases the consumption of computer processing power. For instance, the simulation of two platelets aggregating in 3D, which is provided by PAD, usually runs for days or even up to weeks in order to obtain a few seconds of real-time behavior. Even with the rapid evolution of new generations of CPUs, as well as the development of parallel computing algorithms applied on computer arrays, simulations are usually time consuming and computationally expensive. The coarse-grained approach simplifies the computing methods while preserving the fidelity of the model. Coarse-grained methods are also very understandable and easily transferrable, and thus enable more broad collaboration. Though they may be subject to accuracy concerns, it is expected that they will be an important approach and will be incorporated into a variety of models.

While most multiscale simulation models are still prone to verify an identified physiological mechanism (by which they validate themselves at the same time), researchers' original motivation for developing simulations is their potential predictive power. Mody et al. applied simulations and predicted that the 2-D cross-linking rate of GPIbα-vWF bond appears to be consistent with a piecewise linear model dependent on the imposed fluid shear rate, with a weak dependence on shear rate followed by a stronger dependence on shear rate[13]. Later, Singh et al. experimentally presented a similar piecewise kinetics dependence for vWF-bisANS binding, proposing the unfolding

mechanism of vWF under shear flow[80]. Another example of model prediction is the systems biology approach of S. Diamond and colleagues comprised of a complete bottom-up simulation of platelet metabolism based on a Monte Carlo algorithm which is reaching a point where patient-specific prediction of coagulation kinetics may be possible[40].

Multiscale simulations reinforce the significance of in-vitro studies by filling the gaps between in-vitro experiments to in-vivo human thrombus formation. While it is difficult to recover the full spectrum of in-vivo conditions in-vitro, ideally conditioned in-vitro experiments provide accurate measurement of chemical/physical parameters. Those parameters can be incorporated into models to better recreate realistic and complex in-vivo conditions. On the other hand, the quality of simulations is heavily dependent on the quality of in-vitro data, as the accuracy of the model parameter measurements is critical to support the fidelity of simulation models.

It is hoped that the employment of multiscale simulations of hemostasis and thrombosis will be focused towards clinical predictions, such as diagnosis of a stenosis configuration, estimation of its progression rate and prognosis after surgery. Simulations may also facilitate personalized medicine. An example of this might be a patient with a femoral artery stenosis being implanted with a stent whose geometry is specifically designed to reduce the possibility of turbulent and high-shear flow, which will help prevent further thrombosis in the narrowing vessel region. Such stent design can be supported by recovery of the 3D structure of the patient's femoral artery through non-invasive imaging,

followed by CFD calculation of the associated fluid mechanics. Another example which focuses on microscopic level is specifically designed small soluble protein molecules introduced into the blood circulation system, where the small molecule is capable of restoring normal vWF function in type 1 von Willebrand Disease patients. Such protein design may be based on patient-specific genome sequencing, vWF structure recovery and MD simulation with thousands of small molecule candidate compounds. Simulation might also predict the physiological effects where the pharmacodynamics of a drug can be individually determined for each patient beforehand.

Future simulations of hemostasis process may also involve other physiological processes. Platelets, for example, were long thought to associate with cancer metastasis since the early 1990's[81]. More recently, it has been well studied that platelet activation and blood coagulation have a crucial role in the progression of cancer[82]. Platelets also physically promote tumor metastasis by protecting tumor cells from immune elimination and enhancing their arrest on the endothelium[82]. By introducing cancer cells into hemostasis models, researchers will be able to simulate platelet-mediated tumor metastasis. Platelets also play other pathological roles in inflammation and atherogenesis[83]. In summary, multiscale simulations of hemostasis will be more versatile in the future, being applied in different biological fields.

1.8 Code Sharing

Computer simulation of biological processes has expanded tremendously over the past two decades. Storage databases, such as those used for genomic data in computational

genetics, have been widely shared. However, databases of methods (i.e. algorithms or modules) have not seen the same pooling of resources. While commercially available packages are costly and inflexible toward adjustment, highly compatible platforms have been established for better communication, wider application and more powerful combined modules. Those platforms have a list of compatible components from markup languages and simulation tools to model databases and discussion forums. System Biology Markup Language (SBML) and one of its derivatives, CellML, are examples of common tools for multiple-scale analysis and simulation of biological systems, with the latter placing a special emphasis on cellular phenomena. SBML and CellML are powerful for simulating the coagulation cascade and platelet activation, but are not optimal for physical models, such as cell motion or deformation under flow. Closer collaboration will be required in order to develop comprehensive and more realistic models. Working groups have been formed in order to better serve the networking purposes of computational biologists; these also facilitate the sharing of codes that are not readily transferrable to common platforms. The Multiscale System Biology Working Group is such an example[84]. The group establishes a website platform with up-to-date information on available tools, novel concepts, and major, relevant review papers in the field. The goal is to identify and articulate current challenges and opportunities in the field, as well as to foster scientific collaboration.

CHAPTER 2: MULTISCALE MODEL OF PLATELET TRANSLOCATION AND COLLISION

The tethering of platelets on the injured vessel surface mediated by glycoprotein Ibα (GPIbα) - Von Willebrand factor (vWF) bonds, as well as the interaction between flowing platelets and adherent platelets, are two key events that take place immediately following blood vessel injury. This early-stage platelet deposition and accumulation triggers the initiation of hemostasis, a self-defensive mechanism to prevent the body from excessive blood loss. To understand and predict this complex process, one must integrate experimentally determined information on the mechanics and biochemical kinetics of participating receptors over very small time frames (1-1000 s) and length scales (10-100 nm), to collective phenomena occurring over seconds and tens of microns. In the present study, a unique three dimensional multiscale computational model, platelet adhesive dynamics (PAD), was applied to elucidate the unique physics of (i) a non-spherical, disk-shaped platelet interacting and tethering onto the damaged vessel wall followed by (ii) collisional interactions between a flowing platelet with a downstream adherent platelet. By analyzing numerous simulations under different physiological conditions, we conclude that the platelet's unique spheroid-shape provides heterogeneous, orientation-dependent translocation (rolling) behavior which enhances cell-wall interactions. We also conclude that platelet-platelet near field interactions are critical for cell-cell communication during the initiation of microthrombi. The PAD model described here

helps to identify the physical factors that control the initial stages of platelet capture during this process.

2.1 Introduction

One of the key events in early stage hemostasis – a self-defensive mechanism to prevent excess blood loss by forming a clot to cover the disturbed vessel surface – is the initial tethering of circulating platelets onto the exposed subendothelial surface at the site of blood vessel injury. Followed by translocation of platelets under linear wall-shear driven by blood flow, such platelet-vessel interactions under moderate to high shear rate (>500 s^{-1}) are mediated through bonding between the α subunit of GPIb receptors on the platelet surface and the A1 domain of subendothelial collagen-bound multimeric plasma glycoprotein Von Willebrand factor (vWF). [3,52] The translocation of a platelet on a subendothelial surface through the GPIbα-vWF-A1 bond prolongs the duration of platelet-vessel contact to gain enough signals from receptor-ligand bonding as well as surrounding soluble platelet activation factors to trigger platelet activation [1,2]. This leads to the formation of other receptor-ligand bonds such as integrin $\alpha_2\beta_1$ with subendothelial collagen to support platelet firm adhesion [53] and $\alpha_{IIb}\beta_3$ with its same kind on the surface of other platelets through fibrinogen (also other molecules such as vWF) to cause platelet aggregation [54]. GPIbα-vWF-A1 bonds have been demonstrated to exhibit selectin-like, slip-bond kinetics that include fast intrinsic association and dissociation rates, force dependence of dissociation rate, and a requirement of a threshold shear stress for adhesion to occur [60,84,85]. Recently, a catch-bond sub-regime that spans the lower range of bond force has also been revealed and the detailed bond kinetics

for the transition of catch-slip sub-regimes – a modified quasi-first order dissociation reaction – has been established [62,64]. Qualitative defects on GPIbα and vWF, which result in platelet-type Von Willebrand Disease (vWD) and 2B-type vWD respectively [86], alter the kinetics of the GPIbα-vWF-A1 bond and lead to disordered bleeding phenotypes [85,87-89]. Specifically, for platelet-type vWD, the mutant GPIbα receptor stabilizes the interaction with inactive circulating vWF, depleting the vWF pool in plasma, causing insufficient binding of vWF to subendothelial surfaces during injury leading to hemorrhage [90].

Once the translocating platelet becomes activated and fully adherent – mediated by platelet-collagen receptors (e.g. integrin $\alpha_2\beta_1$) – dramatic changes take place including: exocytosis of α-granules and dense granules (leading to the release of ADP, thrombin and other activating factors), change in shape from discoid to spherical, extension of filopodia, formation of thromboxane A2 (TXA2), and activation of other surface receptors (e.g. integrin $\alpha_{IIb}\beta_3$) that mediate platelet aggregation. Recent studies have shown that there are three distinct mechanisms that intitiate platelet aggregation at various shear rates [91]: i) a single-stage aggregation is predominantly mediated by the interaction of fibrinogen with integrin $\alpha_{IIb}\beta_3$ (shear rate < 1000 s^{-1}); ii) a distinct two-stage aggregation process with the initial-stage aggregations dependent on membrane tethering GPIbα, integrin $\alpha_{IIb}\beta_3$, and a later stage associated with soluble agonists such as ADP (1000 s^{-1} < shear rate < 10000 s^{-1}); iii) platelet aggregation begins independently of integrin $\alpha_{IIb}\beta_3$ or platelet activation and is exclusively mediated by the vWF-GPIbα interaction and form a platelet plug (shear rate > 10000 s^{-1}). The third mechanism has been described in further detail as

a shear-gradient dependent aggregation where a platelet plug can form under mechanical shear-gradient caused by sharp changes in local vessel geometry (stenosis, etc) in the absence of vessel injury [92].

Though critical, few attempts were made to elucidate the physics of the platelet aggregation, and the majority of them utilize multiscale simulation methods which contain parameters and assumptions that cannot be easily determined by experiments. This greatly hampers the fidelity of the simulation work. One explanation is the difficulty of constructing a precise platelet aggregation model a priori. Accurate predictions based on the simplifying assumptions during early thrombus formation (coarse-grained methods) must first be made. A free-flowing two-platelet aggregate mediated by GPIbα-vWF-A1 bonding at physiologically high shear rate (>10000 s^{-1}) was studied [13], but a more typical scenario to focus on is that of a flowing platelet interacting with a captured and immobilized platelet on the injured surface. The present article describes a multiscale computational study focusing on specific biophysical details including the transient formation of GPIbα-vWF-A1 bonds, which mediate the translocating motion of ellipsoid-shaped platelets on an injured surface, as well as the hydrodynamic interaction between an upstream flowing platelet and a downstream, adherent platelet. Based on the well-developed Platelet Adhesive Dynamics (PAD) numerical method, we explore these fundamental hemostasis/thrombosis procedures in depth and provide necessary results for future coarse-grained simulation study.

2.2 Platelet Adhesive Dynamics (PAD)

The PAD model is a multiscale three-dimensional (3-D) numerical simulation method that consists of two distinct yet interrelated components: (1) the 3-D hydrodynamic motion of multiple solid-body spheroid-shaped particles (platelets) under simple shear flow near a stationary planar surface (vessel wall), and the (2) adhesive dynamics of receptors on the platelet membrane binding to their ligands. The adhesive dynamics component utilizes the Monte Carlo method to determine each bond formation/breakage event based on specific receptor-ligand binding kinetics. It calculates the bond forces, which yield the net force and torque acting on each platelet particle. These net forces and torques will then be introduced into the hydrodynamic equations to solve the mobility problem. The PAD model has been successfully used to characterize flowing platelet convection and the high shear-induced behavior of aggregates. [13,14]

2.2.1 The hydrodynamic calculation

This problem involves the creeping motion of one/two rigid oblate spheroid particles of 96 or 384 QUAD9 surface elements (96 for all of the translocation simulations, and 384 for all of the collision simulations) with an aspect ratio of 0.25 in a semi-infinite three-dimensional region filled with a fluid of density of 1.0 g/cm^3 bounded by an infinite flat plane at z = 0 [34].

The Reynolds number of this system is calculated as $N_{RE} = \gamma \rho a^2 / \mu < \mathrm{O}(10^{-2}) < 1$, where the wall shear rate, $\gamma < 10,000 s^{-1}$, is within physiological range, the particle radius, a, is 1 μm, the density of blood plasma, ρ, is 1.0239 g/cm^3, and the viscosity of blood plasma, μ, is 1.0 cP. The flow is within the Stokes regime. The Stokes equation for linear shear ambient flow is:

$$\nabla p = \mu \nabla^2 u\,,\ \nabla \cdot u = 0\,,\ u_\infty = \gamma z\,,\ u_{z=0} = 0\,, \tag{1}$$

where **u** is the velocity, **p** is the pressure, **μ** is the viscosity of the fluid, **γ** is the shear rate, and **z** is the horizontal distance from the center of the particle to the flat wall.

The completed double layer-boundary integral equation method (CDL-BIEM) [33], a boundary elements solution technique to solve the integral representation of the Stokes equation, was used to solve Eq. 1. It is based on the integral representation of the Stokes equation:

$$u_j(X) + \int_S n_k(x) \sum_{ijk} (x, X) u_i(x) dS(x) = \int_S G_{ij}(x, X) \sigma_{ki}(x) n_k(x) dS(x)\,, \tag{2}$$

Here, $\mathbf{G_{ij}}$ is the singularity solution due to a point force on the bounding surface **S**, with **x** acting in the **j** direction of the fluid. The factor **n(x)** is the unit normal vector at **x** and points out from the particle surface into the surrounding fluid, and σ is the stress tensor given by:

$$\sigma = -p\mathrm{I} + \mu(\nabla u + (\nabla u)^t)\,, \tag{3}$$

where **I** is the identity matrix and the superscript t denotes the transpose operator. The integrals on the RHS and LHS of Eq. 2 are known as the single-layer and double-layer potentials, respectively. Both of the expressions are carried out over the bounding surfaces, including the surface of all the particles, but not the infinite plane. The singularity solutions in half-space are used to account for the infinite wall effect [43]. Eq. 2 is termed a boundary integral equation (BIE) where the velocity u(X) is evaluated at the particle surface. It has been shown that the BIE containing the single-layer potential is sufficient to represent the Stokes disturbance flow problem for particles undergoing rigid body motion. However, this integral equation takes the form of a Fredholm integral

equation of the first kind, which for a mobility problem is generally ill-posed and becomes numerically unstable for more refined boundary element meshes [33]. An alternative method solely involves the double-layer potential. Because the double-layer potential does not exert any net force or torque, Power and Miranda [93] incorporated an unknown density (corresponding to the velocity $\mathbf{u_i(x)}$) ,which results in a net force and torque that coincides with the behavior at infinity for Stokes flow (i.e. velocity decays as $\mathbf{R}^{-1}$) into the double-layer integrals. The summarized solution method for Eq. 2 was described by Phan-Thien et al. [43], with the final form of the boundary integral equation shown as

$$\phi_j(\zeta) + (\mathrm{K}\phi)_j(\zeta) + \phi_j^{(p,l)}(\zeta)\left\langle \phi^{(p,l)}, \phi \right\rangle - \psi_j^{(p)}(\zeta)\left\langle \psi^p, \phi \right\rangle = b_j(\zeta) - \frac{1}{2}\psi_j^{(p)}\left\langle \psi^{(p)}, b \right\rangle, \zeta \in S$$

(4)

where $\boldsymbol{\varphi_j}$ is the unknown surface density of the double-layer distribution, $\mathbf{K}$ represents the double-layer surface integral operator, $\boldsymbol{\varphi^{(p,l)}}$ are the orthonormalized null solutions corresponding to the translational (l=1,2,3) and rotational (l=4,5,6) motions of particles p, and the angled brackets represent the inner product $\langle p, q \rangle = \int_S p(x) \cdot q(x) dS(x)$. P takes on values from 1 to N (total particles in the system), $\psi^{(p)}(\zeta)$ are the orthonormalized eigenvectors of the operator K with the value $n/\sqrt{S^{(p)}}$ for $\zeta \in S^{(p)}$, but 0 for $\zeta \notin S^{(p)}$. On the RHS of Eq. 4, $b_j(\zeta)$ is calculated as

$$b_j(\zeta) = -u_j^{\infty} + \sum_{\alpha=1}^{N}(F_i^{(\alpha)} - \frac{1}{2}(T^{(\alpha)} \times \nabla)_i) G_{ji}(\zeta, x_c^{(\alpha)}), \zeta \in S \qquad (5)$$

where $\mathbf{F^{(\alpha)}}$ and $\mathbf{T^{(\alpha)}}$ are the force and torque acting on cell α at the center of mass $\mathbf{x_c^{(\alpha)}}$ of the particle, and $\mathbf{u_j^{\infty}}$ is any ambient fluid velocity that is a valid solution of the Stokes equation.

These equations are solved by Newton iteration for **φ**. Once the double-layer density, **φ**, is determined, the surface velocity field can be obtained as follows:

$$u_j(\zeta) = -\phi_j^{(p,l)}(\zeta)\left\langle \phi^{(p,l)}, \phi \right\rangle \tag{6}$$

By taking the inner product of Eq. 6 and $\boldsymbol{\varphi^{(n,m)}}$ (n = 1,…,N; m = 1~6), the rigid body motion of a particle **n** can be extracted.

2.2.2 Bond kinetics and bond force

The GPIbα receptor density on the platelet surface is about 1500 molec/μm^2 [94]. When the circulating platelet approaches the site of vessel injury, GPIbα-vWF-A1 bonds can be formed between the platelet surface receptor GPIbα and the subendothelial-bound vWF at the injury site and are treated as linear springs throughout the simulation model. The Monte Carlo method is used to determine each individual GPIbα-vWF-A1 bond formation/dissociation event using the probability formulations $\mathbf{P_f}$ (probability of bond formation) and $\mathbf{P_r}$ (probability of bond breakage) described by Hammer and Apte [55]:

$$P_f = 1 - \exp(-k_f \Delta t)\,,\; P_r = 1 - \exp(-k_r \Delta t)\,, \tag{7}$$

where $\mathbf{k_f}$ and $\mathbf{k_r}$ are given in s^{-1} units and **Δt** is the simulation time step 10^{-7} s.

The mathematical expression for the rate of bond formation was derived from Bell's expression [95] of the equilibrium constant for cell-cell bond bridging. The dependence of bond formation rate $\mathbf{k_f}$ on the deviation bond length $|\mathbf{x_b}\text{-}\mathbf{l_b}|$ and slip velocity between

two bonding molecules takes the similar form described by Mody et al. [13] and is shown in Eq. 8,

$$k_f = k^0_{f,2-D} v_s \exp(\sigma \mid x_b - l_b \mid \frac{\gamma - 0.5 \mid x_b - l_b \mid}{k_B T}) \quad , \tag{8}$$

where $\mathbf{v_s}$ is the slip velocity determined by the rotational and translational velocities as well as the location of the GPIbα receptor on the platelet surface, $\mathbf{x_b}$ is the distance spanning the endpoint of the GPIbα receptor on the platelet surface and the vWF-A1 binding site on the vessel wall, $\mathbf{k_BT}$ is the product of Boltzmann's constant and temperature. In our translocation assay, we assume abundant vWF ligand on the injured vessel wall surface, thus $\mathbf{x_b}$ here is simply the z-coordinates minus the surface roughness. The physical meaning and value of the other parameters in Eq. 8 can be found in Table 2.1.

The reverse rate $\mathbf{k_r}$ was evaluated using the Bell model [56] for the force-dependent dissociation rate of weak non-covalent bonds in previous studies [13], because the GPIbα-vWF-A1 bond demonstrates selectin-like binding kinetics: (1) short-lived tethering events and (2) a fast intrinsic dissociation rate constant [60]. This model involves pure slip-bond kinetics stated as following:

$$k_r = k_r^0 \exp(\frac{\gamma \cdot \sigma \mid x_b - l_b \mid}{k_B T}) \tag{9}$$

The value for the intrinsic dissociation rate $\mathbf{k^0_r}$ and the reactive compliance γ were determined from optical tweezer studies [61] with $\mathbf{k^0_r}$ = 5.47 s^{-1}, $\boldsymbol{\gamma}$ = 0.71 nm.

The GPIbα-vWF-A1 bond dissociation based on the Bell model is widely accepted and applied. However, recent in-vitro experiments suggest a new catch-bond/slip-bond force-

Table 2.1 Values of bond formation kinetic parameters

Parameter (unit)	Definition	Value	Reference
l_b (nm)	Equilibrium GPIbα-vWF-A1 bond length	128	[96,97]
γ (nm)	Reactive compliance	0.71	[61]
$k^0_{f,2-D}$ (s^{-2}/μm)	Intrinsic cross-linking formation rate constant	0.05	Determined from simulations
σ (pN/nm)	Spring constant of bond	10	[98]

dependent interchanging mechanism for the GPIα-vWF-A1 bond [64]. This explains the results from studies demonstrating the unusual platelet translocation pattern that an increase in shear stress lowers the average translocation velocity of platelets in a flowing chamber assay below 20 dyn/cm^2 of shear stress [62,63]. These results suggest that two GPIbα-vWF-A1 states exist in the system during platelet rolling. More specifically, two structural arrangements of the vWF A1 domain have been revealed, with one in a native, folded state (NG) which exhibits catch-bond kinetics while another more stretched conformation of an intermediate, open state (IG) that exhibits slip-bond kinetics [64]. The resulting reverse rate, k_r, is a quasi-first-order dissociation rate, which consists of a slip-bond dissociation component and a catch-bond dissociation component, shown as:

$$k_r = \frac{1}{1+\Phi} k_N(f) + \frac{\Phi}{1+\Phi} k_I(f), \quad \Phi = IG/NG, \tag{10}$$

where Φ represents the population ratio of binding vWF molecules between the IG state and NG state and is dependent on the bond force f as follows:

$$\Phi(f) = k^0_{NG\to IG} / k^0_{IG\to NG} * \exp(\frac{\gamma' f}{k_B T}). \tag{11}$$

This two-state, quasi-first-order dissociation model was first applied to the P-selectin: PSGL-1 interaction [99] and simulations of quasi-first-order dissociation have successfully predicted the nano-to-micro scale dynamics of P-selectin detachment from leukocyte interfaces [100]. Each IG/NG state has its own force-dependent dissociation rate based on the classic Bell Model:

Dissociation from the NG state: $k_N(f) = k^0_{N,off} \exp(\frac{y_N f}{k_B T})$, (12)

Dissociation from the IG state: $k_1(f) = k_{1,off}^0 \exp(\frac{y_1 f}{k_B T})$. (13)

The physical significance and values for all of the parameters in Eq. 10~12 can be found in Table 2.2.

The bond force f in Eq. 9-12 is expressed as $\boldsymbol{\sigma(x_b - l_b)}$.

2.3 Platelet translocation (rolling)

The translocating motion of a platelet at the site of injury is mediated by the frequent formation and dissociation of GPIbα-vWF-A1 bonds at the interface of damaged endothelium and the platelet surface under simple shear flow (Figure 2.1). This interaction reduces the platelet translational velocity by orders of magnitude, providing an adequate time window for the platelet to become activated and fully adherent to the exposed subendothelial matrix before extravastion at the injury site.

In-vitro platelet translocation experiments provide a useful technique to study the GPIbα-vWF-A1 bond kinetics and have been successfully applied to explain mechanisms of bleeding disorders resulting from various vWF pathologies [62,89]. Our simulation model utilizes recovers the platelet translocation behavior and serves as a potentially powerful predictive tool that elucidates mechanisms of disease through altered bond kinetics, platelet shape or surface receptor count.

The translocation of an ellipsoid-shaped platelet (Figure 2.2) was demonstrated using traditional slip-bond dissociation kinetics (Bell Model). The intrinsic cross-linking

Table 2.2 Values of bond dissociation kinetic parameters

Parameter (unit)	Definition	Value	Reference
$k^0_{NG\to IG} / k^0_{IG\to NG}$	Unstressed equilibrium constant for NG – IG states	0.4	[64]
γ' (nm)	Force compliance for two states ratio	0.45	[64]
$k^0_{N,off}$ (s^{-1})	Intrinsic dissociation constant for NG state	4.9	[64]
$k^0_{I,off}$ (s^{-1})	Intrinsic dissociation constant for IG state	1.84	[64]
y_N (nm)	Force compliance of dissociation for NG state	-0.23	[64]
y_I (nm)	Force compliance of dissociation for IG state	0.039	[64]

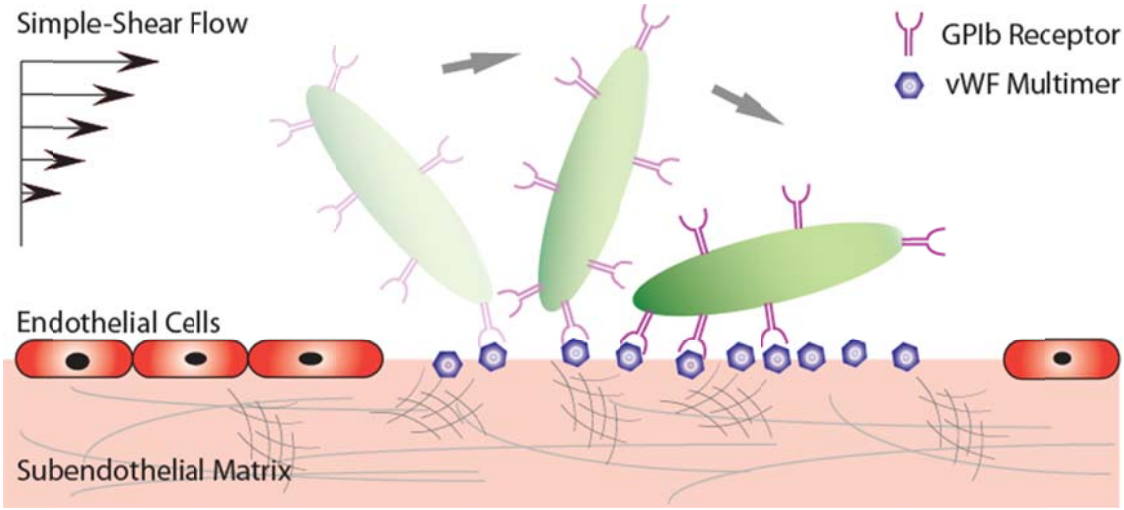

Figure 2.1 Schematic depicting the translocational motion of a platelet at a site of injury (removed endothelial layer) via GPIbα-vWF-A1 bonds under simple-shear near-wall blood flow.

formation rate constant, $k^0_{f,2\text{-}D}$, was tested over a range of values (from 0.001 to 10 $s^{-2}/\mu m$) under varying physiological shear rates (100~ 2000s^{-1}) and then determined by its translocation (larger $k^0_{f,2\text{-}D}$ resulted in fully adherent status and flipping motion was never observed in the simulation time range of 1 s, while smaller $k^0_{f,2\text{-}D}$ resulted in undetectable tethering events, data not shown). The determined $k^0_{f,2\text{-}D}$ was 0.1 $s^{-2}/\mu m$. The rolling motion was composed of a fast flipping period (sharp peaks in Figure 2.2B) where the velocity of the platelet's center of mass reached the flow velocity, followed by a long residence period where the lever arm of the hydrodynamic force acting on the platelet was small, thus increasing the difficulty of breaking existing GPIbα-vWF-A1 bonds. The duration of residence time for each flipping cycle may be different, and depends on the number of existing bonds in the system as well as the uncertainty of a specific bond lifespan due to the dissociation probability distribution, but the velocity profile was quite homogeneous relative to the angular position (Figure 2.2C), indicating that the rapid flipping motion is mainly determined by the hydrodynamic environment, rather than the bonding profile**.** For spherical cells such as a leukocyte rolling on an endothelial layer, both the homogeneity of the velocity profile with the angular position and the heterogeneity of translocation velocity versus real-time were not obvious [58], suggesting there are hidden functions of the platelet's ellipsoid shape. Interestingly, the number of total bonds present in the system oscillated with no obvious accordance to either time or angular position (Figure 2.2D), which deviates from the intuition that more bonds may be formed during the residence period (long axis parallel to the wall surface) due to the larger contact area rather than during the fast flipping period. One possible explanation is the near-zero slip velocity reached by the transiently resting platelet, which reduces the

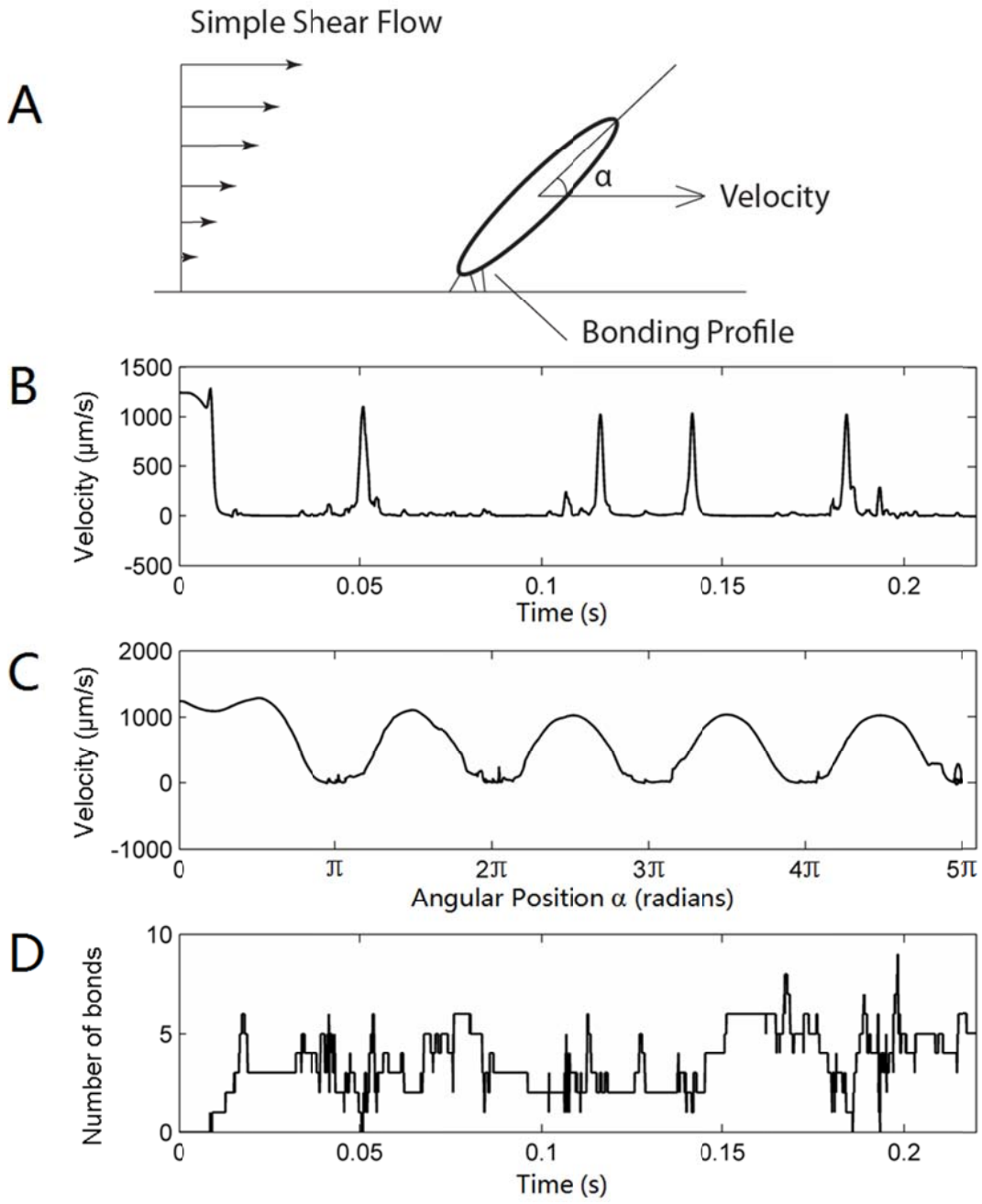

Figure 2.2 Translocation motion of a simulated platelet under simple shear of 1250 s^{-1} (A). The velocity is plotted versus time (B) and relative angular position (C). The bottom graph (D) shows the instantaneous number of bonds. Note: this simulation is based on a slip-bond-kinetic dissociation.

likelihood of new bond formation. Conversely, when the platelet rapidly rotates through the "standing" position the significant increase in relative slip velocity increases the probability of new bond formation despite the reduced contact area.

The translocational velocity (Figure 2.3A) was maintained at steady state at a lower range shear rate (100~250 s^{-1}). In this regime, one would expect that increasing the shear rate would increase the platelet-wall slip velocity and resulted in a larger number of GPIbα-vWF-A1 bonds formed. However, the additional number of bonds drags the platelet backwards and reduces its translocation velocity, which in turn would result in reduced bond formation rate. Such dynamic fluctuations caused by this self-stabilizing negative feedback mechanism made rolling platelets reach a steady translocation velocity of about 2.5 μm/s. At shear rates greater than 500 s^{-1}, the steady translocation velocity increases in a superlinear manner with increasing shear rate.

The tethering efficiency (Figure 2.3B) was measured by dividing the total number of tethering events with the total number of collision events. The results showed a similar pattern to the in-vitro bead-tethering assays [89] that the tethering efficiency reached maximum over a specific range of shear stress and deviation from that "optimal" tethering would result in a lower tethering efficiency. The initial increase in tethering efficiency was mainly caused by the increased slip velocity between the platelet and wall surface. Furthermore, the drop at the higher end of shear rate was most likely caused by an increase in the hydrodynamic force acting on the bonds, which reduces the bond life span and makes tethering events reversible (Figure 2.3C).

The number of bonds in the system showed a similar pattern to tethering efficiency and displayed an optimal range of shear rate (around $1250s^{-1}$) which maximized the total number of bonds formed (Figure 2.3D). This phenomenon resulted from the combined effects of the increased rate of bond formation and the decreased bond lifespan with incremental increases in shear rate.

The receptor density on the cell surface is a critical factor determining the platelet translocation pattern. Previous simulation studies dealing with leukocytes showed that increased receptor counts will reduce the rolling velocity and vice versa [101]. In our study, such sensitivity tests (groups with half or double the surface receptor density) were also performed. Reducing the total number of GPIbα receptors on the platelet surface by half increased the translocation velocity by 60%, lowered the tethering efficiency, and reduced average number of bonds as well as bond lifespan, while doubling the surface receptor density decreased the translocation velocity by 50%, increased the number of bonds and extended the bond lifetime (Figure 2.3). These results indicate that the ellipsoid-particle translocation system behaves similar to a spherical-particle translocation system in the sense that the mobility of the particle (cell) has an inverse relation to the receptor density on particle (cell) surface.

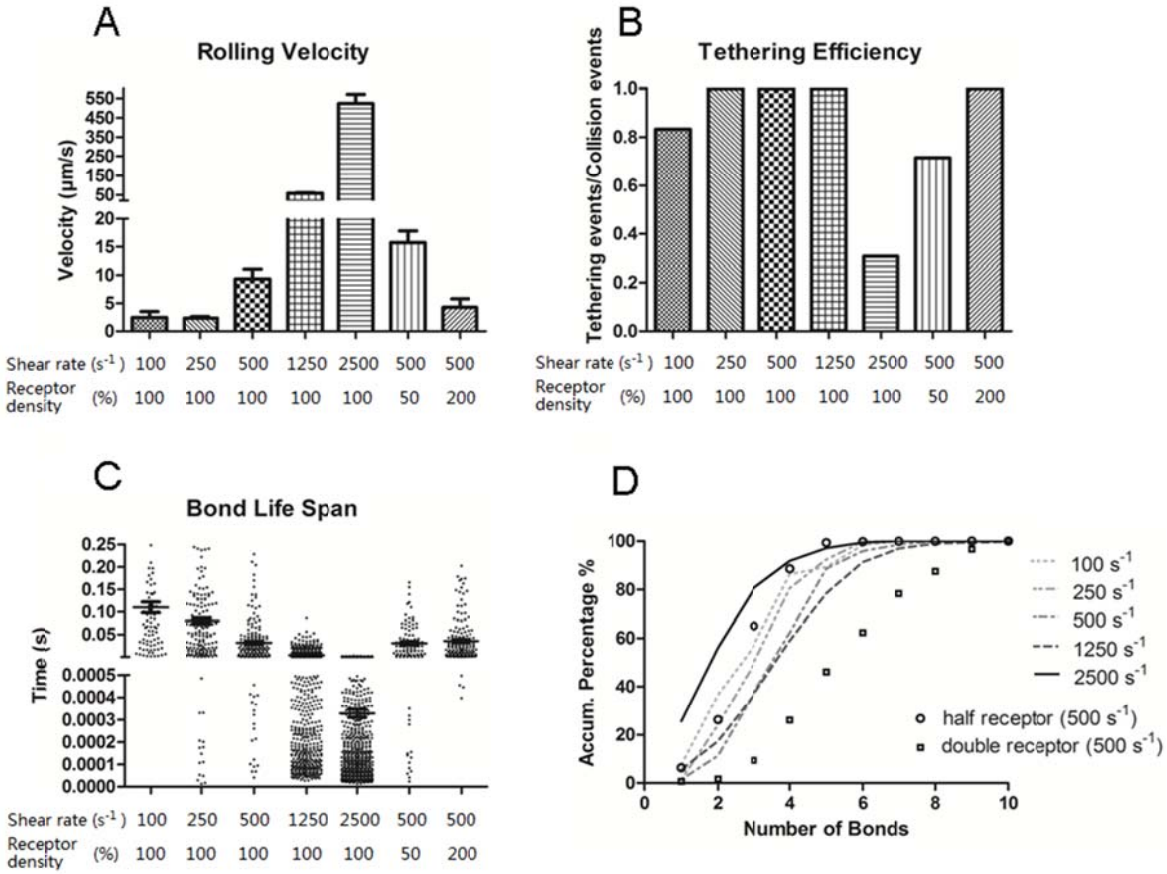

Figure 2.3 Simulation results of translocation velocity (A), tethering efficiency (B), bond life span (C) and the probability distribution of number of bonds (D) are shown at different shear rates. These simulations were based on slip bond kinetics. In A, the main bars indicate the mean rolling velocity and error bar shows the standard error. In C the longer line section shows the average bond lifetime with the two shorter lines indicating the standard error. Each simulation was repeated 10 times. In (A), the difference between the rolling velocity for $100s^{-1}$ and $250s^{-1}$ conditions is not significant ($P = 0.88$ from unpaired two-tailed t-test). For the comparison between $500s^{-1}$ and the double receptor $500s^{-1}$ conditions, $P = 0.102$. For any other two combinations, $P < 0.05$. In (C), the bond life span at the $100s^{-1}$, $250s^{-1}$, $500s^{-1}$ or $2500s^{-1}$ condition is significantly different than any other condition ($P < 0.05$).

Though slip-bond dissociation kinetics (based on the Bell Model) have been widely accepted, recently a catch-bond regime in the lower shear rate range (<1000 s^{-1}) was discovered and is said to show similar binding kinetics to selectin-ligand bonds [62,63] based on both in-vitro platelet and microsphere rolling assays. It is interesting that previous work – employing platelets, mammalian cells engineered to express the GPIbα receptor on the cell surface [85] or spherical beads – did not display catch-bond kinetics in the lower shear rate regime. Since multiscale simulation models are prone to experimental updates [102] , this new types of receptor-ligand bonding kinetics and reproduces expected results based on each mechanism, which is validated by in-vitro experimental data.

The intrinsic cross-linking formation rate constant, $k^0_{f,2\text{-}D}$, was re-determined using a similar method (indicated above) with a value of 0.05 $s^{-2}/\mu m$. The translocation velocity for the catch-slip combination kinetics is shown in Figure 2.4. Both the traditional slip-bond model (Bell Model) and the catch-slip combination model were plotted and compared with the experimental results of in-vitro platelet rolling assays [62]. The catch-slip combination model indeed generated a similar parabolic relationship between the translocation velocity and increasing shear rate. However, over the low shear rate range (100 - 500 s^{-1}), the translocation velocity differs by several orders of magnitude compared to experimental data. In order to explain this deviation, we examined the distribution of bond lifetimes under various bond forces (data from Auton, et al, 2010) [64]. It was shown that within the catch-bond regime (bond force < 20pN), the shortest lifetime for

the GPIbα-vWF-A1 bond is around 0.075 s where there is no net stress acting on the bond (bond force ~ 0pN). By assuming that there is no "jumping" period at any given time, i.e., there is at least one GPIbα-vWF-A1 bond existing at any moment, the fastest possible translocation velocity of the rolling platelet would happen in the scenario shown in the upright box of Figure 2.4A, where there was only one bond formed at the long axis end of the translocating platelet:

V_{max} = 2*R/0.075s = 26.7μm/s. (R is the major axis of the ellipsoid-shaped platelet.)

On average, we would expect at least a 50% drop in the maximum possible translocation velocity due to the multiple bonds formed as well as the random surface distribution of the GPIbα receptors (bonding profile).

Another reason for such deviation may come from the fact that the governing bond association equation (Eq. 8) may not truly represent the most bond-forming kinetics. Unlike dissociation rate, which can be more easily determined by tethering assays or atomic force microscopy, there is a lack of straightforward experimental methods to determine the association rate under flow condition. This may result in overestimates of the bond association rate in the lower predicted shear rate region, overpredicting the number of bonds in the system and a slower translocation velocity. Nevertheless, the translocation velocity from the simulations, though disparate from the experimental data, makes reasonable predictions based on this formula.

Figure 2.4B shows the duration of bonds under different shear rates. It is interesting to note that the average bond lifespan does not show an obvious parabolic pattern, which

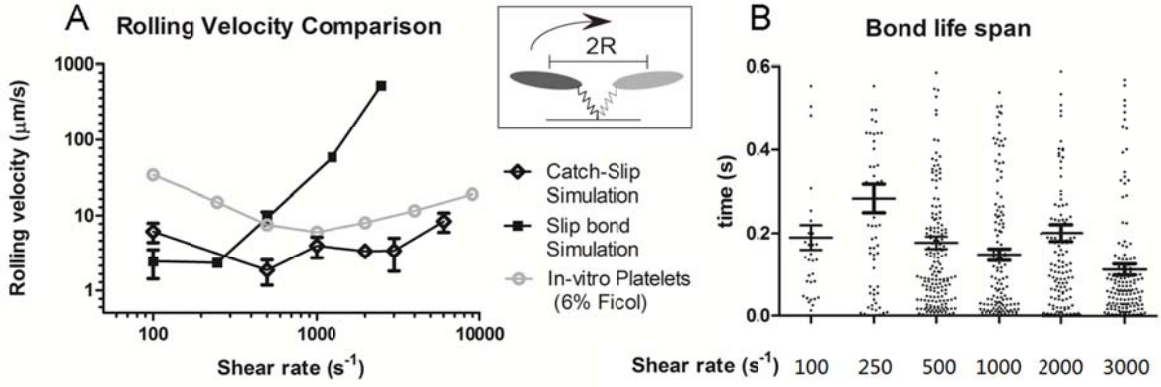

Figure 2.4 Simulation results of translocation velocity (A) and bond life span (B) based on catch-slip combination kinetics. In A, the main bars indicate the mean translocation velocity and error bar shows the standard error. The *in-vitro* experimental data is from Coburn et al [63]. In B, the longer line section shows the average bond lifetime with the two shorter lines indicating the standard error.

would reverse the trend of translocation velocity at different shear rates. One may argue that shorter bond life span would directly relate to faster rolling velocity. However, this statement may not always hold. There is an additional parameter, the average number of bonds existing between the rolling cell and the vessel wall, which also contributes to the translocation velocity. Reducing the bond lifespan will immediately increase the translocation velocity of the cell, however, because the bond formation rate is dependent on the 2D slip velocity between the bond-forming region on the cell and the vessel wall (Eq. 8), faster translocation velocities cause bonds to form faster, though not necessarily increase the average number of bonds existing at one moment since the bonds break faster as well. The quantitative change of the average number of bonds existing in the rolling event after a reduction in bond lifespan is thus a result of balancing the faster bond formation rate and faster bond breakage rate and can be predicted only by simulations or by calculation if a complete analytical model of the cell rolling existed. If the average number of bonds existing in the system truely increases, the distance that a cell will move in response to a single bond breakage event will be smaller, which attenuates the propelling effect of faster translocation velocity caused by shorter bond duration.

2.4 Two Platelet Hydrodynamic Interaction—with one adherent platelet on the vessel wall

The fast expansion of a platelet plug to cover the exposed sub-endothelial surface cannot be fulfilled if thrombus development is purely reliant on platelet/vessel wall interactions. In fact, an adherent platelet provides additional anchoring mechanisms to recruit flowing platelets to the site of injury to facilitate the process of thrombosis, which are strongly

associated with the characteristics of platelet collisions including: collision frequency, contact duration during a collision, and the extent of surface area on each interacting platelet that enters the particle-particle reactive zone. The contact duration and contact area can be combined to generate a metric – the time integral of contact area – that can be used to assess the probability of platelet-platelet adhesion during the hydrodynamic encounter between the upstream flowing platelet and the downstream immobilized platelet. Hundreds of collisions were simulated with different initial configurations of relative distances between the particle centroids in the y- (parallel to the wall plane, perpendicular to the direction of flow) and z-direction (perpendicular to the wall plane). Significant trends between the relative position of the two platelets to the duration and quality of their interactions were found, which serve as indicators of growth potential of the "micro-thrombi". The detailed hydrodynamic and geometrical information during two-platelet interactions are also summarized.

Collision simulations were initiated with two different initial distances (either 10μm or 20μm in the direction of flow) between the centroids of the two platelets, which would, in the absence of flow disturbances from the downstream adherent platelet, result in two limiting orientations ("perpendicular" orientation and "parallel" orientation) for the flowing platelet (see Figure 2.5A, E). A "collision" was defined as any event in which the distance between the two platelet surfaces became less than the maximum reactive distance (260 nm), an approximation of the length of the trimolecular bond integrin $\alpha_{IIb}\beta_3$ – vWF - integrin $\alpha_{IIb}\beta_3$ which is comparable of the length of GPIb - vWF- GPIbα trimolecular bond as used in our previous studies [13] (integrin $\alpha_{IIb}\beta_3$ is comparable in

size to GPIb, with the former slightly smaller than 30nm [103] and the latter slightly larger than 30nm [97]). Threshold distance as the length of integrin $\alpha_{IIb}\beta_3$ - Fibrinogen- integrin $\alpha_{IIb}\beta_3$ bond, which supports the platelet- platelet firm adhesion, is because 1) It has been shown that vWF can support platelet adhesion via interaction with activated integrin $\alpha_{IIb}\beta_3$ [104] and 2) the single fibrinogen molecule spans only about 50nm [105] which is much smaller than the average size of vWF multimers; this gives the likelihood that an integrin $\alpha_{IIb}\beta_3$ – vWF - integrin $\alpha_{IIb}\beta_3$ bond has a greater chance to establish before forming the integrin $\alpha_{IIb}\beta_3$ - Fibrinogen- integrin $\alpha_{IIb}\beta_3$ bond during platelet collision. The contact area was calculated by summation of the surface patches on the flowing platelet, which had "collided" with the adherent platelet. Note that all of the simulations related to one flowing platelet colliding with the immobilized platelet on the wall were performed at a shear rate of 5000 s^{-1}. Because of the linearity of Stokes' flow, collision patterns under variable shear rates will be similar and can be inferred directly from these simulation results. The collision grid map showed significant differences between the two different initial configurations. The initial configuration where the flowing platelet tended to project its edge into the second platelet had not only a larger collision regime in the z-direction, but also showed approximately 10% longer contact time, 15% larger contact area and 15% larger time integral of contact area respectively (Figure 2.5 scale bars). Overall, the integrated contact duration was larger for platelets flowing closer to the vessel wall, such as would be created by the margination effect caused by the existence of larger blood cells such as erythrocytes. There was a sharp decrease in the time integral of contact area when the initial z-direction deviation of the two platelet centroids extended beyond a threshold distance of 0.5 μm (Figure 2.5 D). Interestingly, for both cases, the

contact time reached a maximum when the two platelets started with a separation distance of 1.7 μm along the y axis, which differs from the expectation that gliding directly over an immobilized platelet provides the longest contact time (Figure 2.5 B, F). This is likely due to the fact that, when the flowing platelet glided over the immobilized platelet, the lubrication force generated by the thin fluid layer between the platelet surfaces pushed the flowing platelet further away from the vessel wall, as compared to the situation where the position of the platelet pair had a deviation in the y-direction. The resulting differences in the z-coordinates gave the gliding platelet a greater velocity, based on the bulk simple shear flow profile. On the other hand, the maximum contact area reached a peak value when the flowing platelet's trajectory passed right above the adherent platelet, which, together with the resulting contact time, resulted in a more uniformly-distributed contact area-time integral along the y-direction (Figure 2.5C, D, G, H). The comparison of this grid map to the grid map resulting from a free-flowing platelet collision [14] shows that the platelet's unique ellipsoid shape encourages better interaction when one is tethered to the vessel wall, which to some degree, reduces the probability of flowing platelets to form homotypic aggregates under physiologically high shear stress [106,107].

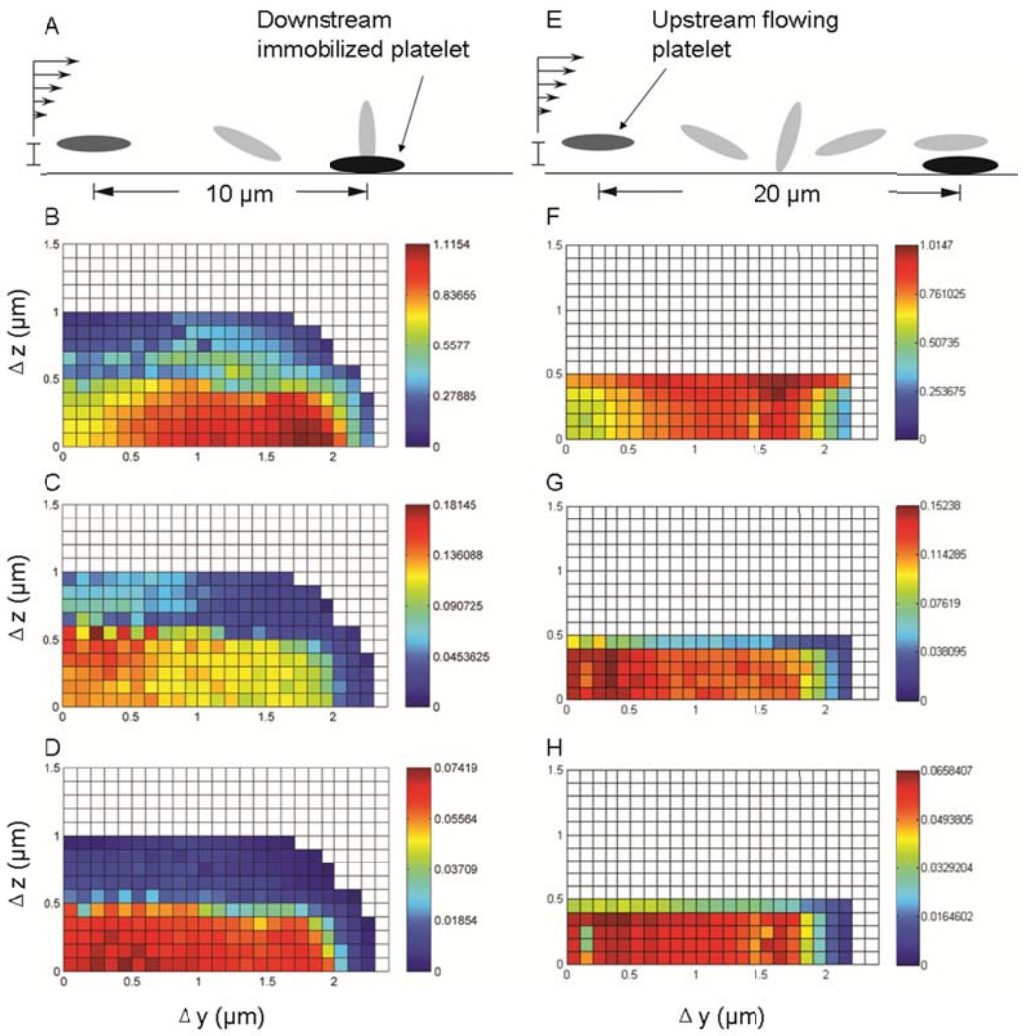

Figure 2.5 The color-scaled binary collision map. Each grid point represents an individual collision experiment with the flowing platelet starting at a specific location represented by δx, δy and δz. A-D (E-H) are results of binary collisions between a flowing platelet 10μm (20μm) upstream of a downstream immobilized platelet. The grey ellipsoids in A, E represent the non-disturbed flowing platelet trajectory path (with adjusted length scale). B, F are the platelet contact time, with the unit associated with numbers shown on the color bar as micro-seconds. C, G are the contact area for the flowing platelet (unit with numbers μm^2). D, H are the time integral of contact area for the flowing platelet (μm^2 ms).

The contact zone of the immobilized platelet was examined in detail to identify the region on the immobilized platelet surface where the flowing platelet comes into contact. Figure 2.6 shows the mapping of the contact area of the surface of the immobilized platelet and each sub-figure is resulted from a series of parallel collision simulations with the flowing platelet started at a specific height (z-coordinates) and position (only x-coordinates). The results match the expectation that proximity of the flowing platelet to the vessel wall leads to longer contact time. However, when the circulating platelet was very close to the vessel wall, it never contacted the top, central part of the adherent platelet. Increasing the initial height (z-coordinate) of the flowing platelet shifted the contact zone on the immobilized platelet from the upstream region towards the central top and downstream regions, but also reduced the contact quality (Figure 2.6A-D). Since longer contact time resulted in higher chances of forming receptor-ligand bonds (fibrinogen, vWF mediated integrin $\alpha_{IIb}\beta_3$ bridging), this unique contact character reduced the probability for the flowing platelet to stack directly above the immobilized platelet**.** Instead, platelets tend to remain longer in the peripheral region of the immobilized platelet, approaching a side by side orientation to each other and gaining better coverage efficiency at the injury site while reducing likelihood of decreasing the effective vessel diameter and potential vessel occlusion. As described above, the collision pattern is sensitive to the x-direction separation between the two platelets, thus we also mapped out the mapping of contact

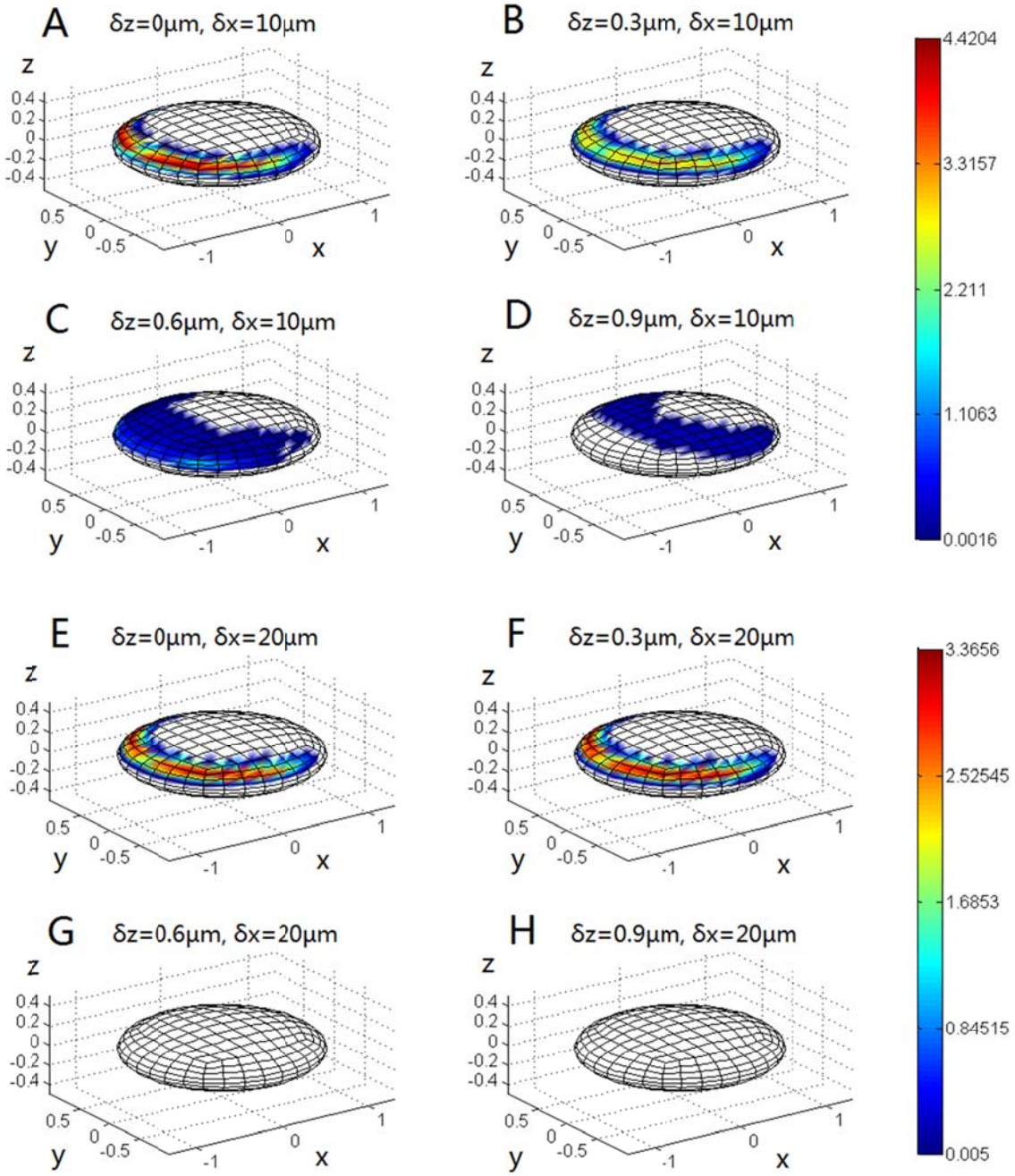

Figure 2.6 The mapping of the contact region on the immobilized platelet for different starting positions of the flowing platelet. The color is scaled to represent the contact time (ms) and the length unit of the Cartesian coordinates is μm.

area for collision series with an x-axis deviation of 20μm. Figure 2.6E-H confirms the results shown in Figure 2.5 that there is no contact when the flowing platelet is at least 0.5μm higher than the stationary platelet. The scale bars show that the overall trend of the collision quality (i.e., time and area) is better for the 10μm condition, which is consistent with the results indicated by the color map in Figure 2.5.

It is evident from Figure 2.6 that the flowing platelet approaches the immobilized platelet mostly in the upstream region. It is interesting to consider how the flowing platelet is able to contact and deposit on the injured surface near the central and downstream regions of the immobilized platelet. Figure 2.7 shows a vector plot representing the velocity of the centroid motion of the flowing platelet starting from a horizontal orientation (long axis parallel to the wall surface) 10μm upstream of the immobilized platelet. The arrows represent the relative motion of the flowing platelet for each collision event, with the circled dots showing the intercept (height) of the trajectories to the plane x = -3μm. The closer that the flowing platelet is to the vessel wall (plane z = 0), the slower the platelet convection, and importantly, the more altered the directional change of the trajectories. Figure 2.7A shows that for flowing platelets that glide over the immobilized platelet, a slight deviation in the y-coordinates pushed the flowing platelet up and more towards the side (outward, or larger y-coordinates). However, when the flowing platelet starts with a y-coordinate deviation large enough to pass by the side of the adherent platelet without collision, the disturbed flow pulls the flowing platelets inward close to the downstream end of the immobilized platelet (Figure 2.7A).

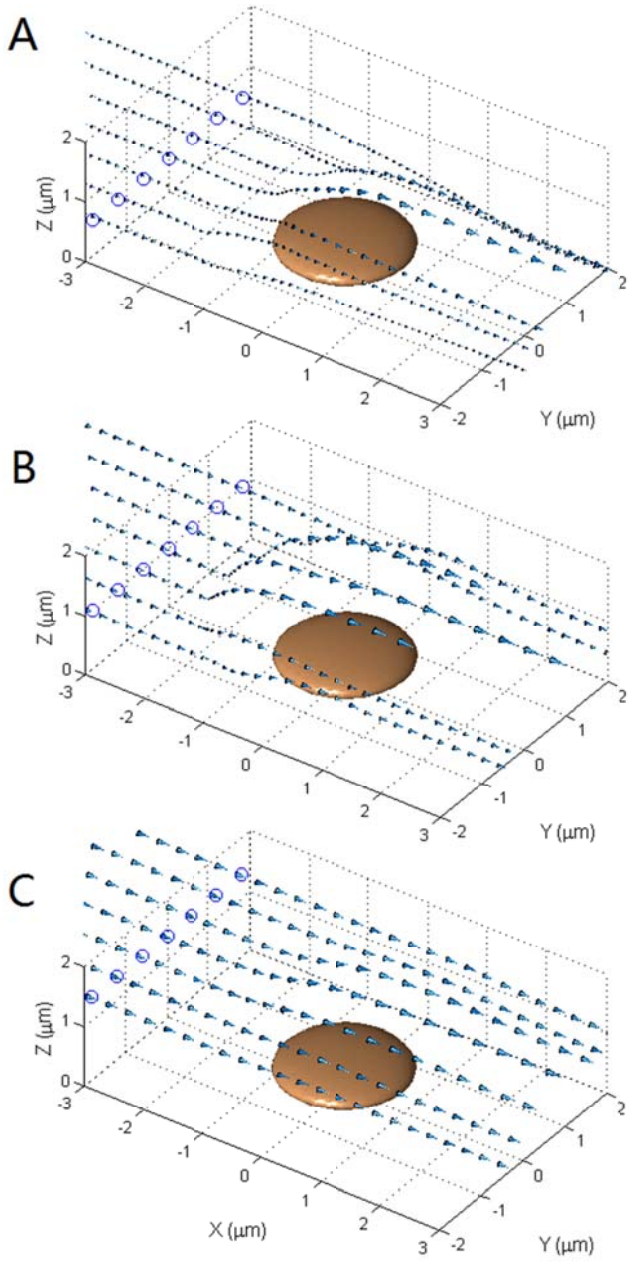

Figure 2.7 The velocity vector for the center of the flowing platelet when flowing past an adherent platelet. A, the flowing platelet was started at 10 μm upstream with a δz of 0.2 μm to the immobilized platelet. B, similar to A, with a δz of 0.6 μm. C, similar to B, with a δz of 1.0 μm.

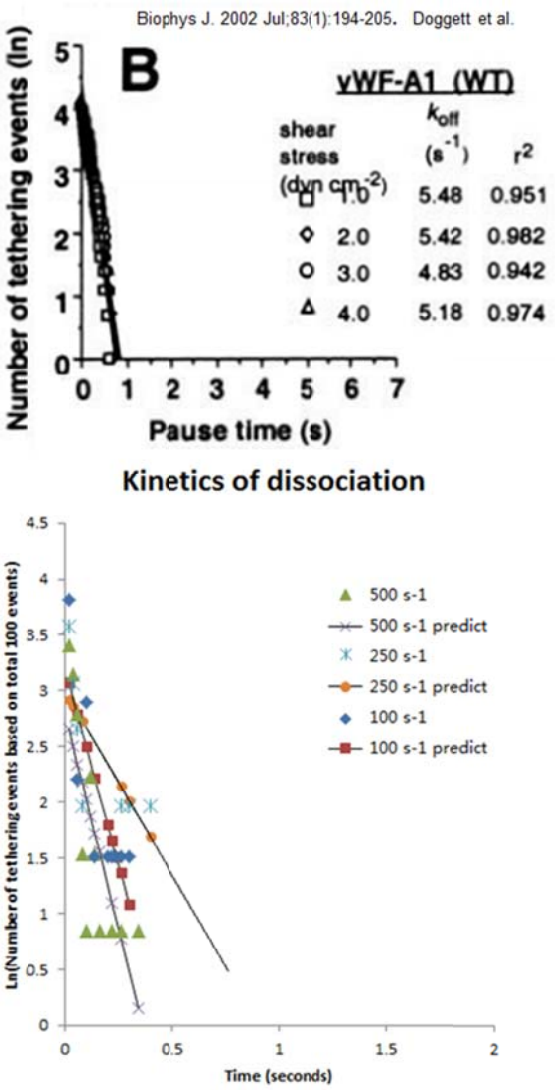

Figure 2.8 Cell tethering experiment comparing to in vitro result. The top figure is the published data [60] where wild-type platelet has been applied to measure the tethering duration. The bottom figure is generated by simulations to measure the tethering duration versus the relative frequency of appearance. The predict line in the bottom figure is just the data point in the top figure.

From the bond kinetics of Bell Model, it actually described a relationship between the duration of the bond and its relative frequency of appearance if such bond does form. We can also tell from Bell Model that there exists a linear relationship between the log relative frequency and the bond duration. In our study, such relationship can be verified by tethering experiments where only one receptor-ligand bond is allowed to form for each simulation. By setting the bin values (bond duration time) and calculate the frequency of events happen within adjacent bin values, and log plot it with bond duration, we can clearly see a linear relationship between the two, and such linear relationship matches what researched found out in experiments (Figure 2.8).

2.5 Conclusion

We describe a multiscale model that incorporates detailed hydrodynamics as well as experimentally based receptor-ligand binding kinetics. This model is capable of revealing some of the subtle physiological processes during hemostasis, such as platelet translocation and interaction. It also demonstrates some of the mechanisms that platelets employ to efficiently form clots to seal wounds on the vessel wall, including the interaction between flowing and adherent platelets, as well as the characteristics of its translocational behavior. Importantly, the stability and versatility of our model suggests the future application of predicting bleeding phenotypes and multiple physiological states, such as a diseased status or therapeutic condition. Once additional types of platelet receptor-ligand interactions are incorporated, we will be able to simulate more comprehensive processes from platelet translocation to irreversible adherence, followed by the formation of platelet aggregates.

CHAPTER 3: SIMULATION OF PLATELET, THROMBUS AND ERYTHROCYTE HYDRODYNAMIC INTERACTIONS IN A 3D ARTERIOLE WITH *IN VIVO* COMPARISON

Cylindrical blood vessels, ellipsoid platelets and biconcave-shaped deformable erythrocytes (RBCs) are important participants in hemostasis and thrombosis. However, due to the challenge of combining these components in simulation tools, few simulation studies have included all of them in realistic three-dimensional models. In the present study, we apply a recently developed simulation model to incorporate these components and analyze the flow in a thrombotic tubular arteriole, particularly the detailed hydrodynamic interactions between the thrombus shape, RBCs and platelets. It was found that at certain azimuth positions, the velocity drops in the proximity of both the upstream and downstream edge of the thrombus, which is accompanied by a rapid velocity increase in the narrowed region. The RBCs alter the flow profiles significantly from the typical low Reynolds (Re) number flow, and also enhance the deposition of free flowing platelets onto the thrombus. By evaluating the platelet-thrombus interaction and platelet-RBC interaction together, several mechanisms of platelet deposition augmentation are identified. With *in vivo* data comparison, our model illustrates the potential of future thrombosis studies that incorporate detailed receptor-ligand adhesion modules.

3.1 Introduction

Thrombosis, the pathological process of the hemostatic system to form unwanted blood clots, can impair blood flow to vital organs and ultimately result in stroke or myocardial infarction [5]. Although widely studied, the complicated ensembles of the hemostatic system, together with measurement limitations, motivate the development of computer simulations of the physiological processes of hemostasis and thrombosis. Current hemostatic simulation models consist of one or more of the following components: hydrodynamics, coagulation cascade, platelet activation, fibrin network, cell mechanics or receptor-ligand adhesion [108]. Some of these modules utilize a "systems biology" approach where the physical elements are described by concentration fields with advection and diffusion in the fluid (plasma) [6]. Others take the mechanics of those elements into consideration, such as shape, density and deformability [6,108].

The physical contact between flowing platelets and the injured vessel surface (including the developing thrombus) is a key event in the progress of thrombosis. Various simulation studies have been performed in an attempt to represent this hydrodynamic interaction. For instance, Mody and King applied the CDL-BIEM method to analyze the near-wall motion of a platelet in 3D and discovered three distinct regimes of platelet-wall hydrodynamic interactions [34]. Later, these authors simulated the platelet-platelet interaction near a wall and demonstrated the importance of the unique spheroid shape to the physiological function of the platelet [14]. Wang et al. used an immobilized platelet to address the early initiation of a micro-thrombus and studied the hydrodynamic interaction between an immobilized and flowing platelet [102]. Other platelet-vessel wall

interaction models combine hydrodynamics with cell-wall adhesion. For example, Fogelson used an immersed boundary method to study the platelet-wall interaction with an adhesion module in 2D [11]; Mori et al. utilized Stokesian Dynamics to simulate platelet-wall interactions and thrombus development in 2D [25]. One of the first platelet-wall interaction models in 3D was presented by Pivkin et al., where the authors analyzed different thrombus growth patterns under different platelet activation delay times [8].

Interestingly, the platelet and vessel wall are not the only determinants in thrombus formation. Platelet margination, an elevated distribution of platelets towards the peripheral region of the vessel lumen, was discovered decades ago [109] and is believed to be mainly caused by the significant volume fraction of RBCs in whole blood. Simulation studies revealed that the high deformability of RBCs as well as the finite size of platelets compared to RBCs may be two reasons for such margination effects [15,110].

Experimental data comparison serves as an important process to evaluate simulation models. In recent years, due to the fact that more detailed models have been established along with more precisely controlled and measured experimental systems, such comparison is shifting from qualitative to quantitative. Flow chamber assays are a good source of *in vitro* data and examples have been shown to verify human platelet-wall interaction models [73]. Mouse models are typically used for generating *in vivo* data and are preferred by clinical investigators. However, they are limited by the fact that all hemostatic components are derived from mice [111]. A biological platform has been developed that specifically addresses this issue, by enabling the *in vivo* assessment of

human platelet mediated thrombus formation [112]. This was accomplished by genetically modifying the A1 domain of murine VWF (VWF-A1) so that it interacts with human but not mouse GPIbα. Consequently, animals have a bleeding phenotype that can be corrected by the administration of human platelets. This humanized mouse model serves the purpose of *in vivo* comparison to our simulation model as we were able to monitor in real-time the dynamics of human platelet interactions with laser-injured arterioles.

In the present study, we utilized a high-efficiency 3D boundary integral method which evaluates the surface integrals using an *O(N logN)* particle-mesh Ewald (PME) approach [77] to simulate hydrodynamic interactions between a thrombus, flowing platelets, and surrounding deformable red blood cells (RBCs) with elastic membranes. The plasma flow at different locations inside the cylindrical vessel wall with an existing thrombus of various shapes was explored; the hydrodynamic effect of various degrees of stenosis was examined and compared to *in vivo* data; and the correlation between RBC-platelet interaction and platelet-vessel wall interaction was also assessed.

3.2 Materials and Methods

All animal experiments were carried out in accordance with institutional IACUC committees of Cornell University and Columbia University, following protocols approved by both institutions' IACUC.

3.2.1 Hydrodynamic Calculation

The hydrodynamic calculation uses a previously reported fast boundary-integral algorithm for numerically computing the flow solution [77]. In this approach, the Green's functions of the flow equation, which is linear in the viscous limit appropriate for the low Reynolds numbers of the microcirculation, are built into integral expressions, which relate the velocity to the forces exerted on the fluid by the elastic cells and the vessel walls. Note that while the fluid mechanics are linear, the combined cell-fluid system has significant geometric nonlinearity, so the collective behavior of the cellular is expected to deviate significantly from what would be predicted overall for a linear Stokes flow. The basic analytic formulation has been available for some time and is summarized clearly by Pozrikidis [113]. To discretize this formulation, the vessel walls and cell surfaces are represented by discrete elements. With such a discretization, numerical evaluation of the integral expressions is tantamount to forming a dense linear system to solve. It is dense because of the long-range interactions embodied in the Green's function: all points on all surfaces induce velocities at all other points in the domain. This is prohibitively expensive to evaluate directly for systems of the size targeted by the presented study, scaling at least as $O(N^2)$, where N is the number of discrete points. However, an Ewald splitting of the Green's function facilitates an approximate, though accurate, discretization that has a much better $O(N \log N)$ complexity [77,114]. This employs a periodic form of the Green's function kernels, which is advantageous in the present cases since the target simulation is streamwise periodic, and not restrictive in the other directions since the presence of the vessel wall breaks any periodic influence.

The simulation scheme is based on the standard boundary-integral solution of Stokes equation. The velocity at a point x in the plasma is given by:

$$u_j(\boldsymbol{x}) = U_j - \frac{1}{8\pi\mu}\iint_{W\cup D} f_i(\boldsymbol{y})G_{ij}(\boldsymbol{y},\boldsymbol{x})dS(\boldsymbol{y}) + \frac{1-\lambda}{8\pi}\iint_D u_j(\boldsymbol{y})T_{ijk}(\boldsymbol{y},\boldsymbol{x})n_k(\boldsymbol{y})dS(\boldsymbol{y})$$

(1)

where D to be the union of all cell membrane surface, W is the vessel wall, u_j is the j-direction component of the plasma velocity, $U_j$is the velocity of a specified driving flow, f_i is the traction force exerted on the cell membrane or vessel wall, μ is the plasma viscosity, λμ is the cytosol viscosity, G_{ij} is the singularity solution of Green's function due to a point force on the bounding surface and T_{ijk} is the stress corresponding to flow produced by a point force.

The second integral on the RHS of Eq.1, also known as the double-layer potential, experiences a jump as $\boldsymbol{x}$ approaches the cell surface continuous on the cell surface and gives the velocity of cell surface:

$$u_j(\boldsymbol{x}) =$$

$$\frac{2}{1+\lambda}U_j - \frac{1}{4(1+\lambda)\pi\mu}\iint_{W\cup D} f_i(\boldsymbol{y})G_{ij}(\boldsymbol{y},\boldsymbol{x})dS(\boldsymbol{y}) + \frac{1-\lambda}{4(1+\lambda)\pi\mu}\iint_D u_j(\boldsymbol{y})T_{ijk}(\boldsymbol{y},\boldsymbol{x})n_k(\boldsymbol{y})dS(\boldsymbol{y})$$

(2)

where $\boldsymbol{x} \in D$ is any given point on the cell surface.

Discretization the first integral on the RHS of Eq.2 by representing the membrane of each cell by a set of collocation points and approximating using a quadrature with weights w^β for each collocation point β gives:

$$\iint_{W \cup D} f_i(\boldsymbol{y}) G_{ij}(\boldsymbol{y}, \boldsymbol{x}^{\alpha}) dS(\boldsymbol{y}) \cong \sum_{\beta} G_{ij}\left(\boldsymbol{y}^{\beta}, \boldsymbol{x}\right) f_i^{\beta} w^{\beta} \quad (3)$$

The RHS of Eq.3 is a matrix-vector multiplication which can be represented by $\mathbf{A}\vec{\boldsymbol{f}}$ where $\mathbf{A}$ is the matrix containing Green's function solution and the list of all components of all the surface tractions. A similar process can be taken on the second integral of Eq.2 and thus the entire Eq. 2 then takes the form:

$$\vec{\boldsymbol{u}} = c\boldsymbol{U} + \mathbf{A}\vec{\boldsymbol{f}} + \boldsymbol{B}\vec{\boldsymbol{u}} \text{ or } \mathbf{A}\vec{\boldsymbol{f}} + \boldsymbol{B}\vec{\boldsymbol{u}} = \boldsymbol{C} \quad (4)$$

Apply the no-slip boundary condition to Eq.1:

$$0 = U_j - \frac{1}{8\pi\mu} \iint_{W \cup D} f_i(\boldsymbol{y}) G_{ij}(\boldsymbol{y}, \boldsymbol{x}) dS(\boldsymbol{y}) + \frac{1-\lambda}{8\pi} \iint_{D} u_j(\boldsymbol{y}) T_{ijk}(\boldsymbol{y}, \boldsymbol{x}) n_k(\boldsymbol{y}) dS(\boldsymbol{y}) \quad (5)$$

where $\boldsymbol{x} \in W$. Use the same idea we can express Eq.5 in the following format similar to Eq.4:

$$\mathbf{A}_*\vec{\boldsymbol{f}} + \boldsymbol{B}_*\vec{\boldsymbol{u}} = \boldsymbol{C}_* \quad (6)$$

If we combine Eq.4 and Eq.6, we have:

$$\begin{pmatrix} \boldsymbol{A} & \boldsymbol{B} \\ \boldsymbol{A}_* & \boldsymbol{B}_* \end{pmatrix} \begin{pmatrix} \boldsymbol{f} \\ \boldsymbol{u} \end{pmatrix} = \begin{pmatrix} \boldsymbol{C} \\ \boldsymbol{C}_* \end{pmatrix} \quad (7)$$

A staggered time integration method updates the position of the cell surface collocation points from $t^{n+1} = t^n + \Delta t$ as following:

(i) Solve the surface velocity $\boldsymbol{u}^n$ at time step n from

$$\boldsymbol{B}^n\boldsymbol{u}^n = \boldsymbol{C}^n - \boldsymbol{A}^n\boldsymbol{f}^n \quad (8)$$

(ii) Update the cell surface coordinates by the forward Euler scheme

$$\boldsymbol{x}^n = \boldsymbol{x}^n - \Delta t\boldsymbol{u}^n \quad (9)$$

(iii) Update the wall drag force by solving

$$\boldsymbol{A}_*^{n+1}\boldsymbol{f}^{n+1} = \boldsymbol{C}_*^{n+1} - \boldsymbol{B}_*^{n+1}\boldsymbol{u}^n \tag{10}$$

The Green's function solution G_{ij} and stress T_{ijk} for periodic boundary conditions are calculated as an Ewald sum [115] by decomposing them into short-range singular (sr) and smooth (sm) parts first:

$\boldsymbol{G} = \boldsymbol{G}^{sr} + \boldsymbol{G}^{sm}$ and $\boldsymbol{T} = \boldsymbol{T}^{sr} + \boldsymbol{T}^{sm}$

$$G_{ij}^{sr}(\boldsymbol{x},\boldsymbol{y}) = \sum_{\boldsymbol{a}} erfc(\tilde{r})\left(\frac{\delta_{ij}}{r} + \frac{r_i r_j}{r^3}\right) + \frac{2}{\sqrt{\alpha}}\sum_{\boldsymbol{a}} e^{-\tilde{r}^2}\left(\frac{r_i r_j}{r^3} - \delta_{ij}\right) \tag{11}$$

Where $\boldsymbol{a} = (n_1 L_1, n_2 L_2, n_3 L_3)$ for integer $n_{1,2,3}$, $\boldsymbol{r} = \boldsymbol{x} - \boldsymbol{y} + \boldsymbol{a}$ is the vector of separation, and $\tilde{\boldsymbol{r}} = \sqrt{\pi/\alpha}\boldsymbol{r}$ is non-dimensional. The corresponding smooth part of $\boldsymbol{G}$ is

$$G_{ij}^{sm}(\boldsymbol{x},\boldsymbol{y}) = \frac{2\alpha}{V}\sum_{\mathbf{k}\neq 0}\Phi_1(\tilde{k}^2)(\tilde{k}^2\delta_{ij} - \tilde{k}_i\tilde{k}_j)e^{i2\pi\mathbf{k}\cdot(\boldsymbol{x}-\boldsymbol{y})} \tag{12}$$

Where $\mathbf{k} = (n_1/L_1, n_2/L_2, n_3/L_3)$ is the wave number and $\tilde{\boldsymbol{k}} = \sqrt{\pi\alpha}\mathbf{k}$ is non-dimensional. The function Φ_1 in Eq.11 is an incomplete γ-function defined as

$$\Phi_\gamma(z) = \int_1^\infty e^{-zt}t^\gamma dt \tag{13}$$

The similar decomposition can be applied to T_{ijk} as well

$$T_{ijk}^{sr}(\boldsymbol{x},\boldsymbol{y}) = \frac{8\sqrt{\pi}}{\alpha}\sum_{\boldsymbol{a}}\Phi_{\frac{3}{2}}(\tilde{r}^2)\tilde{r}_i\,\tilde{r}_j\tilde{r}_k \tag{14}$$

$$T_{ijk}^{sm}(\boldsymbol{x},\boldsymbol{y}) =$$

$$\frac{2\alpha}{V}\sum_{\mathbf{k}\neq 0}(i2\pi)\left(k_i\delta_{jk} + k_j\delta_{ik} + k_k\delta_{ij}\right)\Phi_0\left(\tilde{k}^2\right)e^{i2\pi\mathbf{k}\cdot(\boldsymbol{x}-\boldsymbol{y})} +$$

$$\frac{\alpha^2}{\pi V}\sum_{\mathbf{k}\neq 0}(i2\pi)^3 k_i k_j k_k \Phi_1\left(\tilde{k}^2\right)e^{i2\pi\mathbf{k}\cdot(\boldsymbol{x}-\boldsymbol{y})} \tag{15}$$

The Ewald parameter α determines the length scale of the decomposition. The short-range part $\boldsymbol{G}^{sr}$ and $\boldsymbol{T}^{sr}$ decays exponentially with separation distance when $\tilde{r} \gg 1$, so it is truncated at short distance without introducing significant error. The smooth component is calculated by the smooth particle-mesh Ewald sum (SPME) method [114,116] which has a central idea of calculating the smooth Fourier Ewald sum on a uniform Cartesian mesh using fast Fourier transforms. More details about short-range and smooth components can be found in previous studies [77].

3.2.2 Cell Mechanics

The cell membranes were each discretized with a structured mesh interpolated by spherical harmonic basis functions, which were used to evaluate the elastic stresses. The membranes were mechanically modeled as elastic shells [117], which strongly resists areal dilatation and has a relatively weak resistance to in-plane shear. A bending resistance was also employed. The elastic parameters are those of Pozrikidis [75], which have been used with this simulation tool to reproduce the effective viscosity versus diameter for flow in round tubes of diameters 5μm up to about 30μm [77]. While this or any constitutive model will be unable to reproduce all conceivable red blood cell behaviors, this one is widely used and has been validated for flow in the present regime.

The spherical harmonic basis functions provide excellent resolution and convergence [77]. Since they facilitate error-free interpolation to finer meshes, they also enable a de-aliasing procedure for stabilization without the addition of numerical dissipation or filtering, which will in general degrade solution fidelity. The resulting scheme is both

accurate and robust, so we can choose the resolution needed to achieve necessary accuracy for meeting objectives with relatively little regard to maintaining numerical stability. The resolutions used in the present simulations are consistent with those used previously and in other studies [118,119].

The platelets were modeled as rigid ellipsoids, with shape and size matching that used in past Platelet Adhesion Dynamics (PAD) studies [13,108]. This is appropriate given the relative stiffness of platelets, but introduces an additional challenge to the numerical solution since it renders the basic formulation singular [113]. We resolve this, as we have in studies of transport of magnetic nanoparticles [119], using the methods discussed by Kim & Karrilla [33] and Pozrikidis [113], by which the solid-body modes are projected out of the system and solved separately before being reincorporated to evolve the platelet positions. Our implementation was validated against the results of Hashimoto [115] for drag on an array of spheres (data not shown).

The vessel walls were represented by linear triangular boundary elements.

The cell surface is represented by a series of points expressed as a function of latitude angle $\theta \in [0, \pi]$ and longitude angle $\phi \in [0,2\pi]$

$$x(\theta,\phi) = \sum_{n=0}^{N-1} \sum_{m=0}^{n} \bar{P}_n^m(cos\theta)(a_{nm}\, cos\, m\phi + b_{nm}\, sin\, m\phi) \quad (16)$$

The equation generate N^2 total number of spherical harmonic modes, where a_{nm} and b_{nm} are expansion coefficients and $\bar{P}_n^m = \frac{1}{2^n n!}\sqrt{\frac{(2n+1)(n-m)!}{2(n+m)!}}(1-x^2)^{\frac{m}{2}}\frac{d^{n+m}}{dx^{n+m}}(x^2-1)^n$ are normalized associated Legendre polynomials [120].

On the cell surface, local coordinates are defined by the two tangents $\mathrm{a}_{1,2}$ and the surface normal a_3:

$$\mathrm{a}_1 = \frac{\partial x}{\partial \theta}, \mathrm{a}_2 = \frac{\partial x}{\partial \theta}, \mathrm{a}_3 = n = \frac{\mathrm{a}_1 \times \mathrm{a}_2}{|\mathrm{a}_1 \times \mathrm{a}_2|} \quad (17)$$

Each RBC has a stress-free biconcave reference shape set with a standard function form [75,76]. The local deformation of the membrane is described by the surface deformation tensor **F** that maps the two reference tangents a_k^R to a_k:

$$\mathbf{F} = \sum_{\alpha=1}^{2} \mathrm{a}_\alpha \otimes \mathrm{a}_\alpha^R \quad (18)$$

The neo-Hookean elastic strain energy is:

$$\mathrm{W} = \frac{E_S}{4}\left(\frac{1}{2}I_1^2 + I_1 - I_2\right) + \frac{E_D}{8}I_2^2 \quad (19)$$

where $I_1 = \lambda_1^2 + \lambda_2^2 - 2$, $I_2 = \lambda_1^2\lambda_2^2 - 1$ and $\lambda_{1,2}$ are the eigenvalues of the left Cauchy-Green tensor $\boldsymbol{V}^2 = \mathbf{F} \cdot \mathbf{F}^{\boldsymbol{T}}$, E_S is the elastic shear modulus and E_D is the dilatation modulus resisting surface area changes. The corresponding in-plane Cauchy stress tensor is:

$$\tau = \frac{E_S}{2J_S}(I_1 + 1)\boldsymbol{V}^2 + \frac{J_S}{2}(E_D I_2 - E_S \boldsymbol{P}) \quad (20)$$

where $\boldsymbol{P} = \boldsymbol{I} - \boldsymbol{n} \otimes \boldsymbol{n}$ is the surface projection tensor and J_S=$\lambda_1\lambda_2$ is the dilatation.

The linear isotropic model used for the bending moment M is

$$M_{\alpha\beta} = -E_B(b_{\alpha\beta} - b_{\alpha\beta}^R) \quad (21)$$

for α, β=1,2, where E_B is the bending modulus and $b_{\alpha\beta} = \mathrm{a}_{1,2} \cdot \boldsymbol{n}$ is the covariant component of the curvature tensor.

Apply the Stokes theorem to the local torque balance gives the expression of the surface transverse tensor Q and the in-plane tension tensor N:

$$M_{\alpha\beta}^{|\alpha} - Q_\beta = 0,\ e_{\alpha\beta}(N_{\alpha\beta} - b_{\alpha\lambda}M_{\lambda\beta}) = 0 \quad (22)$$

where the superscript '|α' denotes a covariant derivative. By a local force balance, the hydrodynamic surface traction f used in Eq.2 is

$$N_{\alpha\beta}^{|\alpha} - b_{\alpha\beta}Q_\alpha + f^\beta = 0,\ \alpha, \beta=1,2 \quad (23)$$

$$Q_\alpha - b_{\alpha\beta}N_{\alpha\beta} + f^3 = 0 \quad (24)$$

where f^3 denotes the normal component of $\boldsymbol{f}$.

3.2.3 Simulation Domain

We consider a streamwise periodic cylindrical vessel with diameter 15μm and length 45μm. In a vessel of this size, the Fahaeus effect [121,122] can be quite significant. The hematocrit value (volume fraction of RBCs in the blood, abbreviated as Hct) can drop from 40~45% in arteries of normal adults to 10~20% in small capillaries. A Hct of 10% is examined here, which corresponds to eight RBCs positioned inside the 45μm arteriole section. The platelet count in a healthy individual is between 150,000 and 450,000 per μL [123] which is equivalent to 1~3 platelets in the simulation volume. Computationally, we consider a single platelet, corresponding to a concentration of approximately 150,000 cells per μL (with consideration of volume exclusion of the thrombus). Larger vascular sizes, higher Hct values and platelet count may be employed in future studies at a higher

computational cost. The initial configuration of the RBCs and platelet were predetermined manually, and simulations were run until they randomized and reached a statistically stationary state (data not shown). The platelet was placed at the peripheral region because of the well-known platelet margination effect [15,109,124]. The mean flow velocity was set at a velocity of 1128 μm/s, which is within the physiological range in arterioles of this size [125]. The resulting Reynolds number is about 5.65×10^{-3}, which is well within the range of Stokes flow calculations.

A 3D bump was centered at the midpoint of the vessel to represent an existing thrombus and partial stenosis. Its specific shape is

$$y = H - \frac{w}{1.9^{\left(\frac{(z-22.5)^2}{a}+\frac{x^2}{b}\right)}}$$

which is based on *in vivo* fluorescent microscopic images from the mouse experiments of this study. The *x*-*z* section of the thrombus is an ellipse and the *x*-*y* section of the thrombus appears Gaussian in shape. By varying the parameters *a*, *b*, *w* and *H* one can obtain different thrombus shapes and percentages of stenosis (calculated as the *x*-*y* cross sectional area blockage).

3.2.4 In Vivo Thrombus Formation

The VWF ^{R1326H} mouse strain was used as described in previous studies [112]. The administration of anesthesia, fluorescent labeling, and administration of human platelets and surgical preparation of the cremaster muscle in mice have been previous described [60,126]. Injury to the vessel wall of arterioles (~40–65 μm diameter) was performed using a pulsed nitrogen dye laser (440 nm, Photonic Instruments) applied through a 20×

water-immersion Olympus objective (LUMPlanFl, 0.5 NA) of a Zeiss Axiotech vario microscope.

Human platelet–vessel wall interactions were visualized by fluorescence microscopy using a system equipped with a Yokogawa CSU-22 spinning disk confocal scanner, iXON EM camera, and 488-nm and 561-nm laser lines to detect BCECF-labeled platelets (Revolution XD, Andor Technology). The extent of thrombus formation was assessed immediately after laser-induced injuries for a total observation period of 10 min. Images were captured at an average of 66.7 fps with 10 ms exposure time at an appropriate *x*-*z* plane. Data from three mice yielded ~4000 frames of micrograph images to analyze in this study.

3.2.5 Image Processing and Analysis

The *in vivo* image stacks were processed using ImageJ. All the data visualization and analysis was carried out using Microsoft Excel and in-house developed Matlab codes.

3.3 Results

First, we studied the blood flow profile in thrombotic vessels and the disturbed flow around the existing thrombus. The near-wall velocity field indicates potential platelet-wall interactions. A stability analysis on the hydrodynamics caused by RBCs was also performed. The stenotic flow velocity was compared to *in vivo* data and good agreement was found. Platelet trajectories when passing by the thrombus with and without RBCs

were then examined. The platelet-thrombus and platelet-RBC interaction patterns were studied to evaluate the significance of RBC-enhanced platelet-thrombus interactions.

3.3.1 Simulation of Flow Disturbance Caused By A Thrombus

The flow profile in the vessel section unit is displayed in Figure 1. The biconcave-shaped RBCs deform into cap-like structures in the cylindrical vessel lumen, in agreement with in vitro observations [127]. The velocity field is shown in Figure 3.1B. Along both ends of the *z*-axis, the velocity field shows an approximately parabolic shape with *z*-axis symmetry. The effect of the thrombus is localized, showing that the streamwise periodic length of the vessels is sufficiently large to avoid any significant artifacts associated with the non-*z*-axis symmetric periodic boundary conditions. When the flow reaches the thrombus (z = 15 to 30 μm), the entire flow is displaced in the *y*-direction. Figure 1C shows the disturbance of the flow caused by the thrombus. It was generated by subtracting the non-disturbed flow (flow inside a smooth cylindrical vessel without a thrombus) from the flow shown in Figure 3.1B. Note that the length scale of the blue cones is expanded in Figure 3.1C compared to Figure 3.1B to display the velocity disturbance clearly. It can be readily seen that the velocity disturbance at z = 5 μm is very small, verifying that the disturbance of the thrombus one period upstream has little impact on the target section. Indeed, it is known from the Green's function of Stokes flow that the velocity disturbance from a point force decays at a rate of $1/r$. The existence of the thrombus slows down the overall flow, dragging the near-thrombus flow by the no-slip boundary condition while accelerating the flow at the back side (locations with smaller *y* coordinate, as opposed to the thrombus side), showing how the fluid accelerates

when passing through a narrowing blood vessel. It is worth noting that due to the existence of RBCs, the velocity profile does not display a smooth outline. In the model, the higher viscosity of the RBC cytosol as well as the elastic cell membrane [76] cause the velocity field to deviate from an smooth curve.

3.3.2 Simulation of Flow Profile with Various Thrombus Shapes

The near-wall velocity is shown in Figure 3.2. The velocity profile at the near-thrombus region (Figure 3.2C-E, I-K) and on the opposite side of the vessel (Figure 3.2F-H, L-N) was analyzed for different thrombus shapes. Since all of the velocities in Figure 3.2 are evaluated at the same distance from the vessel wall, this provides an estimate of the wall shear stress $\tau \approx \mu \frac{v}{\Delta y}$ (with Δy being the same in all cases). As a result, the conclusions drawn for flow velocity in this section can be applied to shear stress as well. It was found that, at most of the locations along the central line of the thrombus, the near-wall velocity exhibited a drop directly before reaching and after passing the thrombus (Figure 3.2C-E, I-K), which matches previous observations [128]. Such stagnation zones are not found at the back side of the vessel, where the velocity changes at z = 22.5 μm are also smaller by three-fold (Figure 3.2F-H, L-N). It is interesting to note that not all azimuthal positions (as one color indicate one azimuth in Figure 3.2) experience a velocity increase when approaching the thrombus. At specific azimuths (Figure 3.2C, D, I-K orange line), the velocity in fact decreases while approaching the thrombus. This is most likely because at the locations where the thrombus surface and cylindrical vessel wall surface intersect and form a near 90º angle, the no-slip boundary conditions (imposed by the thrombus surface as well as the vessel surface) strongly limit the flow velocity in these valley regions. For

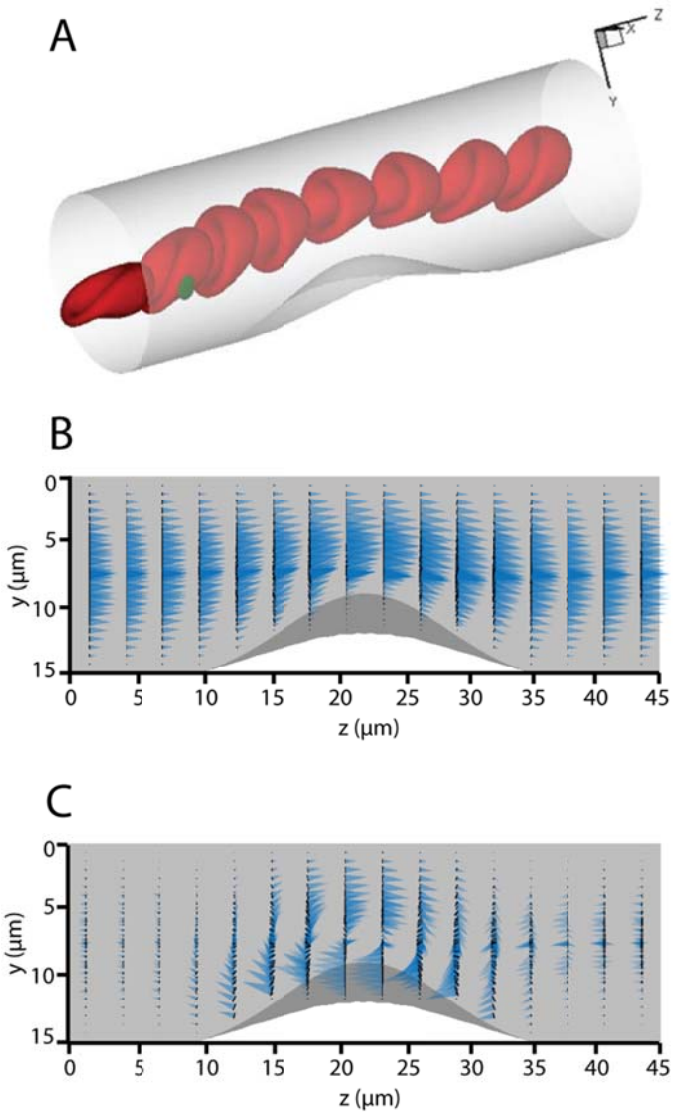

Figure 3.1 The 3D visualization of the simulation model and velocity profile inside the vessel lumen. (A) A representative sketch with one periodic boundary unit displayed. The red particles show the natural shape of biconcave-shaped RBCs under tubular flow. The green cell represents a platelet and the semi-transparent bump on the vessel wall represents the thrombus. (B) The velocity profile inside the vessel lumen is shown. Each cone represents the velocity vector at that specific location. (C) Deviation velocity field surrounding the thrombus.

different thrombus shapes, there is no significant change in the character of the flow (Figure 3.2C-H). Extension of the thrombus along the *z*-axis causes a similar expansion pattern in the velocity profile (Figure 3.2C, F), while extension of the thrombus along the *x*-axis reduces the "valley" region discussed above (Figure 3.2E). Without cells in the system, the near wall velocity shows surface symmetry at the surface z = 22.5 μm (Figure 3.2C-E). Such symmetry is not present for cellular blood flow (Figure 3.2I-N). It was also found that the peak near-wall velocity decreases by about 15% when Hct=10% (Figure 3.2D, I-K), suggesting that the existence of RBCs caused blood rheology change (e.g. increased viscosity). In the presence of RBCs and platelets, velocity fluctuations as a function of time are observed (Figure 3.2I-N). These fluctuations can be as large as 10% of the average. The velocities near the center of the thrombus exhibit a similar "zigzag" change (Figure 3.2L-N) at different time points. This may be due to the similar configuration of the surface boundary conditions when cap-shaped RBCs pass by the thrombus, with the caps oriented downstream. Taken together, these data indicate that blood cells, particularly deformable RBCs, may not be neglected when constructing thrombosis models.

3.3.3 Simulation of Flow Velocity with Various Degrees of Stenosis and its Comparison to Published Patient Data

To confirm the hydrodynamics of our model, the dimensionless peak velocity (DPV) based on different degrees of area stenosis was calculated and compared to previously published patient data (Figure 3.3). The DPV is calculated by dividing the maximum *z*-

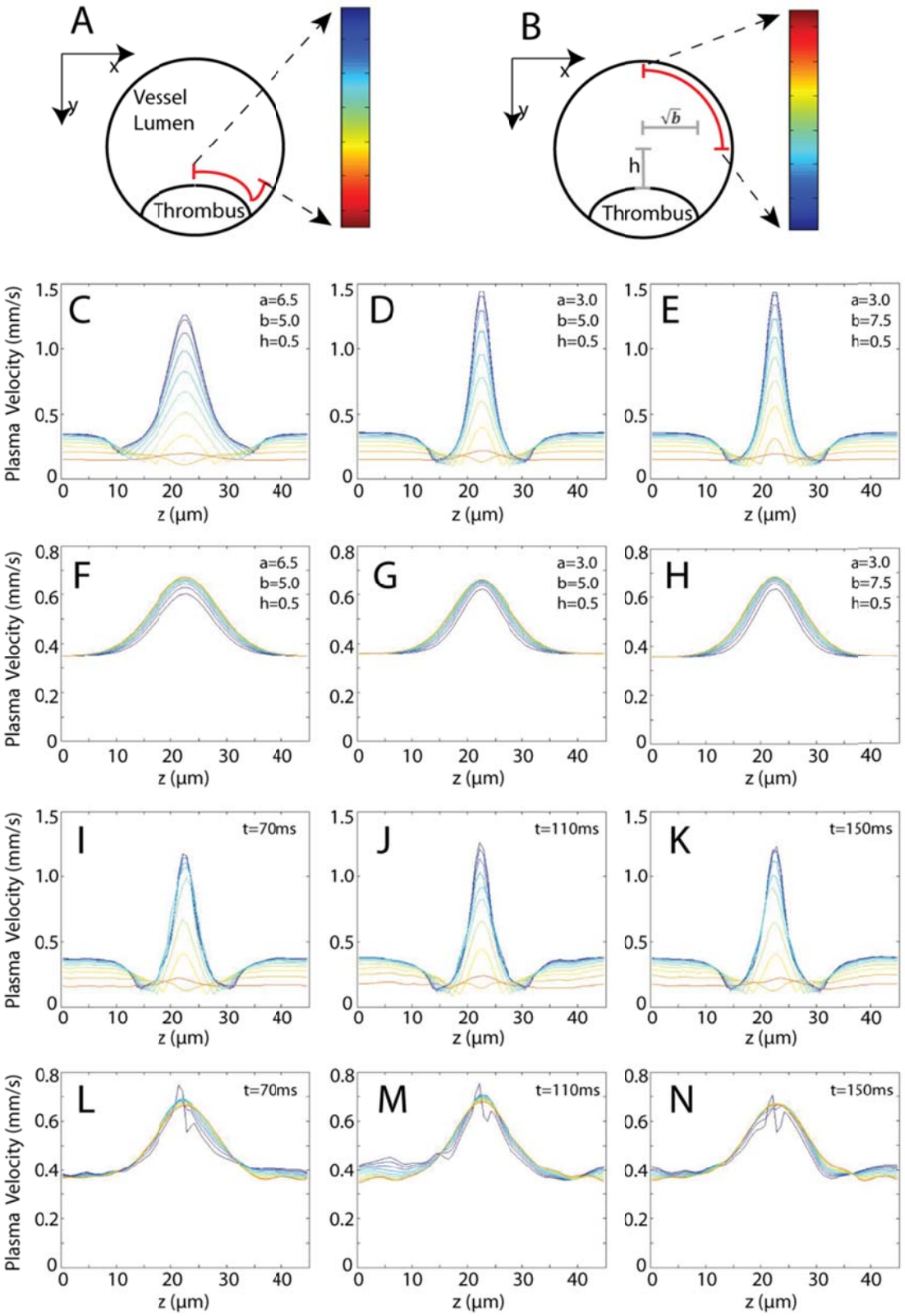
A
x
y
Vessel
Lumen
Thrombus
B
x
y
√b
h
Thrombus
C
a=6.5
b=5.0
h=0.5
D
a=3.0
b=5.0
h=0.5
E
a=3.0
b=7.5
h=0.5
F
a=6.5
b=5.0
h=0.5
G
a=3.0
b=5.0
h=0.5
H
a=3.0
b=7.5
h=0.5
I
t=70ms
J
t=110ms
K
t=150ms
L
t=70ms
M
t=110ms
N
t=150ms
Plasma Velocity (mm/s)
z (μm)

Figure 3.2 Near-wall velocity profiles. (A) Analysis geometry for C–E and I–K. The color bar identifies the series of near-thrombus velocity profiles in C–E and I–K along the curve (y-distance 0.5 μm from the wall). (B) Analysis geometry for F–H and L–N, with the color as in (A) but with 0.5 μm distance from the wall. (C–H) The velocity profiles with three different thrombus shapes are shown (Hct=0). (I–N) The velocity profiles at the same conditions as D and G, with Hct=10% are shown. The thrombus geometry parameters a, b, $h = H\text{-}w$ are defined in Eq. 25 and the resulted degree of stenosis are 36%, 36% and 39% separately.

axis velocity in the vessel by the maximum non-stenotic velocity. Several factors suggest the use of the DPV metric: (i), the consensus clinical indicator of stenotic blood velocity is the peak systolic velocity (PSV) [129], where the "peak" indicates the highest velocity which is usually found at the narrowest stenotic region (z = 22.5 μm in our cases, based on the results in Figure 3.2); (ii), non-dimensionalization enables direct comparisons. We found a super-linear relationship between DPV and the percentage area stenosis for all four thrombus shape settings (Figure 3.3A). The larger the percentage area stenosis, the greater the impact of thrombus shape on DPV, while for less-severe stenosis (<35%), the DPV do not vary much among different thrombus shapes (Figure 3.3A). Our simulation results agree with patient sample data where the blood flow velocity shows a super-linear relationship between DPV and percentage area stenosis (Figure 3.3B).

3.3.4 Simulation of Platelet Trajectories and its Comparison to New Mouse Data

Platelet trajectories both in simulations and the *in vivo* mouse thrombus model (Figure 3.4A, B) were analyzed. *In vivo* platelet trajectory plot (Figure 3.4B) was reproduced by manually discretizing platelet trajectories over 500 frames. One way to quantitatively evaluate the hydrodynamic impact of the thrombus on platelet motion is to examine how platelet trajectories converge at the stenosis relative to the thrombus shape. We ran a series of simulations with platelets released at locations $y = 0.5(22.5 - h)$ and the x-coordinates varied for each thrombus setting. Considering the limitations of fluorescent microscopy regarding the depth of field, simulations resulting in platelet trajectories fluctuating more than 2 μm in the y-direction were excluded. The trajectory densities were recorded according to their relative z-axis positions (Figure 3.4C), where the

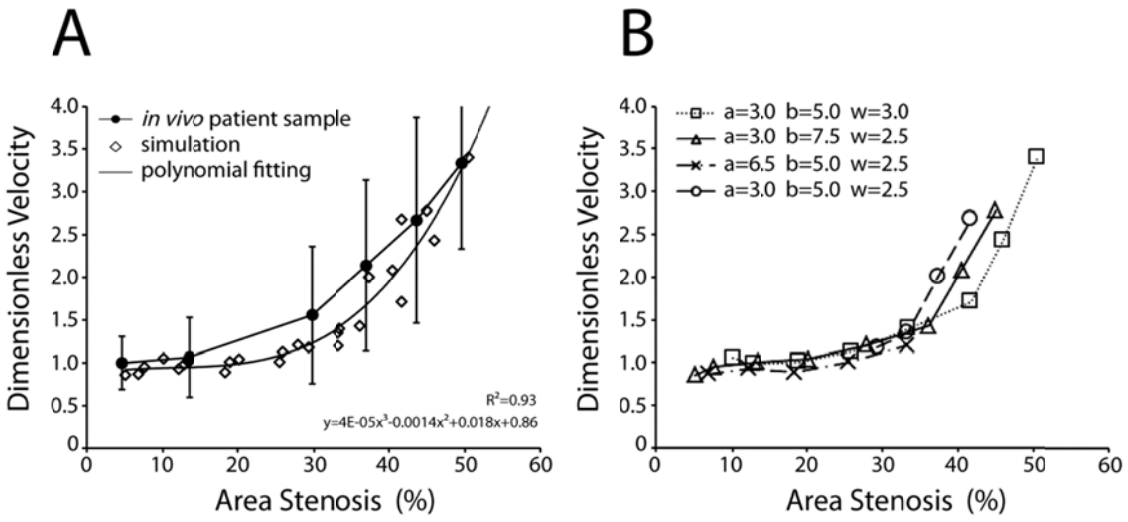

Figure 3.3 Peak blood velocity for a range of simulation settings and their comparison to *in vivo* data. (A) The dimensionless peak blood velocities (DPV) from four different thrombus settings were evaluated. Note: for each thrombus setting, the parameters a, b and w are fixed, but H was varied (Eq. 25) which resulted in different degrees of area stenosis. The percentage area stenosis was evaluated by the percent area blockage of the thrombus at z = 22.5 μm. (B) All the data points in (A) are plotted, fitted by polynomial fitting and compared to the *in vivo* carotid artery stenosis-blood velocity data [129]. (The *in vivo* data was non-dimensionalized with the *in vivo* average non-stenotic blood velocity of 75 cm/s.)

relative z is quantified by the z-axis position minus 22.5 μm and then scaled by the length of the major axis of the 3D thrombus projection (the projection is an ellipse as described) on the x-z plane. The trajectory density at each $z = Z$' was calculated as: (i), projected all the trajectories onto the x-z plane; (ii), scaling of the total number of trajectories passing by the line $z = Z$' by their largest x-coordinates separation (max(x)-min(x)); (iii), renormalization with the highest density. It is clearly seen that the extensions in both z and x direction (a = 3, b = 5) of the thrombus cause the platelet trajectories to converge and diverge at closer distances to the thrombus. It was also determined that the existence of RBCs drive platelets laterally thus further condensing the platelet trajectory when passing by the thrombus, compared to the less pronounced convergence and divergence in simulations without RBCs (Figure 3.4C). The reversibility of platelet trajectories, one of the key characteristics of Stokes flow, was checked. It was found that when RBCs are present, there is up to a 10% difference in the x-coordinates for the platelet positioned at the same distance upstream and downstream of the thrombus center along its trajectory (Figure 3.4D). On the other hand, there is only ~1% difference in the absence of RBCs which is mostly likely the result of numerical error. In other words, platelet trajectories do not reconverge downstream of the thrombus as rapidly as they diverge before reaching the thrombus. Two-sample unpaired t-tests indicate that this difference is significant ($P < 0.05$) for most of the conditions (Figure 3.4D).

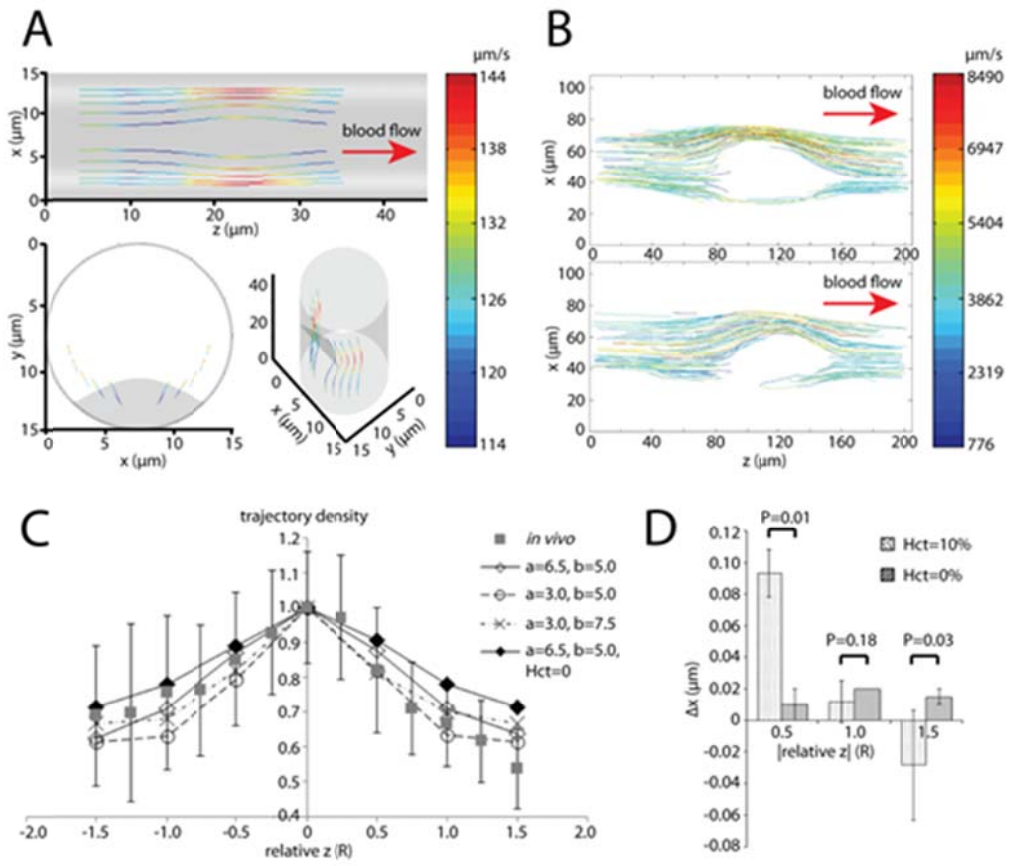

Figure 3.4 Platelet trajectories generated in simulations and compared with *in vivo* data. (A) A representative platelet trajectory collection generated by a series of simulations under a specific thrombus shape setting (a = 7.5, b = 6, h = 1.2, degree of stenosis = 23%) as viewed from three camera angles, with color indicating the local platelet velocity. (B) Two representative *in vivo* platelet trajectory collections are shown and color coded to represent the local platelet velocity. (C) Quantitative comparison between simulation and *in vivo* data of how platelet trajectories converge when passing by a thrombus and then diverge when leaving the thrombus. (D) Quantification of the x-coordinates difference of the platelet positions along a trajectory the same distance upstream and downstream the thrombus center (the absolute value of relative z coordinate) from the same series of simulations in (C). Two-sample unpaired t-test was performed with P-values given.

3.3.5 Simulation Shows Direct Evidence That RBCs Enhance Platelet Deposition

To determine how RBCs affect platelet-thrombus interactions, the platelet deposition potential map (Figure 3.5A, B) generated by a series of simulation experiments with platelets starting at different peripheral positions inside the vessel was plotted. The platelet deposition potential is defined here as the shortest separation distance between the following platelet and the thrombus surface, with smaller distances corresponding to stronger potentials. A global enhancement of the platelet deposition potential on the entire thrombus surface is readily seen. The closest distance is about 0.17 μm, within the maximum reactive distance (~260nm) based on the approximation of the length of the integrin $\alpha_{IIb}\beta_3$-vWF-$\alpha_{IIb}\beta_3$ trimolecular bond [54,103]. The direct observation of RBC-enhanced platelet-thrombus interaction is depicted in Figure 3.5C. When the platelet follows the motion of a modified Jeffery orbit near the vessel wall, it rotates along the *x*-axis and transitions from a parallel orientation to a perpendicular orientation, then back to the parrallel orientation again [34]. During the perpendicular orientation, the platelet extends its reach along the *y*-axis and occupies the excluded volume generated by the RBCs. As a result, the platelet is pushed towards the thrombus thus enhancing its deposition potential (Figure 3.5C).

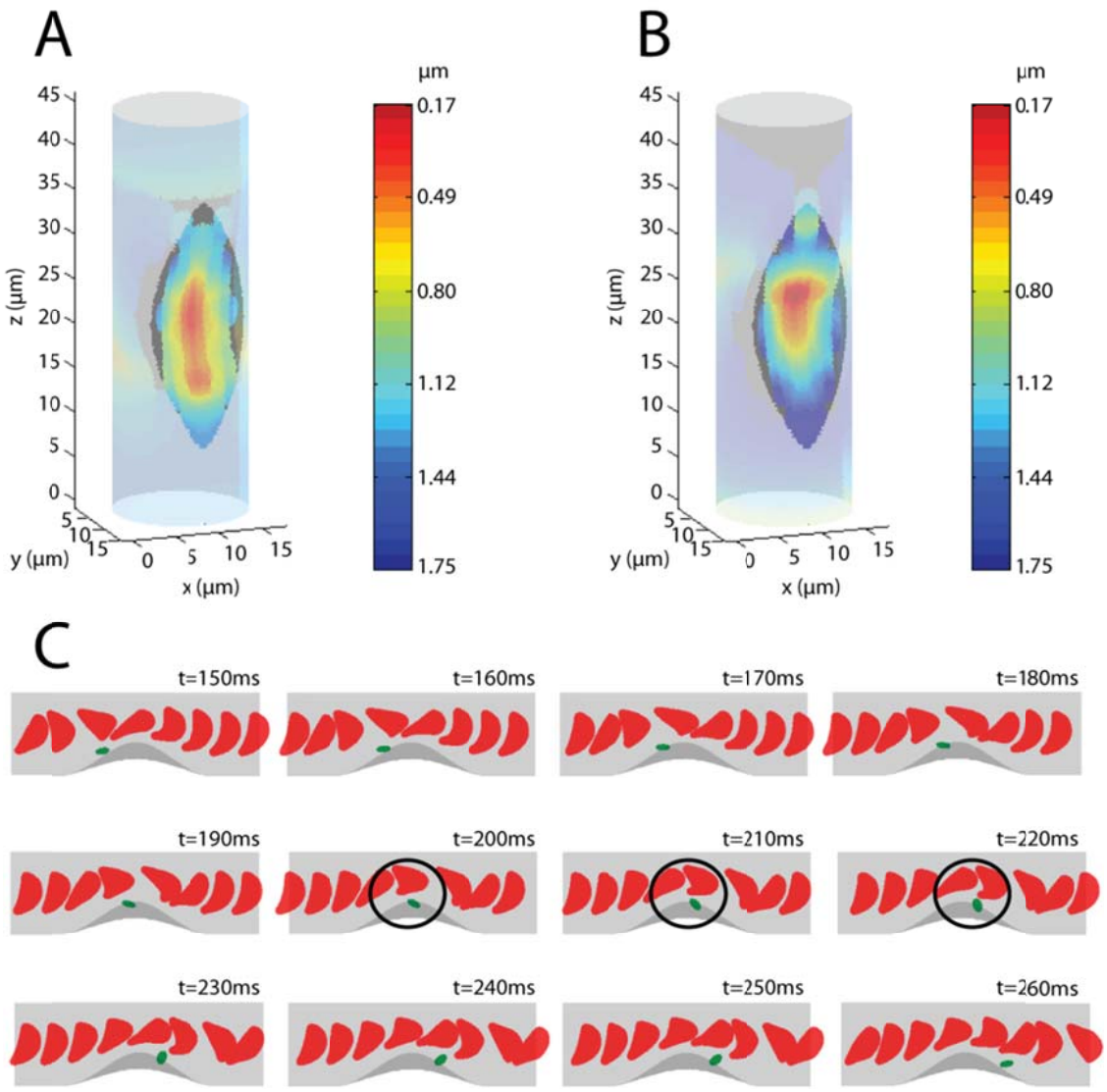

Figure 3.5 The platelet deposition potential is enhanced by hydrodynamic interactions with RBCs (thrombus settings: a = 7.5, b = 6, h = 1.2, degree of stenosis = 23%). (A) The platelet deposition potential map generated by a series of simulations with Hct = 10%. The color on the vessel wall surface indicates the distance between a flowing platelet and the vessel wall. (B) The platelet deposition potential map with the same settings as in (A) except Hct = 0. (C) Sequential frames of a representative simulation. The black circles demark direct evidence of RBCs-enhanced platelet-thrombus interaction.

3.3.6 Simulation of Platelets and Their Interaction with RBCs and Vessel Wall

Quantitative analysis of RBCs-influenced platelet-thrombus interactions was carried out for different initial positions of the platelet (Figure 3.6). Some general trends are: (i) the distance between the platelet and RBCs exhibits "wave-like" oscillations, with each peak corresponding to the passing of an RBC; (ii) the disk-shaped platelet spends most of its time in a parallel orientation and experiences a fast flipping motion every 20~25 μm; (iii) such flipping motion is prolonged when the initial position of the platelet has a larger azimuthal angle (x-coordinate deviation from 7.5 μm). The third trend could have important implications during the development of hemostasis, since the longer duration of perpendicular orientation extends the time window of platelet-thrombus hydrodynamic interaction at the side of the thrombus. Such extension enhances the probability of successful recruitment of following platelets onto the side of the thrombus, compensating for the reduced margination effect of RBCs at larger azimuthal angles (the platelet-RBCs distance increases with increasing azimuthal angle of the initial position of the platelet, Figure 3.6A~D). It was also found that the closest distance between the thrombus and platelet throughout simulations is concurrent with the shortest separation distance between the platelet and RBCs (Figure 3.6A).

3.4 Discussion

This study evaluates the hydrodynamic interaction between deformable RBCs, ellipsoidal platelets and a model thrombus shape under physiological flow inside a cylindrical arteriole. The flow profile inside the vessel was found to have stagnation zones directly

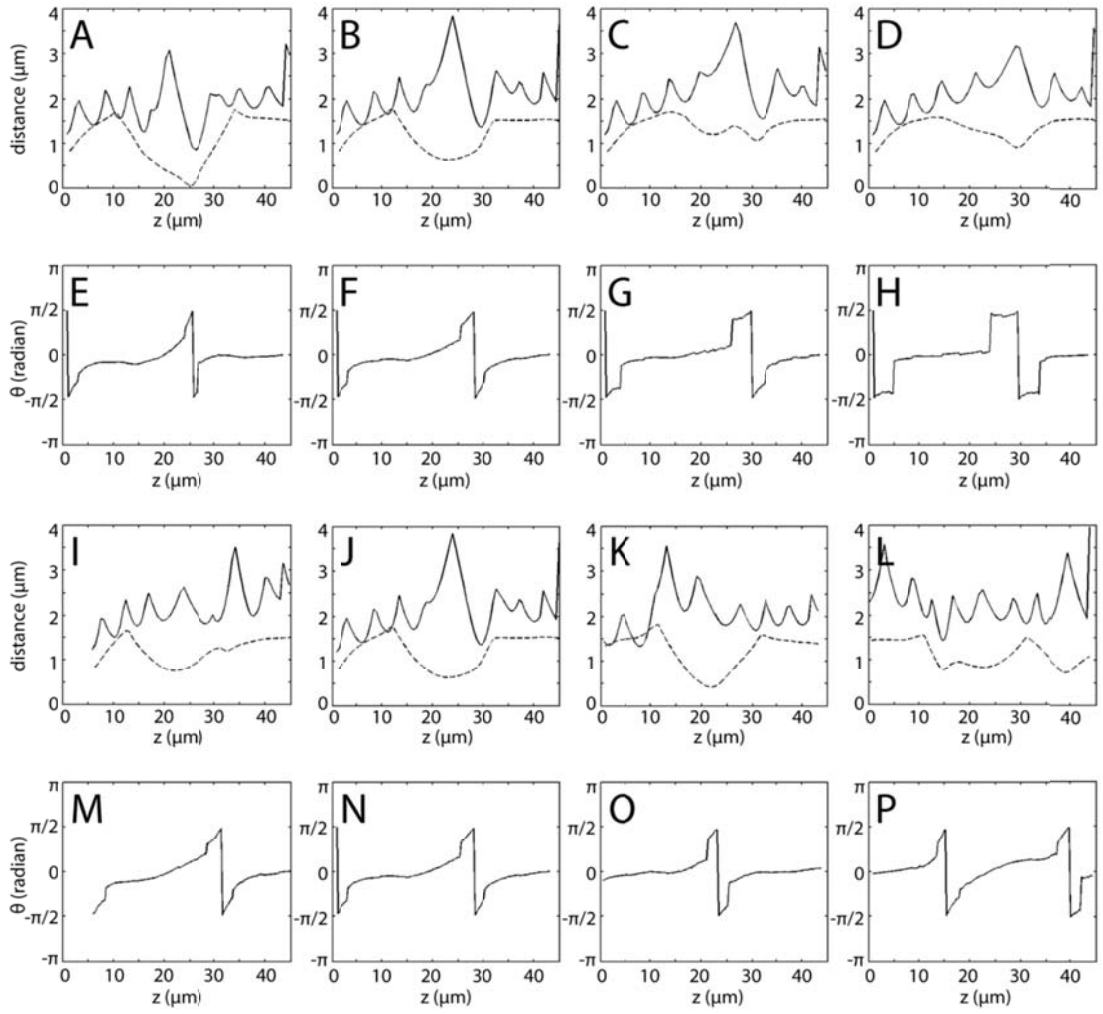

Figure 3.6 The hydrodynamic interaction between platelets, thrombus and RBCs and the configuration of the flowing platelet is shown. (A)-(D), (I)-(L) Solid lines display the shortest distance between the platelet and RBCs during platelet advection. Dashed lines display the shortest distance between the platelet and vessel wall surface. (E)-(H), (M)-(P) The rotational angle of the platelet about the *x*-axis is shown during platelet advection. (A)(E), (B)(F), (C)(G), (D)(H) are pairwise data generated from four simulations with platelets starting at $z = 0$ μm and the same distance to the vessel wall, but different

azimuthal angles. (I)(M), (J)(N), (K)(O), (L)(P) are pairwise data generated from four simulations with the platelets starting at the same azimuthal angle and same distance to the vessel wall, but different *z*-coordinates (5 μm, 0 μm, -5 μm, -10 μm separately). Note: (J)(N) are duplicates of (B)(F).

upstream and downstream of the thrombus at most azimuth angles. In previous studies, stagnation zones were identified by *in vivo* experiments [128]. A new mechanism of

platelet aggregation has been described by Nesbitt et al. and is considered to be mainly shear stress gradient dependent [92]. In their study, the authors found that platelets form aggregates when encountering a drop in shear rate. However, they did not explore the fact that platelets also experience a drop in shear rate at the opposite side of the thrombus and no aggregate is formed. Based on the present results, we argue that the non-axisymmetric placement of a bump-shaped thrombus creates a hydrodynamic environment which causes the magnitude of shear-gradient that platelets experience to differ by 3~4 fold at different azimuth positions (Figure 3.2). In other words, platelets experience a much smaller shear gradient at the opposite side of the thrombus, potentially explaining this phenomenon.

While the majority of the available blood flow velocity data comes from large human arteries, there is a lack of published information for the full range of percentage stenosis in vessels of smaller sizes (arterioles, venules and capillaries). We choose human carotid artery stenosis data [129] for comparison in Figure 3.3, recognizing the blood rheology difference (e.g., Hct) between large arteries (~5 mm in diameter for carotid artery in human adults) and small arterioles (~40 μm). Any comparison is limited to examining qualitative trends, due to the difference in length scales between the clinical and computational systems. Another point to note is the conversion of the *in vivo* data from diameter stenosis provided by Grant et al. to area of stenosis. It is known that the

thrombus does not develop uniformly along the peripheral of the vessel wall to form a perfect ring shape (which would translate to a quadratic relationship between diameter and area), and does not develop in a "flow-chamber" character (which would translate linearly between diameter and area). Thus, the relation between diameter stenosis and area stenosis must be super-linear but not exceed a power of two. Indeed, a recent study determined with CT angiography that the correlation of carotid stenosis diameter with cross-sectional areas is super-linear but did not exceed a square dependence [130]. In Figure 3.3B, we thus assume a power of 1.5 and introduce an additional adjustment factor of 0.63 to compare the *in vivo* patient sample with the present simulation results. The factor 0.63 may represent the result of blood rheology differences due to the two orders of magnitude length scale difference between carotid arteries and a 15 μm diameter arteriole.

Due to the complex *in vivo* vessel/thrombus geometry, as well as the larger vessel diameters (45~60 μm) of mouse cremaster muscle (15 μm in our simulation), the convergence of platelet trajectories fluctuates in individual *in vivo* experiments in Figure 3.4. However, it shows a similar trend with comparable ranges. The mechanics of deformable RBCs cause the flow inside the vessel tube to deviate from the typical characteristics of Stokes flow. This can be understood by simple reasoning: Stokes flow does not require time to develop and the disturbance will immediately cause steady flow changes throughout the entire volume; however, RBCs do require time to establish their equilibrium 'cap-shaped' geometry following the start of flow.

The irreversible motion depicted in Figure 3.4D is in accordance with the results of Figure 3.6 (A)(B)(I)~(K), where one finds that platelets approach the thrombus faster and leave the thrombus slower. This may reduce the probability of the thrombus to grow in the direction of flow, increasing the effective wound coverage and reducing the size of the thrombus to result in a reduced risk of a blood clot. This non-Stokesian behavior is introduced into the system by the geometric nonlinearity and mechanical properties of the RBCs, with the elasticity of the RBCs adding an additional time scale.

It is well understood that RBCs contribute to the rheology of blood by increasing the viscosity and causing margination of platelets and leukocytes. However, the hydrodynamic interaction between platelets and a thrombus in the presence of RBCs has not been previously studied in detail. From Figure 3.6, one may conclude that there are three major sources for potential platelet deposition onto the thrombus, i.e., when the platelet comes close enough to the thrombus surface for molecular adhesion such as that mediated by $\alpha_{IIb}\beta_3$-vWF-$\alpha_{IIb}\beta_3$ bond formation. The first source of such platelet deposition potential is the geometry of the thrombus itself which reduces the platelet-thrombus distance in the thrombus region (z coordinates ranging from 15 to 30 μm) in all simulations performed. The second source is the platelet flipping motion, where the platelet rotational angle jumps (from $\pi/2$ to $-\pi/2$) are always concomitant with a dip in the platelet-thrombus distance (Figure 3.6), indicating the physiological importance of the ellipsoid shape of platelets. The third is the interaction between platelets and RBCs. These three sources of platelet deposition potential identified here not only reinforce the importance of their ellipsoid shape to normal platelet function, but also show the direct

enhancement of platelet-thrombus interaction through platelet-RBCs interactions. In the future, it would be interesting to investigate the direct interaction between RBCs and the thrombus as well as any mechanical effect of RBCs on thrombus fragmentation. Previous studies show that RBCs can be engineered to suppress thrombosis by coupling them with anti-thrombotic agents [131], suggesting frequent physical contact between RBCs and the developing thrombus.

Ultrasound Doppler is currently the most common blood velocity measurement method and is widely accepted in clinical applications. Doctors judge patients' degree of stenosis based on elevated blood flow velocity. While much faster, convenient and non-invasive compared to angiography, Doppler has its own limitation: accuracy. The major source of inaccuracy comes from the broad assumption that the direction of blood flow is parallel to the axis of the blood vessel lumen, which can cause miscalculation of the velocity magnitude [132]. Another limitation is that the Doppler data does not easily facilitate reconstruction of 3D flow fields and vessel conditions. Several improvements have been made to either precisely position the sample volume [133] or use multiple transducers to measure the velocity vector [134], but these improvements cannot fully eliminate uncertainty. Computational studies can better reveal the flow characteristics inside the complex geometry of the vessel wall thus helping clinicians to better link the Doppler data with patient symptoms. Comparisons such as that in Figure 3.3 serve as an example: from given velocity data, clinicians may assess the range of potential thrombus shape and position. This also suggests that simulation studies can potentially regain the lost dimension in clinical measurement (2D to 3D).

In conclusion, we have established a hydrodynamic model which is able to reveal the hydrodynamic interaction between blood cells and the vessel wall in 3D. We successfully characterized the hydrodynamic environment for different thrombus shapes and degree of stenosis and the results agree with *in vivo* results. Future applications of the present model will be focused on adhesion of various types of receptor-ligand pairs. We have already incorporated the kinetics of GPIbα–vWF-A1 into our Platelet Adhesion Dynamics model (PAD) [14]. We also successfully recover the translocational motion of platelets on injured vessel walls [102]. It will be interesting to examine how platelets tether and translocate under the interaction of surrounding RBCs and thrombus in a cylindrical vessel.

CHAPTER 4: ANALYSIS OF EARLY THROMBUS DYNAMICS IN A HUMANIZED MOUSE LASER INJURY

Platelet aggregation and thrombus formation at the site of injury is a dynamic process that involves the continuous addition of new platelets as well as thrombus rupture. In the early stages of hemostasis (within minutes after vessel injury) this process can be visualized by transfusing fluorescently labeled human platelets and observing their deposition and detachment. These two counterbalancing events help the developing thrombus reach a steady-state morphology, where it is large enough to cover the injured vessel surface but not too large to form a severe thrombotic occlusion. In this study, the spatial and temporal aspects of early stage thrombus dynamics which result from laser-induced injury on arterioles of cremaster muscle in the humanized mouse were visualized using fluorescent microscopy. It was found that rolling platelets show preference for the upstream region while tethering/detaching platelets were primarily found downstream. It was also determined that the platelet deposition rate is relatively steady, whereas the effective thrombus coverage area does not increase at a constant rate. By introducing a new method to graphically represent the real-time *in vivo* physiological shear stress environment, we conclude that the thrombus continuously changes shape by regional growth and decay, and neither dominates in the high shear stress region.

4.1 Introduction

During the early stages of hemostasis, a thrombus mainly consists of adherent platelets and grows in size through the active recruitment of additional flowing platelets via αIIbβ3-fibrinogen-αIIbβ3 or αIIbβ3- von Willebrand factor (VWF)-αIIbβ3 bonds [54]. The formation of these two types of trimolecular bonds requires the activation of integrin αIIbβ3 on the platelet surface. Such integrin activation is usually a result of platelet activation followed by either adhesion to immobilized VWF and collagen, or by signaling through soluble platelet agonists such as ADP and thrombin [135]. Under extreme hydrodynamic conditions, at shear rates > 10000 s^{-1}, platelets can form aggregates independently of integrin αIIbβ3 or platelet activation and are believed to be mediated through VWF–GPIbα interaction [91].

Surface-recruited platelets do not always end their journey by forming aggregates at sites of vascular injury. Platelet tethering, detachment and translocation (rolling) events are frequently observed and readily incorporated into both experimental and computational platelet aggregation models [73,108,136,137]. Although platelet rolling on activated, intact endothelium depends on endothelial P-selectin [138], tethering and translocation are associated with interactions between matrix-bound VWF and GPIbα [3,60]. Specifically, the binding kinetics of the VWF–GPIbα bond was determined by *in vitro* platelet tethering and translocation experiments on VWF-coated flow chambers [60,85]. Both tethering and translocating platelets are temporary residents on the injured vessel wall and rejoin the blood circulation after a relatively short period of time (several seconds).

Even adhesive platelets that successfully formed aggregates at the injury site may be released back to the bloodstream from platelet-rich clots. These aggregates that form in regions such as the post-stenotic with ideal hydrodynamic conditions for thrombus growth are usually unstable and lead to intermittent embolization [139,140]. The peripheral regions of the developing thrombus may also be prone to fragmentation given that high shear stress decreases the lifetime of adhesive bonds on platelets [141]. Fragmented emboli travel in the bloodstream and may re-lodge in small vessels or capillaries when the diameter of the vessel is too small for the emboli to pass through. Eventually, they are eliminated by blood flow (washout) or extravasation for vascular recanalization [142]. Impaired clearance of emboli may lead to organ hypoperfusion, embolism and ischemic stroke [143].

The thrombus undergoes dynamic growth and fragmentation for hours after initial vessel injury, but these processes may persist for days or even longer [128]. Such a dynamic balance is a consequence of the combination of rheological and chemical (e.g., soluble agonists) mechanisms [128]. While soluble agonists exclusively activate platelets and stabilize thrombus growth, rheological mechanisms may result in two opposing effects. On the one hand, the complex geometry of the wound generates a pathological high shear stress locally. Such a high-shear environment promotes recruitment of discoid platelets by forming VWF–GPIbα bonds, which require a minimal threshold shear environment to establish [60]. On the other hand, high shear stress may facilitate thrombus fragmentation due to mechanical failure. Other rheological mechanisms that

play a role in thrombus dynamics may include RBC mediated platelet margination and adhesion [144] as well as finite platelet size and shape [14,145].

Application of microfluidic devices specifically designed to study the thrombus formation *in vitro* can be dated back to the 1970's [146] and are still making its progress today [147]. Meanwhile, *in vivo* models start to show their significance. For example, Newman et al. infused human platelets into a mouse circulation system to study platelet function, survival and the efficacy of antiplatelet therapeutics [148]. However, because of the structural differences between human and murine sVWF and GPIbα molecules, human platelets cannot form clots on injured murine vessel surfaces. A novel platform has been developed to address this issue by enabling the *in vivo* assessment of human platelet mediated thrombus formation in mice [112]. This was accomplished by genetically modifying the A1 domain of murine VWF (VWF-A1) so that it interacts with human but not mouse GPIbα. Consequently, the VWF R1326H mice have a bleeding phenotype that can be corrected by the administration of human platelets.

While *in vivo* thrombus growth and platelet aggregation have been studied for more than a decade [149,150], *in vivo* flow field reconstruction methods still require refinement to be applicable to different individuals. A typical example is to use high resolution magnetic resonance imaging (MRI) to define the static 3D geometry of the target blood vessel *in vivo*. The geometry data is analyzed with computational fluid dynamics (CFD) software to calculate the local hydrodynamic environment [23]. However, the method does not capture the dynamically changing hemostatic environment in real-time. In this

paper, we offer a cell trajectory and outline based method to capture the real-time deformation of the thrombus and the changing hydrodynamic calculation.

4.2 Materials and Methods

4.2.1. In vivo fluorescence microscopy

The VWF^{R1326H} mouse strain was used as described in previous studies [23]. The administration of anesthesia, fluorescent labeling, human platelets as well as surgical preparation of the cremaster muscle in mice have been previously described [60,126]. Injury to the vessel wall of arterioles (~80-μm diameter) was achieved by using a pulsed nitrogen dye laser (440 nm, Photonic Instruments) applied through a 20× water-immersion Olympus objective (LUMPlanFl, 0.5 NA) of a Zeiss Axiotech vario microscope. The resulting wound was approximately 40 μm × 40 μm.

Human platelet–vessel wall interactions were visualized by fluorescence microscopy using a system equipped with a Yokogawa CSU-22 spinning disk confocal scanner, iXON EM camera, and 488-nm and 561-nm laser lines to detect BCECF-labeled platelets (Revolution XD, Andor Technology). To capture early events of hemostasis, the extent of thrombus formation was assessed ~5 s after laser-induced injury. Images were recorded at an average of 66.7 fps with 10 ms exposure time. The focal plane was adjusted such that it was parallel to the part of vessel surface in which the injury was introduced. Data from six mice yielded a total of ~15,000 micrograph image frames to be analyzed in this study. Since the images are two-dimensional (2D) projections, all the physical components are analyzed in 2D, including positions of captured platelets, trajectories of

the flowing platelets, the velocity fields and the wall shear stress.

4.2.2. Image processing and calculations

The locations of adherent, translocating and tethering platelets were recorded manually in Cartesian coordinates using ImageJ (Figure 4.1A). In each experiment, the absolute positions were based on the boundaries of image frames and the positions relative to the center of the thrombus were calculated as follows:

1. Calculate the center of injury by averaging the locations of adherent platelets.
2. Re-center all platelets by the approximate center of injury.
3. Convert Cartesian coordinates to polar coordinates.
4. In each experimental set normalize the radii by the 50% quantile of the radii of all adherent platelets to enable parallel comparison between different sets to be made.

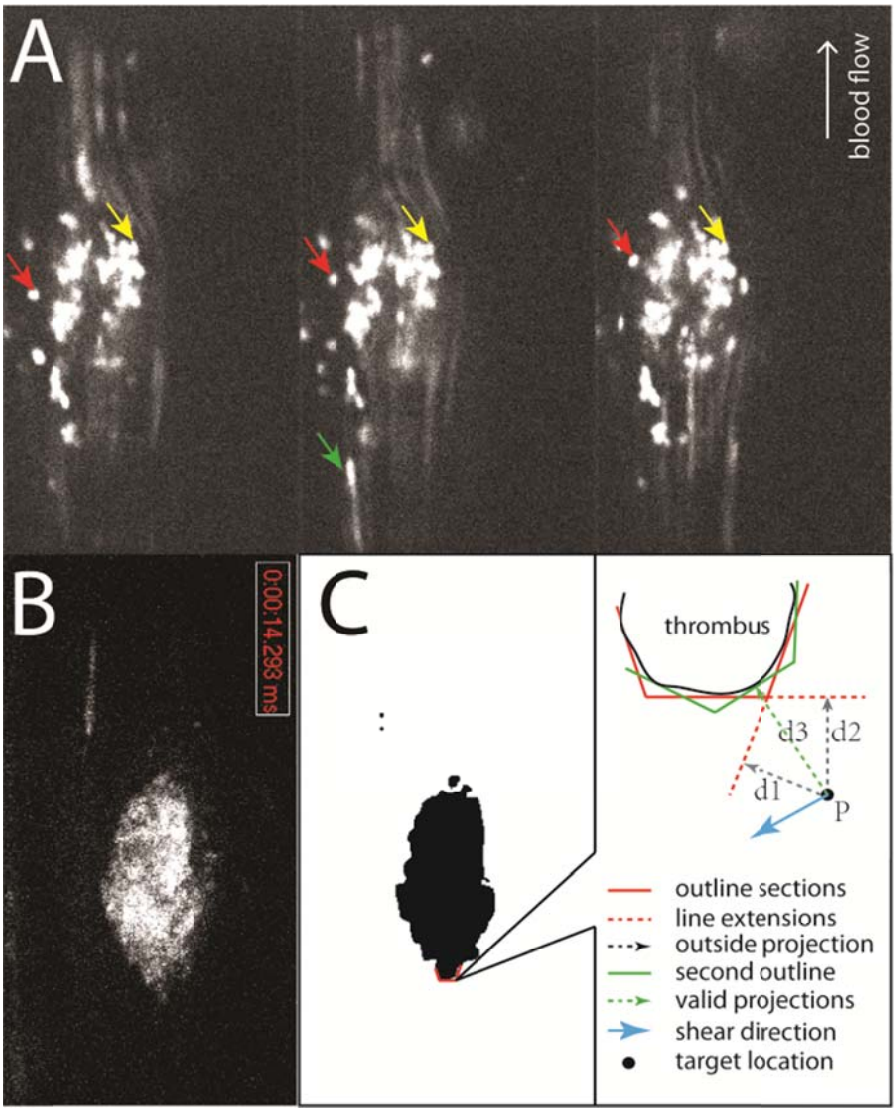

Figure 4.1 A. Three representative consecutive frames of microscopic images at early stage hemostasis (<60 s after laser induced injury). The red arrow points to a translocating platelet, the yellow arrow points to an adherent platelet and the green arrow indicates the trajectory of a flowing platelet. B. About 5 min after the initial injury, the fluorescent platelets cover the injury and form a solid thrombus. C. Conversion of pixel color into binary results in a clear thrombus outline. The graphic explanation of the dual-outline strategy is also shown in detail.

All values of distance and area were converted from pixels to actual lengths. The thrombus coverage areas were obtained using an “edge detection” algorithm in ImageJ after enhancing the contrast of the original microscopic images and converting pixel colors to binary. The regions of thrombus growth and decay were determined pixelwise by superimposing consecutive frames of binary images and comparing their differences. The thrombus outlines and trajectories of the flowing platelets were recorded manually in the form of connected line segments.

The blood velocity at a given location and time was approximated from the flowing platelets as follows:

1. A specific duration (number of frames) was chosen by assuming a steady hydrodynamic environment within that time span.
2. A detection radius with origin at the location of interest was defined, and platelet trajectories passing through this circular region were selected, and the velocities obtained from the length of the trajectory in a time of 10 ms.
3. The mean average of all platelet velocities measured was calculated.

The thrombus growth and decay regions within a given time frame were determined by comparing images of thrombus areas (Figure 4.1C) to the initial image of that period. The set of pixels within the thrombus in the initial image but not in later images were defined as the decay area, and pixels not present in the initial thrombus image but present in the thrombus in later images were defined as the growth area. The degrees of decay and growth were calculated by the consistency of such decay/growth trends.

The shear rate at any near-thrombus location was calculated by its definition: the parallel-to-wall velocity gradient perpendicular to the thrombus outline. As stated above,the thrombus outlines are composed of a series of line segments (Figure 4.1C). Given the no-slip boundary condition, the velocity gradient can be simplified as the point velocity divided by its distance to the thrombus. The specific line segment responsible for calculating the shear stress of the target location is chosen by the shortest distance rule, recognizing that the projection of the target location on the line segment should not be located at its extensions. To address this additional limitation, a dual-outline strategy was introduced (Figure 4.1C). The dual-outline method works as follows: a second set of line segments are constructed which stagger with the first set.

A second set of thrombus outlines is needed because the specific line segment responsible for the shear rate calculation must be determined first in order to calculate the shear rate at the target location. However, there may be no such line segment satisfying our criterion, since the projections of the target location on line segments which have the shortest distances to the target may fall outside the lines. A second set of thrombus outlines (green solid line, Fig.1C) is used to compensate such shortfalls. Thus, at any location, one can always find a line segment where the point-line distance correctly represents the distance from the location.

4.3 Results

4.3.1. Platelet distribution

The locations of platelets exhibiting various behaviors within one minute after injury during the early stage of hemostasis were recorded (Figure 4.2A). The three groups of platelets were captured around the center of the injury. However, the extreme locations along the *x*-axis (contact platelets with a |relative *x*| > 2) occurs more frequently upstream. This result can be counterintuitive since both the blood flow disturbance and platelet agonist molecules are convected downstream. The deviation of *y*-coordinates of all the captured platelets is also larger on the upstream side. This may be the result of convergent streamlines downstream of the thrombus, which concentrates the flowing platelets locally and causes deformation of the existing thrombus. There is no significant time-dependency of the distribution of different states of captured platelets (Figure 4.2F-H). The rolling, tethering and firmly adherent platelets can be observed quite evenly across a 60 s time frame.

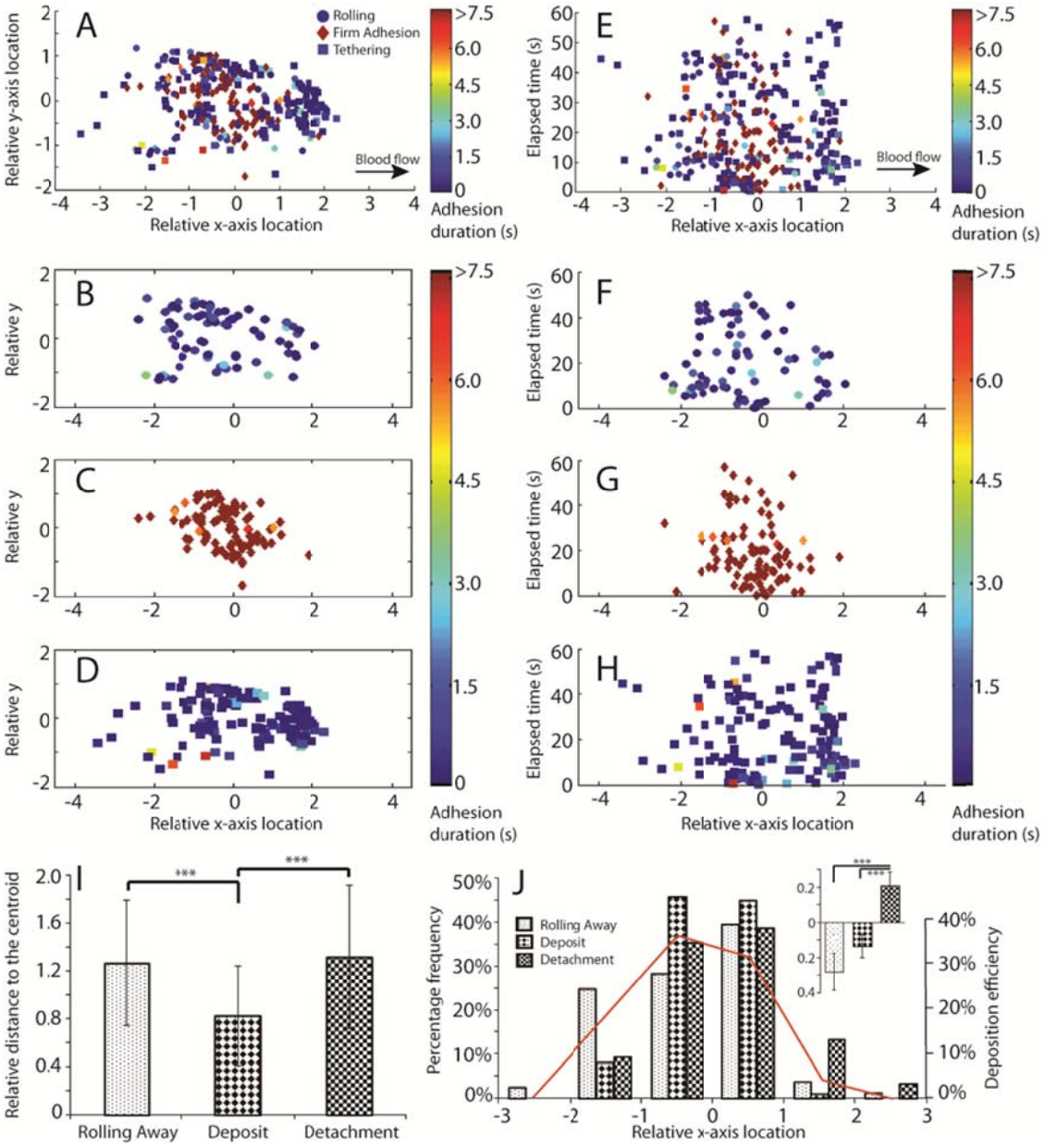

Figure 4.2 Graphic mapping of captured platelets for five experimental sets. The platelets are classified into three observed behaviors. A. Platelets deposition map with their positions relative to the center of the wound. B-D. Separate plots for each group of platelets. E. Platelet deposition position and time. F-H. Separate plots for each group of platelets. (Some adherent platelets last for less than 7.5 s because they are captured towards the end of the 60 s time frame) I. Bar graph showing the distance of three

different groups of platelets from the center of wound, with unpaired t-test performed (error bar shows SD). J. Distribution of three groups of platelets at different locations. The bar graph was generated to represent the number of platelets in each category at that location divided by the total number of platelets in that category. The red line is the ratio of deposited platelets versus the number of platelets in all three categories at that location (deposition efficiency). Unpaired t-test shows the difference of the relative x-axis distribution among the three groups (inset graph with error bars showing SEM).

While the adherent platelets do not detach during the observation period, the majority of the tethering and rolling platelets reside on the developing thrombus for less than a second (Figure 4.2B-D). An interesting observation is that translocation events tend to occur at the peripheral region of the injury while firm adhesion events are more likely to be found near the center. Statistical analysis also confirmed that, compared to the adherent platelets, the rolling and tethering platelets are distributed further away from the center of wound (Figure 4.2I). This evidence directly supports the idea that firmly adherent platelets are densely distributed towards the center of injury site, resulting in effective wound coverage. Our analysis also shows that rolling events occur more frequently upstream of the thrombus, while tethering events are more likely to be found downstream (Figure 4.2J). The platelet deposition efficiency is also calculated at different thrombus locations (Figure 4.2J, red line), suggesting that the highest deposition probability occurs at the central region of the thrombus.

The rate of platelet adhesion was recorded for each of the five independent experiments.

The rate of addition of firmly attached platelets was steady for each experiment, resulting in a constant increase in the number of total adherent platelets (Figure 4.3A). This addition rate is not universal across the experiments, indicating such addition of adherent platelets is affected by factors such as blood flow rate and vessel geometry in different experiments. Within the first 10 s of laser injury, more captured platelets become firm adherent. This shows the immediate physiological response of hemostasis to the exposure of the sub-endothelial layer to the blood stream. The deposition efficiency then approaches a steady number after oscillating for 30 s (Figure 4.3B). The equilibrium fractions of successful deposition events vary among different experiments as well.

Unlike the steady rate of addition of adherent platelets, the effective thrombus coverage area does not always experience a constant increase (Figure 4.3C). This is mainly because of the continuous thrombus fragmentation and platelet detachment. As we can see, out of five experiments, only set one shows a continuous increase and doubles the thrombus size during the 50 s time frame. It also shows that in most cases, the thrombi developed in size within the few s gap between the application of laser and microscopic photography (Figure 4.3C), suggesting that initial platelet attachment is very responsive and flowing platelets almost act immediately after the injury. The platelet deposition rate, which is calculated as the number of deposition events per unit clot area per unit time for five experiments is 6.95 ± 4.73 (SD) $\times 10^{-4}\ s^{-1}\mu m^{-2}$. For each experiment, we defined the average thrombus coverage area determined across a 50 s time frame as the clot area.

It is interesting to note that because of the light diffraction, bright objects in the fluorescent image appear larger than their actual size. Researchers may use point spread

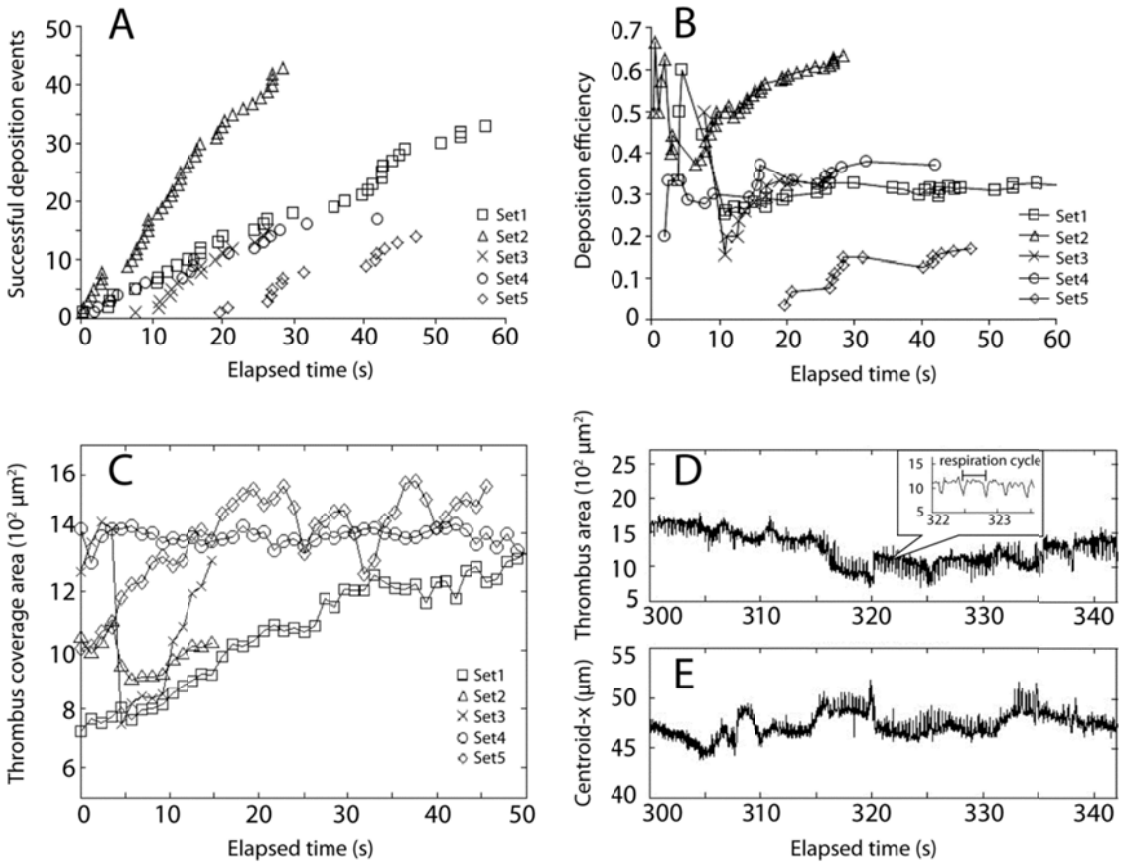

Figure 4.3 Real-time recording of platelet deposition rate and thrombus coverage area. A. The plot of total firm adhesion events versus time for five experiments. B. The deposition efficiency versus time where the deposition efficiency is the accumulated percentage of firm adhesion events versus total number of capture events. C. The thrombus coverage area versus time. D, E. The pulmonary effect on the thrombus coverage area and the center of the wound becomes significant when a solid thrombus forms.

functions (PSF) to adjust the real resolution of confocal microscopy [151]. In our case, the diffraction exaggerates the coverage area of the developing thrombus, especially in the very early stage when adherent platelets are distributed relative sparsely on the wound. When a solid thrombus forms as in Figure 4.1B, such bias is reduced due to the overlap of adherent platelets. As a result, the variation of the thrombus size is understated in Figure 4.3C.

4.3.2. Thrombus shape dynamics

As time progresses (~5 min after injury), the developing thrombus shows a solid appearance (Figure 4.1B). When the pulmonary effect, resulting from the mouse breathing motion, starts to become observable (Figure 4.3D, E) it affects the quality of the measurement. However, the pulmonary effect remains local (~ 0.3 s for each pulmonary cycle) and does not affect the thrombus dynamics, which show variation on a larger time scale (~3 s). Because the whole injury area was well covered by fluorescent platelets (Fig.1B) after 5 min of injury, it would be difficult to record individual platelet capture events. However, thrombus dynamics can be studied according to its changing shape and surrounding hydrodynamic environment.

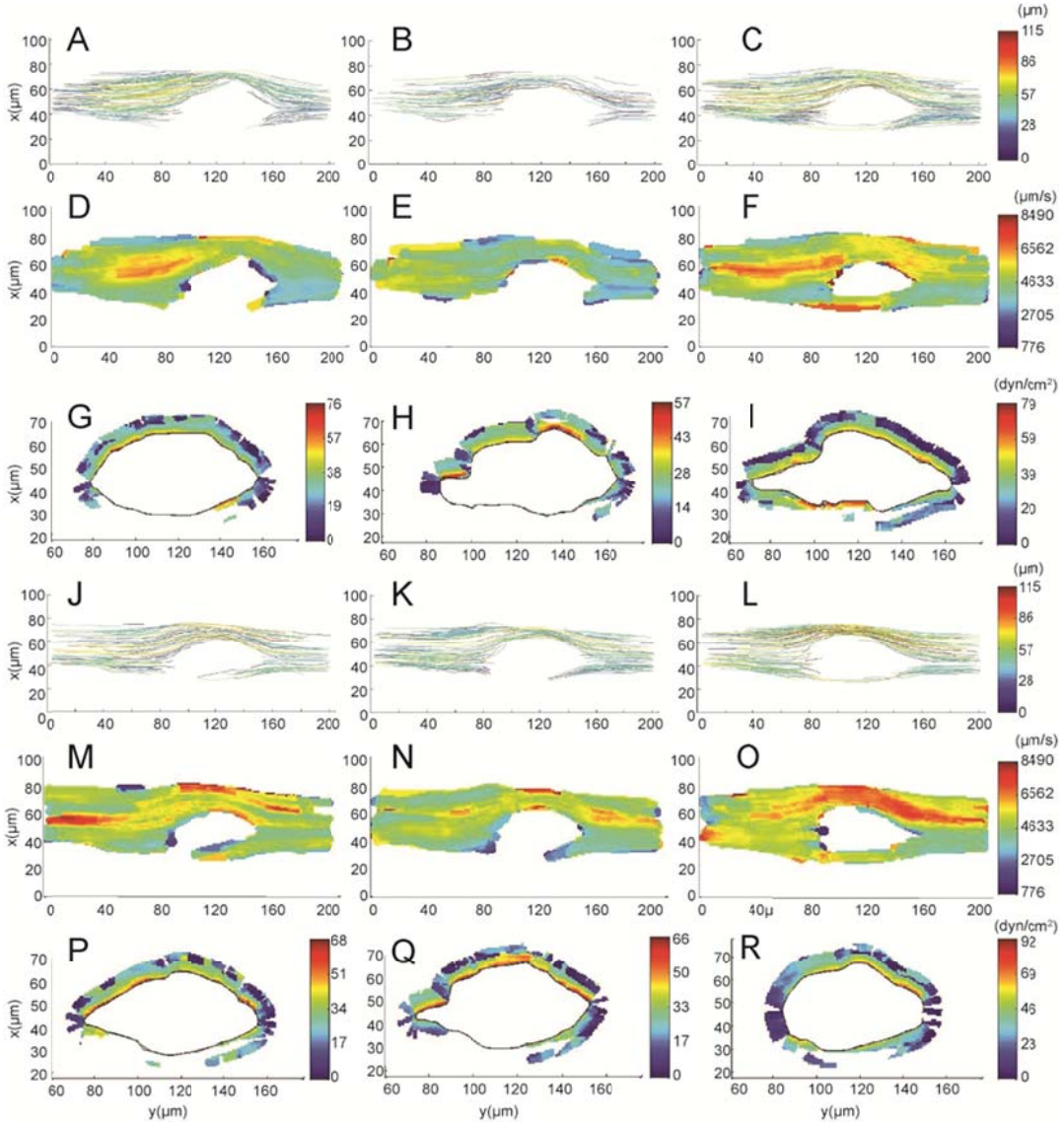

Figure 4.4 Platelet trajectories and the recovery of velocity field and shear stress plot of six time periods, with each period consisting of 500 frames of consecutive images. A – C, J – L. Collection of platelet trajectories with color indicating the trajectory contour lengths. D – F, M – O. The 2D-velocity field recovered from the trajectories of flowing platelets. G – I, P – R. The shear stress plot of the near-thrombus region is shown. The thrombus outlines are taken from the shape of the thrombus at the midpoint of the chosen time period.

A specific time period was chosen for the hydrodynamic calculation. This 7.1-s period (~500 frames) was long enough that sufficient platelet trajectories were collected to recover the velocity field. We assume that the thrombus shape remained unchanged and led to a steady flow. Six consecutive periods from one mouse experiment were analyzed (Figure 4.4), with trajectories, velocity fields and wall shear stress shown separately. The velocity fluctuation among different time periods was significant (Figure 4.4 D – F, M – O). The shear stress distribution along the thrombus outline also varied significantly across the total of 43 s. The major reason for such change is likely due to the dynamics of the thrombus shape.

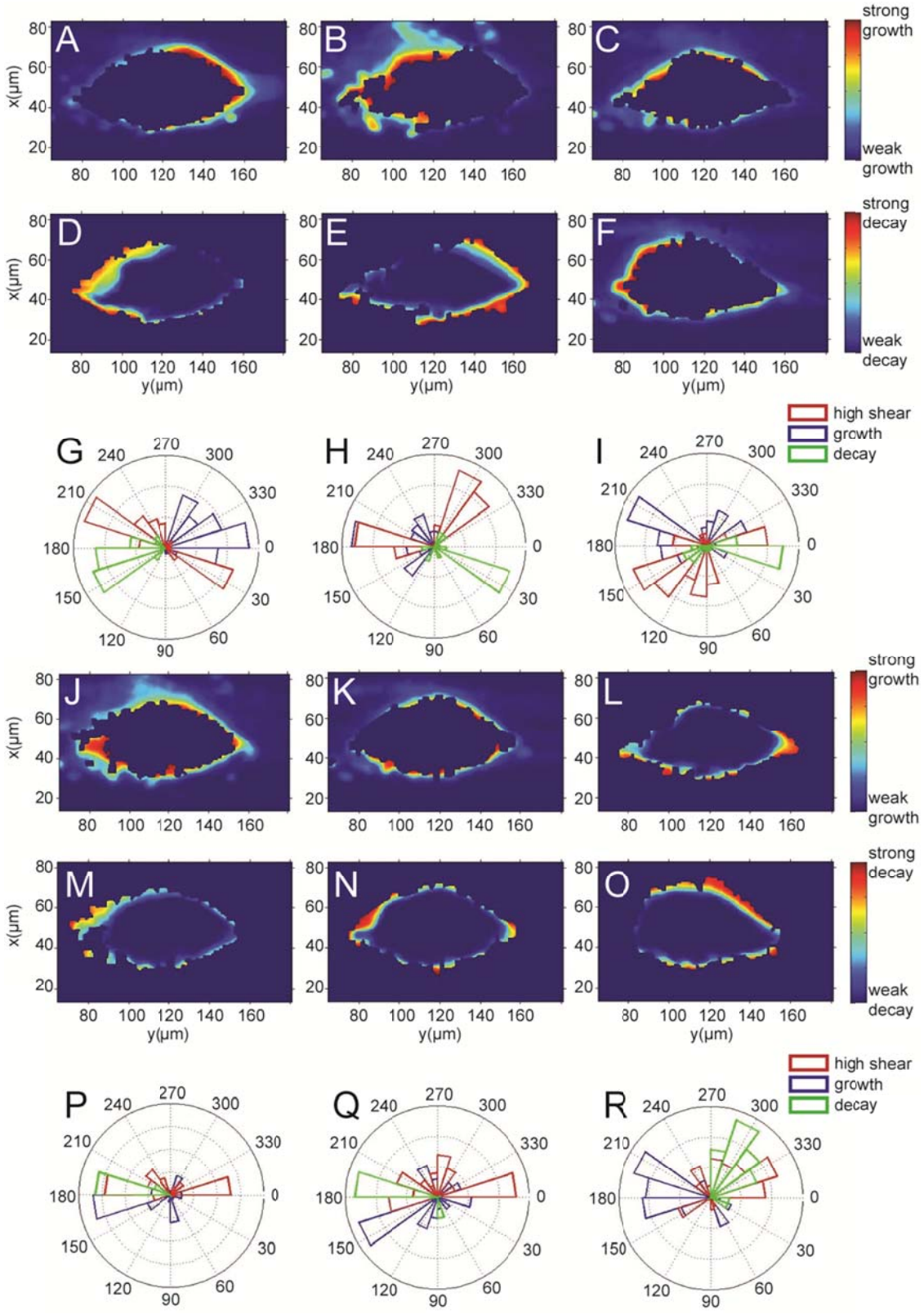
A
B
C
D
E
F
G
H
I
J
K
L
M
N
O
P
Q
R
x(μm)
y(μm)
strong growth
weak growth
strong decay
weak decay
high shear
growth
decay

Figure 4.5 Thrombus shape dynamics and its correlation to the hydrodynamic environment of six time periods the same as shown in Figure 4.4 A – C, J – L. Mapping of thrombus growth region. D – F, M – O. Mapping of thrombus decay region. G – I, P – R. Comparing frequencies of the angular position (in polar coordinates) of thrombus growth, decay and shear stress field. All the polar coordinates are centered to the thrombus centroid and the magnitude of the frequencies are normalized in each category to show the relative frequencies.

The thrombus shapes were recorded according to the time frames in Figure 4.4. Overlapping the images generated the maps of decay and growth (Figure 4.5 A - F, J - O), which directly indicate the rapid shape change of the thrombus outline. For the whole 42 s period, the target thrombus continuously grows and decays at different locations but overall does not undergo an observable shift (Figure 4.5 G-I, P-R). It is understandable that the decay and growth regions are spatially well separated within each ~7 s period. However, it is of interest to note, that the high shear stress region did not overlap with either the growth or decay areas. In fact, these three categories of behaviors tend to exclude each other (Figure 4.5 G-I, P-R.)

4.4 Discussion

Thrombus dynamics are a critical aspect of hemostasis involving new platelet addition and thrombus fragmentation. In the early stages of hemostasis, the thrombus growth rate prevails over the dissolving rate to develop an effective plug to cover the wound. Given that our observations showed the platelet addition rate to be fairly steady, the variable that most affected the overall thrombus growth rate was the fragmentation of small platelet aggregates, which can be calculated as the overall growth rate minus the platelet addition rate. The overall thrombus growth rate and the platelet addition rate vary in each individual experiment, suggesting vessel geometry and wound shape are critical determinants in thrombus dynamics.

The thrombus dynamics also vary with time. While the initial response of platelets to the wound occurs so rapidly that our method was not able to recover the platelet attachment

process in the first few s after injury, Figure 4.3C indicates that this time frame is critical. For a vessel wound of microscopic size, it takes less than five minutes for platelets to cover the injury area. The deformation of the thrombus may not be solely caused by platelet addition/thrombus fragmentation, as visible deformation of the thrombus towards the downstream direction driven by the blood flow was also observed. The thrombus morphology shows a similar shape compared to *in vitro* observations [152], with an aspect ratio that varies between 1.7 to 2.1 and the longer axis consistent with the direction of flow (Figure 4.5).

High shear stress is believed to enhance platelet deposition through various known mechanisms. However, high shear stress also represents a high convection velocity of plasma, which reduces the residence time of the flowing platelet in the local injury region [23] and reduces the chance of firm adhesion. Such antagonism may generate an "optimal" shear stress range for local thrombus development, explaining the result that the high shear stress region was likely to expel either growing or decaying areas. Our Newtonian assumption (constant viscosity) may affect the accuracy of our hydrodynamic calculations. However, such an effect is believed to be small since blood behaves close to a Newtonian fluid when the shear stress is larger than 1 Pa [153], and our results showed that shear stress typically extends over 9 Pa close to the thrombus.

The uncontrolled development of the thrombus leads to pathological conditions such as stenosis. How the thrombus "knows" when to stop growing remains unclear (maybe related to increased force on VWF – exposing the cryptic A2 domain – permiting

ADAMTS13 to cleave) One school of thought utilizes numerical methods and argues that stopping the growth of a developing thrombus may result in its exterior being removed by the flow and expose its non-adhesive core [154]. This mechanism has not yet been verified by experiments. Our cell trajectory-based method to recover the flow conditions and thrombus geometry serves as a good candidate to observe such phenomena in *vivo*. This method can be further expanded in 3D with serial confocal images taken at different focal depths. By consolidating platelet trajectories as well as the thrombus surface outlines that pass through different focal planes, the changing 3D hydrodynamic environment and the 3D thrombus geometry can be determined in real-time.

In conclusion, our study quantitatively measures the thrombus dynamics in the early stages of hemostasis. The equilibrium between thrombus growth and decay are essential for maintaining normal hemostatic functions. Such antagonistic mechanisms also adapt the changing hydrodynamic environment to ensure the rapid and safe formation of a thrombus.

CHAPTER 5: CONCLUSIONS & FUTURE WORKS

5.1 Conclusions

The main results can be classified into four categories which follow the timeline of the initiation of hemostasis.

5.1.1 Platelet-wall interaction

The initiation of hemostasis is mediated by tethering / translocation (rolling) of platelets on an injured vessel surface. Our simulation model successfully recaptured this process for small time/length scales. We determined that ellipsoid-shaped platelets roll differently from spherical cells. Under simple shear flow, they usually remain stationary for a period of time, followed by a fast flipping motion, then back to stationary for some time again. As a result, platelet rolling velocity is an average velocity between the combination of fast flipping motion and long stationary motion.

The rolling behavior is actually a combination of hydrodynamics and constant bond formation and breakage. The classical Bell Model (slip bond) was applied as the governing equation for bond kinetics. Our simulations indicated that, in a wide range of flow rates (from 100 s^{-1} to 2500 s^{-1}), there are usually less than ten GPIbα-vWF bonds existing in the system, which is about half the number of bonds existing for leukocyte rolling on an endothelial layer [155]. The average GPIbα-vWF bond lifetime changes with changing flow rate, but it is usually under 0.1 s. The rolling velocity increases from 3 μm/s at a shear rate of 100 s^{-1} to about 500 μm/s at a shear rate of 2500 s^{-1}. Doubling the total number of receptors on the cell surface decreases rolling velocities and vice

versa. The tethering efficiency shows a parabolic curve, with increasing efficiency when shear rate increases from 100 s^{-1} to 1250 s^{-1}, then drops when shear rate further increases, suggesting that although increased flow rate increases the slip velocity between the cell and the vessel wall and thus increases the chance to form bonds, the interaction time window decreases at the same time.

When the catch-slip combination kinetics are applied, the platelet rolls much slower at higher shear rate. This rolling behavior resembles the *in vitro* rolling experiments. The bond lifetime remains at an order of magnitude of 0.1 s under catch-slip conditions.

5.1.2 Free platelet-adherent platelet interaction

Once the captured platelet stops rolling and becomes fully stationary, it serves as a "seed" to trap other flowing platelets to join the growing thrombus. We determined that such secondary platelet recruitment, which is based on contact time and contact area, actually shows preference when the flowing platelet has a deviation in the direction perpendicular to the flow direction. This property helps flowing platelets to bind and cover a wide range of vessel area rather than superimposing on the top of the previous adherent platelet.

The contact map of the adherent platelet (Figure 2.6) also shows that flowing platelets have a greater chance to interact with it on the peripheral region rather on the top. This results from a combination of platelet-platelet distance, local flow velocity and flowing platelet orientation. The trajectory of the flowing platelet also shows that, when it glides over the side of an adherent platelet, it tends to be pushed sideways by the flow.

5.1.3 Platelet-thrombus interaction

After the "seed" platelet recruits more platelets to the injury site and forms an immature thrombi, the local bump on the injured vessel surface is significantly larger than a single adherent platelet. The size is sufficiently large that it starts to alter the flow pattern inside the entire vessel lumen. The existence of a sizable thrombus slows down the overall volumetric flow but generally increases flow velocity at a given location in the lumen. Along the streamline passing the thrombus, the fluid velocity does not simply increase. It experiences stagnation zones upstream and downstream of the thrombus, which further increases the velocity gradient along the path. The near-wall shear rate at the site of a thrombus is a function of the percentage area stenosis and this effect is not sensitive to the detailed thrombus shape. While it is reasonable to expect that fluid velocities will increase with increasing stenosis, a super-linear relationship between the two may not be obvious. Our model reproduces such a super-linear relationship as recorded by *in vivo* Doppler assay.

Aside from the thrombus geometry, deformable erythrocytes (red blood cells, or RBCs) also play important roles in hemostasis. RBCs create a non-Newtonian environment and platelet trajectories actually converge more after passing by the thrombus than diverge before reaching the thrombus. RBCs also directly enhance the platelet deposition potential. Margination effect causes RBCs to stay in the center of the lumen while pushing platelets towards the vessel wall. As a result, when the blood flow passes the thrombus, the RBCs may directly push platelets to the thrombus surface to enhance

platelet deposition and thrombus growth.

5.1.4 Thrombus dynamics

Previous results are all related to thrombus development and growth. However, a thrombus cannot continue to grow which might result in blocking the entire vessel. While platelets continue to join the thrombus, adherent platelets also continuously fragment and detach from the thrombus. Uncontrolled thrombus growth and vessel blockage may be devastating to the living individual, especially if such clotting happens in a coronary artery or arteries in the brain. Once a thrombus is reaching an equilibrium size, the platelet deposition rate is similar to the thrombus fragmentation rate. As a result, the thrombus does not grow in size overall.

Our in vivo observations indicate that the platelet deposition rate does not change during the first five minute time window. However, the thrombus growth rate is not constant during those five minutes. We conclude that thrombus fragmentation rate increases with increasing thrombus size. We also recovered the flow field from platelet trajectories. We found out that the thrombus regional decay and growth area do not coincide with the high shear stress region. This phenomenon is probably explained by the theory that high shear stress will enhance thrombus growth through the enhancement of platelet activation and also enhance thrombus fragmentation due to mechanical shear force.

5.2 Future work

There are a number of potential projects which are derived directly from the work

presented in this thesis.

5.2.1 Platelet shape potentially affects its physiological function by changing its translocation / tethering behavior

The platelet's finite size and ellipsoid shape has been long studied. While its size is believed to result in platelet margination and its shape can enhance platelet-wall interaction, it has never been reported how platelet shape will affect the translocation behavior. One way to study this would be to apply the CDL-BIEM method to ellipsoid-shaped platelets with different aspect ratios while keeping their cell volume and surface receptor density the same. Quantitative comparison between their rolling velocities and tethering efficiencies under different flow conditions could elucidate more fundamentals about the significance of platelet shape. This model can be directly associated to clinical data, where patients with a special congenital bleeding disorder, platelet spherocytosis, lose their normal platelet morphology and turn to spherical shape [156].

5.2.2 A 3D platelet deposition/ thrombus growth model that includes deformable RBCs

One potential enhancement of the 3D vessel-deformable RBCs-platelet model presented in Chapter 3 would be to add receptor-ligand adhesion to the model. Addition of an adhesion module would grant the model capabilities of assessing the platelet aggregation / thrombus development under different vessel geometries, flow rate as well as bond kinetics. The similar method of allocating receptors on the cell mesh surface introduced in Chapter 2 could be applied here. However, one thing worth mention here is that the

mesh structures between the two models are different, thus full attention should be paid to the area of each surface element.

While one could reproduce the platelet translocation motion by adding an adhesion module, a thrombus development model would be extremely impactful. Keeping adherent cells as ellipsoid shaped particles causes a problem of hydrodynamic calculation because numerical difficulties arise when the surfaces are close to each other. One solution could be to merge the cell into the vessel wall. The method about how adhering platelets join the vessel wall could be achieved by removing the adherent platelet while creating a bump (adjusting the mesh coordinates of the wall) at the site of adhesion. Of course, one would need to develop an algorithm to make such merges spatially smooth, and the hydrodynamic calculation should also be verified.

5.2.3 An analytical solution of spherical cell translocation

Krasik and her colleagues established a semi-analytical leukocyte rolling model [157] in 2004. While this method reduces the CPU cost of complicated Monte Carlo simulation by a factor of ~1000, it still requires about an hour to complete individual simulations. Hence, Dr. Koch and I discussed the idea of establishing a purely analytical model which can calculate the rolling velocities of any type of spherical cells in minutes. Details can be found in Appendix A.

REFERENCES

1. Davi G, Patrono C (2007) Platelet activation and atherothrombosis. N Engl J Med 357: 2482-2494.
2. Kroll MH, Harris TS, Moake JL, Handin RI, Schafer AI (1991) von Willebrand factor binding to platelet GpIb initiates signals for platelet activation. J Clin Invest 88: 1568-1573.
3. Savage B, Saldivar E, Ruggeri ZM (1996) Initiation of platelet adhesion by arrest onto fibrinogen or translocation on von Willebrand factor. Cell 84: 289-297.
4. Laurens N, Koolwijk P, de Maat MP (2006) Fibrin structure and wound healing. J Thromb Haemost 4: 932-939.
5. Colman RW (2006) Hemostasis and thrombosis : basic principles and clinical practice. Philadelphia, PA: Lippincott Williams & Wilkins. xxiv, 1827 p. p.
6. Xu Z, Kamocka M, Alber M, Rosen ED (2011) Computational approaches to studying thrombus development. Arterioscler Thromb Vasc Biol 31: 500-505.
7. Xu ZL, Lioi JH, Mu JA, Kamocka MM, Liu XM, et al. (2010) A multiscale model of venous thrombus formation with surface-mediated control of blood coagulation cascade (vol 98, pg 1723, 2010). Biophysical Journal 99: 2384-2385.
8. Pivkin IV, Richardson PD, Karniadakis G (2006) Blood flow velocity effects and role of activation delay time on growth and form of platelet thrombi. Proc Natl Acad Sci U S A 103: 17164-17169.
9. Fogelson AL (1992) Continuum Models of Platelet-Aggregation - Formulation and Mechanical-Properties. Siam Journal on Applied Mathematics 52: 1089-1110.

10. Wang NT, Fogelson AL (1999) Computational methods for continuum models of platelet aggregation. Journal of Computational Physics 151: 649-675.
11. Fogelson AL, Guy RD (2004) Platelet-wall interactions in continuum models of platelet thrombosis: formulation and numerical solution. Mathematical Medicine and Biology-a Journal of the Ima 21: 293-334.
12. Kuharsky AL, Fogelson AL (2001) Surface-mediated control of blood coagulation: The role of binding site densities and platelet deposition. Biophysical Journal 80: 1050-1074.
13. Mody NA, King MR (2008) Platelet adhesive dynamics. Part II: high shear-induced transient aggregation via GPIbalpha-vWF-GPIbalpha bridging. Biophys J 95: 2556-2574.
14. Mody NA, King MR (2008) Platelet adhesive dynamics. Part I: characterization of platelet hydrodynamic collisions and wall effects. Biophys J 95: 2539-2555.
15. Tokarev AA, Butylin AA, Ermakova EA, Shnol EE, Panasenko GP, et al. (2011) Finite Platelet Size Could Be Responsible for Platelet Margination Effect. Biophysical Journal 101: 1835-1843.
16. Munn LL, Dupin MM (2008) Blood cell interactions and segregation in flow. Annals of Biomedical Engineering 36: 534-544.
17. Zhao R, Kameneva MV, Antaki JF (2007) Investigation of platelet margination phenomena at elevated shear stress. Biorheology 44: 161-177.
18. Merrill EW (1969) Rheology of Blood. Physiological Reviews 49: 863-&.
19. Murata T (1983) Theory of Non-Newtonian Viscosity of Red-Blood-Cell Suspension - Effect of Red-Cell Deformation. Biorheology 20: 471-483.

20. Einav S, Bluestein D (2004) Dynamics of blood flow and platelet transport in pathological vessels. Cardiac Engineering: From Genes and Cells to Structure and Function 1015: 351-366.
21. Anderson JD (1995) Computational fluid dynamics : the basics with applications. New York: McGraw-Hill. xxiv, 547 p. p.
22. Steinman DA (2002) Image-based computational fluid dynamics modeling in realistic arterial geometries. Annals of Biomedical Engineering 30: 483-497.
23. Rayz VL, Boussel L, Ge L, Leach JR, Martin AJ, et al. (2010) Flow Residence Time and Regions of Intraluminal Thrombus Deposition in Intracranial Aneurysms. Annals of Biomedical Engineering 38: 3058-3069.
24. Brady JF, Bossis G (1988) Stokesian Dynamics. Annual Review of Fluid Mechanics 20: 111-157.
25. Mori D, Yano K, Tsubota K, Ishikawa T, Wada S, et al. (2008) Simulation of platelet adhesion and aggregation regulated by fibrinogen and von Willebrand factor. Thromb Haemost 99: 108-115.
26. Mori D, Yano K, Tsubota K, Ishikawa T, Wada S, et al. (2008) Computational study on effect of red blood cells on primary thrombus formation. Thromb Res 123: 114-121.
27. Hyakutake T, Matsumoto T, Yanase S (2006) Lattice Boltzmann simulation of blood cell behavior at microvascular bifurcations. Mathematics and Computers in Simulation 72: 134-140.

28. MacMeccan RM, Clausen JR, Neitzel GP, Aidun CK (2009) Simulating deformable particle suspensions using a coupled lattice-Boltzmann and finite-element method. Journal of Fluid Mechanics 618: 13-39.
29. Wu JS, Aidun CK (2010) Simulating 3D deformable particle suspensions using lattice Boltzmann method with discrete external boundary force. International Journal for Numerical Methods in Fluids 62: 765-783.
30. Yamaguchi T, Ishikawa T, Imai Y, Matsuki N, Xenos M, et al. (2010) Particle-Based Methods for Multiscale Modeling of Blood Flow in the Circulation and in Devices: Challenges and Future Directions. Annals of Biomedical Engineering 38: 1225-1235.
31. Filipovic N, Kojic M, Tsuda A (2008) Modelling thrombosis using dissipative particle dynamics method. Philosophical Transactions of the Royal Society a-Mathematical Physical and Engineering Sciences 366: 3265-3279.
32. Pivkin IV, Richardson PD, Karniadakis GE (2009) Effect of Red Blood Cells on Platelet Aggregation. Ieee Engineering in Medicine and Biology Magazine 28: 32-37.
33. Kim S, Karrila SJ (1991) Microhydrodynamics : principles and selected applications. Boston: Butterworth-Heinemann. xxiii, 507 p. p.
34. Mody NA, King MR (2005) Three-dimensional simulations of a platelet-shaped spheroid near a wall in shear flow. Physics of Fluids 17: 113302.
35. Mackman N, Tilley RE, Key NS (2007) Role of the extrinsic pathway of blood coagulation in hemostasis and thrombosis. Arteriosclerosis Thrombosis and Vascular Biology 27: 1687-1693.
36. Lippi G, Favaloro EJ, Franchini M, Guidi GC (2009) Milestones and Perspectives in Coagulation and Hemostasis. Seminars in Thrombosis and Hemostasis 35: 9-22.

37. Gailani D, Renne T (2007) Intrinsic pathway of coagulation and arterial thrombosis. Arteriosclerosis Thrombosis and Vascular Biology 27: 2507-2513.

38. Undas A, Ariens RAS (2011) Fibrin Clot Structure and Function A Role in the Pathophysiology of Arterial and Venous Thromboembolic Diseases. Arteriosclerosis Thrombosis and Vascular Biology 31: E88-E99.

39. Ataullakhanov FI, Panteleev MA (2005) Mathematical modeling and computer simulation in blood coagulation. Pathophysiol Haemost Thromb 34: 60-70.

40. Diamond SL (2009) Systems biology to predict blood function. Journal of Thrombosis and Haemostasis 7: 177-180.

41. Lo K, Denney WS, Diamond SL (2005) Stochastic modeling of blood coagulation initiation. Pathophysiology of Haemostasis and Thrombosis 34: 80-90.

42. Chatterjee MS, Denney WS, Jing HY, Diamond SL (2010) Systems Biology of Coagulation Initiation: Kinetics of Thrombin Generation in Resting and Activated Human Blood. Plos Computational Biology 6.

43. Luan D, Zai M, Varner JD (2007) Computationally derived points of fragility of a human cascade are consistent with current therapeutic strategies. PLoS Comput Biol 3: e142.

44. Luan D, Szlam F, Tanaka KA, Barie PS, Varner JD Ensembles of uncertain mathematical models can identify network response to therapeutic interventions. Mol Biosyst 6: 2272-2286.

45. Fogelson AL, Tania N (2005) Coagulation under flow: the influence of flow-mediated transport on the initiation and inhibition of coagulation. Pathophysiology of Haemostasis and Thrombosis 34: 91-108.

46. Leiderman K, Fogelson AL (2011) Grow with the flow: a spatial-temporal model of platelet deposition and blood coagulation under flow. Mathematical Medicine and Biology-a Journal of the Ima 28: 47-84.
47. Fogelson AL, Hussain YH, Leiderman K (2012) Blood Clot Formation under Flow: The Importance of Factor XI Depends Strongly on Platelet Count. Biophysical Journal 102: 10-18.
48. Jones KC, Mann KG (1994) A Model for the Tissue Factor Pathway to Thrombin .2. A Mathematical Simulation. Journal of Biological Chemistry 269: 23367-23373.
49. Xu Z, Chen N, Kamocka MM, Rosen ED, Alber M (2008) A multiscale model of thrombus development. J R Soc Interface 5: 705-722.
50. Weisel JW (2007) Structure of fibrin: impact on clot stability. J Thromb Haemost 5 Suppl 1: 116-124.
51. Fogelson AL, Keener JP Toward an understanding of fibrin branching structure. Phys Rev E Stat Nonlin Soft Matter Phys 81: 051922.
52. Sakariassen KS, Bolhuis PA, Sixma JJ (1979) Human blood platelet adhesion to artery subendothelium is mediated by factor VIII-Von Willebrand factor bound to the subendothelium. Nature 279: 636-638.
53. Jung SM, Moroi M (2000) Activation of the platelet collagen receptor integrin alpha(2)beta(1): its mechanism and participation in the physiological functions of platelets. Trends Cardiovasc Med 10: 285-292.
54. Bennett JS (2005) Structure and function of the platelet integrin alphaIIbbeta3. J Clin Invest 115: 3363-3369.

55. Hammer DA, Apte SM (1992) Simulation of cell rolling and adhesion on surfaces in shear flow: general results and analysis of selectin-mediated neutrophil adhesion. Biophys J 63: 35-57.

56. Bell GI (1978) Models for the specific adhesion of cells to cells. Science 200: 618-627.

57. King MR, Hammer DA (2001) Multiparticle adhesive dynamics: hydrodynamic recruitment of rolling leukocytes. Proc Natl Acad Sci U S A 98: 14919-14924.

58. King MR, Hammer DA (2001) Multiparticle adhesive dynamics. Interactions between stably rolling cells. Biophys J 81: 799-813.

59. Mody NA, King MR (2007) Influence of Brownian motion on blood platelet flow behavior and adhesive dynamics near a planar wall. Langmuir 23: 6321-6328.

60. Doggett TA, Girdhar G, Lawshe A, Schmidtke DW, Laurenzi IJ, et al. (2002) Selectin-like kinetics and biomechanics promote rapid platelet adhesion in flow: the GPIb(alpha)-vWF tether bond. Biophys J 83: 194-205.

61. Arya M, Anvari B, Romo GM, Cruz MA, Dong JF, et al. (2002) Ultralarge multimers of von Willebrand factor form spontaneous high-strength bonds with the platelet glycoprotein Ib-IX complex: studies using optical tweezers. Blood 99: 3971-3977.

62. Yago T, Lou J, Wu T, Yang J, Miner JJ, et al. (2008) Platelet glycoprotein Ibalpha forms catch bonds with human WT vWF but not with type 2B von Willebrand disease vWF. J Clin Invest 118: 3195-3207.

63. Coburn LA, Damaraju VS, Dozic S, Eskin SG, Cruz MA, et al. (2011) GPIb alpha-vWF Rolling under Shear Stress Shows Differences between Type 2B and 2M von Willebrand Disease. Biophysical Journal 100: 304-312.

64. Auton M, Zhu C, Cruz MA (2010) The Mechanism of VWF-Mediated Platelet GPIb alpha Binding. Biophysical Journal 99: 1192-1201.

65. Kim J, Zhang CZ, Zhang XH, Springer TA (2010) A mechanically stabilized receptor-ligand flex-bond important in the vasculature. Nature 466: 992-U123.

66. Zucker MB, Nachmias VT (1985) Platelet Activation. Arteriosclerosis 5: 2-18.

67. Munnix ICA, Cosemans JMEM, Auger JM, Heemskerk JWM (2009) Platelet response heterogeneity in thrombus formation. Thrombosis and Haemostasis 102: 1149-1156.

68. Purvis JE, Chatterjee MS, Brass LF, Diamond SL (2008) A molecular signaling model of platelet phosphoinositide and calcium regulation during homeostasis and P2Y1 activation. Blood 112: 4069-4079.

69. Purvis JE, Radhakrishnan R, Diamond SL (2009) Steady-state kinetic modeling constrains cellular resting states and dynamic behavior. PLoS Comput Biol 5: e1000298.

70. Sorensen EN, Burgreen GW, Wagner WR, Antaki JF (1999) Computational simulation of platelet deposition and activation: I. Model development and properties. Annals of Biomedical Engineering 27: 436-448.

71. Sorensen EN, Burgreen GW, Wagner WR, Antaki JF (1999) Computational simulation of platelet deposition and activation: II. Results for Poiseuille flow over collagen. Annals of Biomedical Engineering 27: 449-458.

72. Chu SG, Becker RC, Berger PB, Bhatt DL, Eikelboom JW, et al. Mean platelet volume as a predictor of cardiovascular risk: a systematic review and meta-analysis. J Thromb Haemost 8: 148-156.

73. Mody NA, Lomakin O, Doggett TA, Diacovo TG, King MR (2005) Mechanics of transient platelet adhesion to von Willebrand factor under flow. Biophys J 88: 1432-1443.

74. Wiggs BR, English D, Quinlan WM, Doyle NA, Hogg JC, et al. (1994) Contributions of capillary pathway size and neutrophil deformability to neutrophil transit through rabbit lungs. J Appl Physiol 77: 463-470.

75. Pozrikidis C (2005) Axisymmetric motion of a file of red blood cells through capillaries. Physics of Fluids 17: 031503.

76. Pozrikidis C (2003) Numerical simulation of the flow-induced deformation of red blood cells. Annals of Biomedical Engineering 31: 1194-1205.

77. Zhao H, Isfahani AHG, Olson LN, Freund JB (2010) A spectral boundary integral method for flowing blood cells. Journal of Computational Physics 229: 3726-3744.

78. Jen CJ, Mcintire LV (1982) The Structural-Properties and Contractile-Force of a Clot. Cell Motility and the Cytoskeleton 2: 445-455.

79. Lam WA, Chaudhuri O, Crow A, Webster KD, Li TD, et al. (2011) Mechanics and contraction dynamics of single platelets and implications for clot stiffening. Nature Materials 10: 61-66.

80. Singh I, Themistou E, Porcar L, Neelamegham S (2009) Fluid Shear Induces Conformation Change in Human Blood Protein von Willebrand Factor in Solution. Biophysical Journal 96: 2313-2320.

81. Honn KV, Tang DG, Crissman JD (1992) Platelets and Cancer Metastasis - a Causal Relationship. Cancer and Metastasis Reviews 11: 325-351.

82. Gay LJ, Felding-Habermann B (2011) Contribution of platelets to tumour metastasis. Nature Reviews Cancer 11: 123-134.

83. Gawaz M, Langer H, May AE (2005) Platelets in inflammation and atherogenesis. Journal of Clinical Investigation 115: 3378-3384.

84. Arya M, Kolomeisky AB, Romo GM, Cruz MA, Lopez JA, et al. (2005) Dynamic force spectroscopy of glycoprotein Ib-IX and von Willebrand factor. Biophys J 88: 4391-4401.

85. Kumar RA, Dong JF, Thaggard JA, Cruz MA, Lopez JA, et al. (2003) Kinetics of GPIbalpha-vWF-A1 tether bond under flow: effect of GPIbalpha mutations on the association and dissociation rates. Biophys J 85: 4099-4109.

86. Sadler JE (1994) A revised classification of von Willebrand disease. For the Subcommittee on von Willebrand Factor of the Scientific and Standardization Committee of the International Society on Thrombosis and Haemostasis. Thromb Haemost 71: 520-525.

87. Huizinga EG, Tsuji S, Romijn RA, Schiphorst ME, de Groot PG, et al. (2002) Structures of glycoprotein Ibalpha and its complex with von Willebrand factor A1 domain. Science 297: 1176-1179.

88. Dumas JJ, Kumar R, McDonagh T, Sullivan F, Stahl ML, et al. (2004) Crystal structure of the wild-type von Willebrand factor A1-glycoprotein Ibalpha complex reveals conformation differences with a complex bearing von Willebrand disease mutations. J Biol Chem 279: 23327-23334.

89. Doggett TA, Girdhar G, Lawshe A, Miller JL, Laurenzi IJ, et al. (2003) Alterations in the intrinsic properties of the GPIbalpha-VWF tether bond define the kinetics of the platelet-type von Willebrand disease mutation, Gly233Val. Blood 102: 152-160.

90. Ruggeri ZM (2004) Type IIB von Willebrand disease: a paradox explains how von Willebrand factor works. J Thromb Haemost 2: 2-6.

91. Jackson SP (2007) The growing complexity of platelet aggregation. Blood 109: 5087-5095.

92. Nesbitt WS, Westein E, Tovar-Lopez FJ, Tolouei E, Mitchell A, et al. (2009) A shear gradient-dependent platelet aggregation mechanism drives thrombus formation. Nat Med 15: 665-673.

93. Power H, Miranda G (1987) 2nd Kind Integral-Equation Formulation of Stokes Flows Past a Particle of Arbitrary Shape. Siam Journal on Applied Mathematics 47: 689-698.

94. Reininger AJ, Heijnen HF, Schumann H, Specht HM, Schramm W, et al. (2006) Mechanism of platelet adhesion to von Willebrand factor and microparticle formation under high shear stress. Blood 107: 3537-3545.

95. Bell GI, Dembo M, Bongrand P (1984) Cell adhesion. Competition between nonspecific repulsion and specific bonding. Biophys J 45: 1051-1064.

96. Singh I, Shankaran H, Beauharnois ME, Xiao Z, Alexandridis P, et al. (2006) Solution structure of human von Willebrand factor studied using small angle neutron scattering. J Biol Chem 281: 38266-38275.

97. Fox JE, Aggerbeck LP, Berndt MC (1988) Structure of the glycoprotein Ib.IX complex from platelet membranes. J Biol Chem 263: 4882-4890.

98. Chtcheglova LA, Shubeita GT, Sekatskii SK, Dietler G (2004) Force spectroscopy with a small dithering of AFM tip: a method of direct and continuous measurement of the spring constant of single molecules and molecular complexes. Biophys J 86: 1177-1184.

99. Evans E, Leung A, Heinrich V, Zhu C (2004) Mechanical switching and coupling between two dissociation pathways in a P-selectin adhesion bond. Proceedings of the National Academy of Sciences of the United States of America 101: 11281-11286.

100. King MR, Heinrich V, Evans E, Hammer DA (2005) Nano-to-micro scale dynamics of P-selectin detachment from leukocyte interfaces. III. Numerical simulation of tethering under flow. Biophysical Journal 88: 1676-1683.

101. Chang KC, Hammer DA (2000) Adhesive dynamics simulations of sialyl-Lewis(x)/E-selectin-mediated rolling in a cell-free system. Biophys J 79: 1891-1902.

102. Wang W, Mody NA, King MR (2013) Multiscale model of platelet translocation and collision. J Comput Phys 244: 223-235.

103. Carrell NA, Fitzgerald LA, Steiner B, Erickson HP, Phillips DR (1985) Structure of human platelet membrane glycoproteins IIb and IIIa as determined by electron microscopy. J Biol Chem 260: 1743-1749.

104. Naimushin YA, Mazurov AV (2004) Von Willebrand factor can support platelet aggregation via interaction with activated GPIIb-IIIa and GPIb. Platelets 15: 419-425.

105. Tunc S, Maitz MF, Steiner G, Vazquez L, Pham MT, et al. (2005) In situ conformational analysis of fibrinogen adsorbed on Si surfaces. Colloids Surf B Biointerfaces 42: 219-225.

106. Alevriadou BR, Moake JL, Turner NA, Ruggeri ZM, Folie BJ, et al. (1993) Real-time analysis of shear-dependent thrombus formation and its blockade by inhibitors of von Willebrand factor binding to platelets. Blood 81: 1263-1276.

107. Peterson DM, Stathopoulos NA, Giorgio TD, Hellums JD, Moake JL (1987) Shear-induced platelet aggregation requires von Willebrand factor and platelet membrane glycoproteins Ib and IIb-IIIa. Blood 69: 625-628.

108. Wang WW, King MR (2012) Multiscale Modeling of Platelet Adhesion and Thrombus Growth. Annals of Biomedical Engineering 40: 2345-2354.

109. Goldsmith HL, Turitto VT (1986) Rheological Aspects of Thrombosis and Hemostasis - Basic Principles and Applications - Icth-Report - Subcommittee on Rheology of the International Committee on Thrombosis and Hemostasis. Thrombosis and Haemostasis 55: 415-435.

110. Zhao H, Shaqfeh ES (2011) Shear-induced platelet margination in a microchannel. Phys Rev E Stat Nonlin Soft Matter Phys 83: 061924.

111. Magallon J, Egalka M, Diacovo TG (2011) Humanizing thrombi in mice. Trends Cardiovasc Med 21: 33-36.

112. Chen J, Tan K, Zhou H, Lo HF, Roux DT, et al. (2008) Modifying murine von Willebrand factor A1 domain for in vivo assessment of human platelet therapies. Nat Biotechnol 26: 114-119.

113. Pozrikidis C (1992) Boundary integral and singularity methods for linearized viscous flow. Cambridge [England] ; New York: Cambridge University Press. xi, 259 p. p.

114. Saintillan D, Darve E, Shaqfeh ESG (2005) A smooth particle-mesh Ewald algorithm for Stokes suspension simulations: The sedimentation of fibers. Physics of Fluids 17: 033301.

115. Hasimoto H (1959) On the Periodic Fundamental Solutions of the Stokes Equations and Their Application to Viscous Flow Past a Cubic Array of Spheres. Journal of Fluid Mechanics 5: 317-328.

116. Deserno M, Holm C (1998) How to mesh up Ewald sums. I. A theoretical and numerical comparison of various particle mesh routines. Journal of Chemical Physics 109: 7678-7693.

117. Skalak R, Tozeren A, Zarda RP, Chien S (1973) Strain Energy Function of Red Blood-Cell Membranes. Biophysical Journal 13: 245-280.

118. Freund JB, Orescanin MM (2011) Cellular flow in a small blood vessel. Journal of Fluid Mechanics 671: 466-490.

119. Freund JB, Shapiro B (2012) Transport of particles by magnetic forces and cellular blood flow in a model microvessel. Physics of Fluids 24: 051904.

120. Swarztrauber PN, Spotz WF (2000) Generalized discrete spherical harmonic transforms. Journal of Computational Physics 159: 213-230.

121. Fahraeus R (1929) The suspension stability of the blood. Physiological Reviews 9: 241-274.

122. Sutera SP, Seshadri V, Croce PA, Hochmuth RM (1970) Capillary blood flow. II. Deformable model cells in tube flow. Microvasc Res 2: 420-433.

123. Kumar PJ, Clark ML Kumar & Clark's clinical medicine. Edinburgh: Saunders Elsevier. p. p.

124. Jordan A, David T, Homer-Vanniasinkam S, Graham A, Walker P (2004) The effects of margination and red cell augmented platelet diffusivity on platelet adhesion in complex flow. Biorheology 41: 641-653.

125. Riva CE, Grunwald JE, Sinclair SH, Petrig BL (1985) Blood velocity and volumetric flow rate in human retinal vessels. Invest Ophthalmol Vis Sci 26: 1124-1132.

126. Diacovo TG, Puri KD, Warnock RA, Springer TA, von Andrian UH (1996) Platelet-mediated lymphocyte delivery to high endothelial venules. Science 273: 252-255.

127. Tomaiuolo G, Guido S (2011) Start-up shape dynamics of red blood cells in microcapillary flow. Microvascular Research 82: 35-41.

128. Jackson SP, Nesbitt WS, Westein E (2009) Dynamics of platelet thrombus formation. J Thromb Haemost 7 Suppl 1: 17-20.

129. Grant EG, Benson CB, Moneta GL, Alexandrov AV, Baker JD, et al. (2003) Carotid artery stenosis: Gray-scale and Doppler US diagnosis - Society of Radiologists in Ultrasound consensus conference. Radiology 229: 340-346.

130. Bartlett ES, Symons SP, Fox AJ (2006) Correlation of carotid stenosis diameter and cross-sectional areas with CT angiography. AJNR Am J Neuroradiol 27: 638-642.

131. Murciano JC, Muzykantov VR (2003) Coupling of anti-thrombotic agents to red blood cells offers safer and more effective management of thrombosis. Discov Med 3: 28-29.

132. Phillips DJ, Beach KW, Primozich J, Strandness DE, Jr. (1989) Should results of ultrasound Doppler studies be reported in units of frequency or velocity? Ultrasound Med Biol 15: 205-212.

133. Schrank E, Phillips DJ, Moritz WE, Strandness DE, Jr. (1990) A triangulation method for the quantitative measurement of arterial blood velocity magnitude and direction in humans. Ultrasound Med Biol 16: 499-509.

134. Overbeck JR, Beach KW, Strandness DE, Jr. (1992) Vector Doppler: accurate measurement of blood velocity in two dimensions. Ultrasound Med Biol 18: 19-31.

135. Li Z, Delaney MK, O'Brien KA, Du X (2010) Signaling during platelet adhesion and activation. Arterioscler Thromb Vasc Biol 30: 2341-2349.

136. Dopheide SM, Maxwell MJ, Jackson SP (2002) Shear-dependent tether formation during platelet translocation on von Willebrand factor. Blood 99: 159-167.

137. Kulkarni S, Dopheide SM, Yap CL, Ravanat C, Freund M, et al. (2000) A revised model of platelet aggregation. J Clin Invest 105: 783-791.

138. Frenette PS, Johnson RC, Hynes RO, Wagner DD (1995) Platelets roll on stimulated endothelium in vivo: an interaction mediated by endothelial P-selectin. Proc Natl Acad Sci U S A 92: 7450-7454.

139. Falk E (1985) Unstable angina with fatal outcome: dynamic coronary thrombosis leading to infarction and/or sudden death. Autopsy evidence of recurrent mural thrombosis with peripheral embolization culminating in total vascular occlusion. Circulation 71: 699-708.

140. Lowe GD (1986) Blood rheology in arterial disease. Clin Sci (Lond) 71: 137-146.

141. Ruggeri ZM, Mendolicchio GL (2007) Adhesion mechanisms in platelet function. Circ Res 100: 1673-1685.

142. Lam CK, Yoo T, Hiner B, Liu Z, Grutzendler J (2010) Embolus extravasation is an alternative mechanism for cerebral microvascular recanalization. Nature 465: 478-482.

143. Caplan LR, Hennerici M (1998) Impaired clearance of emboli (washout) is an important link between hypoperfusion, embolism, and ischemic stroke. Arch Neurol 55: 1475-1482.

144. Nash GB, Watts T, Thornton C, Barigou M (2008) Red cell aggregation as a factor influencing margination and adhesion of leukocytes and platelets. Clin Hemorheol Microcirc 39: 303-310.

145. Watts T, Barigou M, Nash GB (2013) Comparative rheology of the adhesion of platelets and leukocytes from flowing blood: why are platelets so small? Am J Physiol Heart Circ Physiol 304: H1483-1494.

146. Karino T, Goldsmith HL (1979) Adhesion of human platelets to collagen on the walls distal to a tubular expansion. Microvasc Res 17: 238-262.

147. Muthard RW, Diamond SL (2013) Side view thrombosis microfluidic device with controllable wall shear rate and transthrombus pressure gradient. Lab Chip 13: 1883-1891.

148. Newman PJ, Aster R, Boylan B (2007) Human platelets circulating in mice: applications for interrogating platelet function and survival, the efficacy of antiplatelet therapeutics, and the molecular basis of platelet immunological disorders. J Thromb Haemost 5 Suppl 1: 305-309.

149. Tsuji S, Sugimoto M, Miyata S, Kuwahara M, Kinoshita S, et al. (1999) Real-time analysis of mural thrombus formation in various platelet aggregation disorders:

distinct shear-dependent roles of platelet receptors and adhesive proteins under flow. Blood 94: 968-975.

150. Zaman AG, Osende JI, Chesebro JH, Fuster V, Padurean A, et al. (2000) In vivo dynamic real-time monitoring and quantification of platelet-thrombus formation: use of a local isotope detector. Arterioscler Thromb Vasc Biol 20: 860-865.

151. Cole RW, Jinadasa T, Brown CM (2011) Measuring and interpreting point spread functions to determine confocal microscope resolution and ensure quality control. Nat Protoc 6: 1929-1941.

152. Colace T, Falls E, Zheng XL, Diamond SL (2011) Analysis of morphology of platelet aggregates formed on collagen under laminar blood flow. Ann Biomed Eng 39: 922-929.

153. Replogle RL, Meiselman HJ, Merrill EW (1967) Clinical implications of blood rheology studies. Circulation 36: 148-160.

154. Tosenberger A, Ataullakhanov F, Bessonov N, Panteleev M, Tokarev A, et al. (2013) Modeling of thrombus growth and growth stop in flow by the method of dissipative particle dynamics. Russian Journal of Numerical Analysis and Mathematical Modeling 27: 16.

155. King MR, Rodgers SD, Hammer DA (2001) Hydrodynamic collisions suppress fluctuations in the rolling velocity of adhesive blood cells. Langmuir 17: 4139-4143.

156. White JG, de Alarcon PA (2002) Platelet spherocytosis: a new bleeding disorder. Am J Hematol 70: 158-166.

157. Krasik EF, Hammer DA (2004) A semianalytic model of leukocyte rolling. Biophys J 87: 2919-2930.

APPENDIX A: PRELIMINARY DATA FOR ANALYTICAL MODEL

Krasik et al. used a bond density distribution function to describe the bonding profiles (number of bonds and their bond forces) to obtain the rolling velocities [157] by applying force / torque balances and bond formation / breakage balances. Their model settings are depicted in Figure A.1. The cell is modeled as a solid sphere, which has a translational velocity V_x and angular velocity ω_x. A specific bond contact zone is manually determined based on the k_{off} threshold value in the Bell Model. When calculating the bond forces, all of the bonds are assumed at one location (as a cluster) and have the same configuration, which results in the same bond force. The bond force is plugged into the hydrodynamic equations, which together with the force balance in the y-direction and the equilibrium bond break and formation, comprise the three main equations.

Preliminary research on this topic has been completed and what I determined is that we can use three key equations to solve for the rolling velocity:

$$k_{on}\left|\tilde{V}-\tilde{r}\times\tilde{\Omega}\right|n_{RT}n_{LG}*A-k_r^0\exp(\frac{\gamma_c F_B}{k_B T})n_b=0$$

$$V+\frac{k_{on}}{n_b}n_{RT}n_{LG}L=2Lk_r^0\exp\left(\frac{\gamma_c F_B}{k_B T}\right)$$

$$F_y^{rep}+F_y^{grav}+F_y^{bond}=0$$

Ultimately, the three unknowns are bond angle θ, the closest distance between the cell and wall H_0, and the number of bonds existing at equilibrium n_b.

The three equations above are not linear. There are many potential methods that can be applied to solve them. Here we can use heuristic optimization methods to solve these equations and find the rolling velocity V. The rationale for utilizing a heuristic method is because of the ease of implementation and independence of the behavior of the equations. Note that optimization methods serve to find the minimum or maximum of a given function. We can move the RHS of these three equations to the left and take the square sum as the cost function f(x) one wishes to minimize. One such heuristic method is called Dynamic Dimensional Search (DDS), which is essentially a "greedy" search algorithm. It uses as an initial guess of the solution x_0, and a maximum iteration number is specified. For each iteration, the method calculates a perturbation probability as:

$$P(i) = 1 - \frac{\ln(i)}{\ln(Max\_iter)}$$

where "i" is the current iteration number. It is expected that the perturbation probability will drop from 1 to 0 as the method progresses. Once one obtains the probability, Monte Carlo method (random number-generation) is used to determine whether a dimension will be perturbed. If yes, another random variable is generated that follows a normal distribution, and this random variable is added to the value of the current solution for the jth dimension $x_{current,\,j}$ as the $x_{new,\,j}$ value. This is done for all the dimensions and one obtains the new solution x_{new}. The cost function is evaluated based on this x_{new}. If it is better than $x_{current}$, that is, if one wishes to minimize f(x) and $f(x_{new})<f(x_{current})$, the $x_{current}$

is replaced with x_{new}. Otherwise, one starts with the previous solution and the perturbation is done again, with

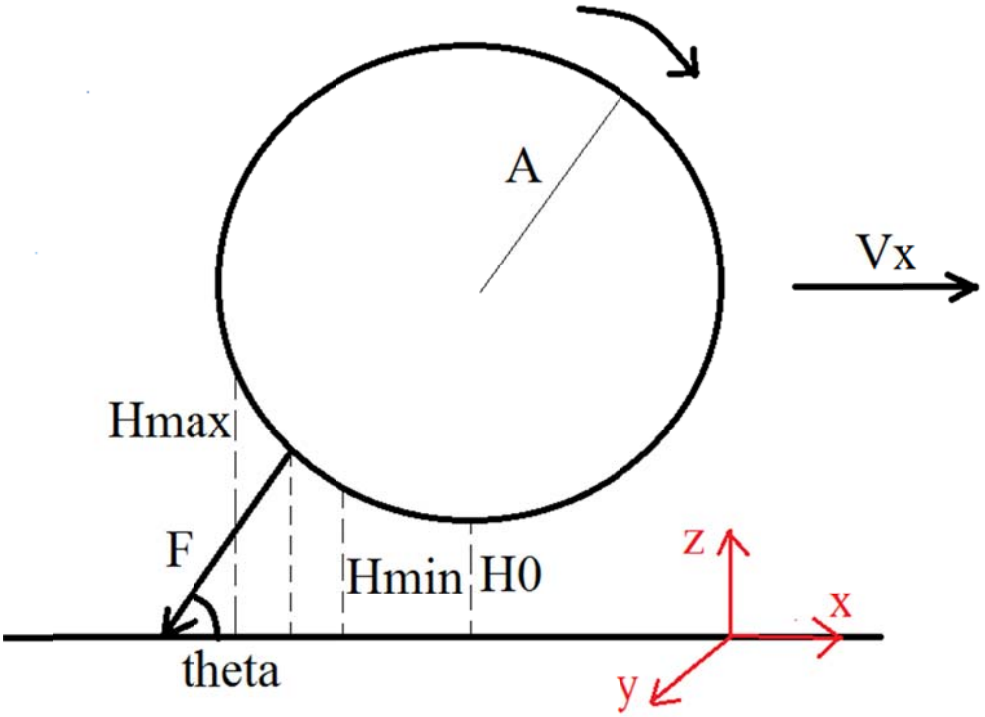

Figure A.1 A graphical sketch depicting the semi-analytical model. The analytical model described here will be using a similar structure. This figure is reproduced from Krasik's 2004 paper [157].

iteration number is increased by one. An example of how cost function value decreases as desired when iteration continues is shown in Figure A.2. The code of the detailed hydrodynamic calculation and DDS method can be found at the end of Appendix A.

Several things are prone to adjustment. Firstly, while the first and third equation are solid and well-behaved, the second equation describes an approximation of the relationship between bond formation / breakage and rolling velocity that may not be accurate. Such inaccuracy could introduce error into this equation set and make it unsolvable. The second issue is how good the solution is before one can claim that these are the precise solutions. This issue involves the scaling of these three equations properly as well as how to set up a threshold value of the cost function to end the iteration in the heuristic method.

Once the model has been established, it is hoped that it could predict the rolling behavior of any type of cells or particles by plugging in appropriate the parameters in the model and solving the equations within minutes.

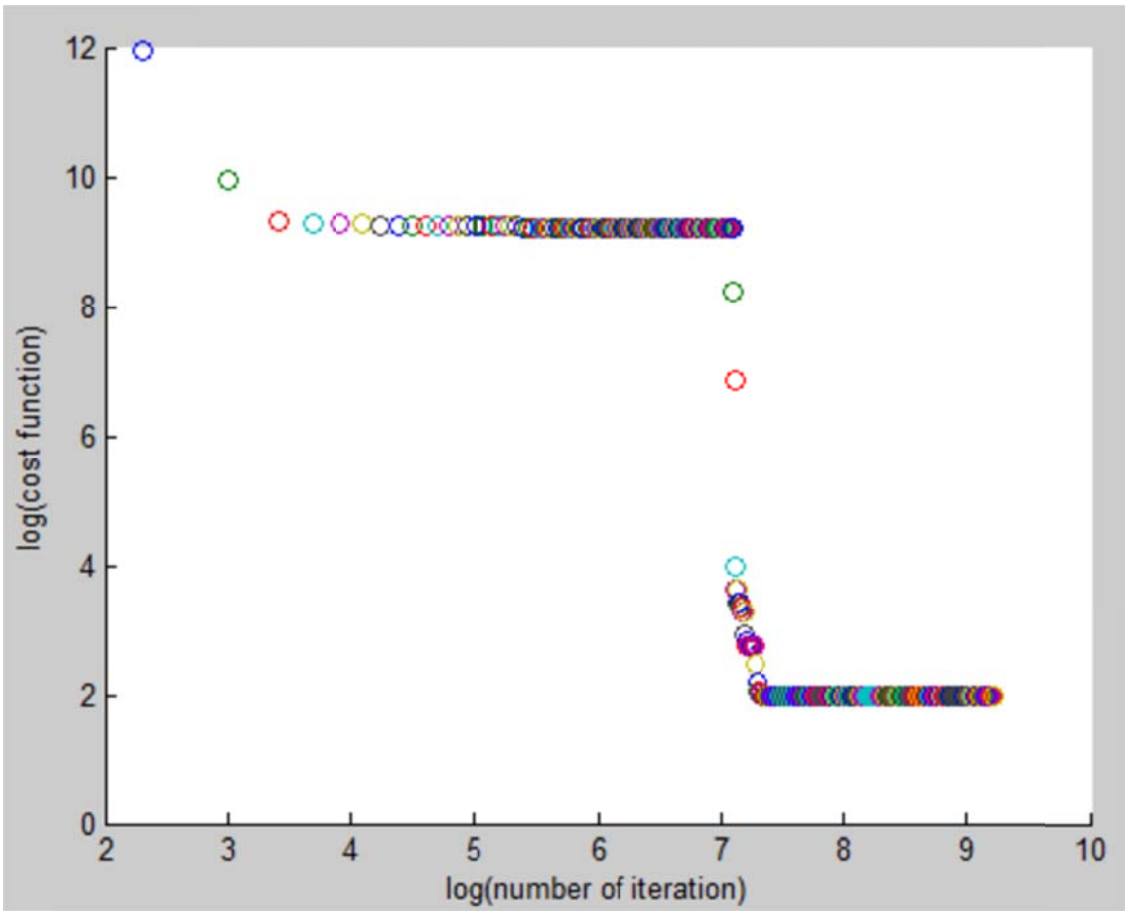

Figure A.2. An example figure showing how the value of the cost function decreases as the number of iteration steps increases. Note it is a minimization problem, and since it is greedy, the function value never increases.

Matlab code for Chapter 5.3: An analytical solution of spherical cell translocation.

```
%%%%%%%%%%%%Weiwei Wang%%%%%%%%%%%%%%%%%%%%%%%%
%the pure analytical solution for spherical particle translocation
%Here we only consider leukocyte rolling
%Play with it try to solve the three ultimate unknowns by three main
%equations. Future parameter tuning is expected
function [err,U] = funEval(H0,n_b,theta)
%hydrodynamics
R = 5; %cell radius, um
shear = 100; %wall shear, s^-1
mu = 0.0035; %viscosity, kg s^-1 m^-1


%bond kinetics
k_on = 0.0005;  %um^-1
k_r = 5; %intrinsic off rate, s^-1
n_RT = 48; %receptor surface density, um^-2
n_LG = 200; %ligand surface density, um^-2
lambda = 0.07; %equilibrium bond length, um
rC = 0.000039; %Reactive compliance, um
%K_B = 1.38*10^(-8); %Boltzman Constant, um^2 g s^-2 k^-1
K_B = 1.380649*10^(-5); % Boltzman Constant, um pN K^-1 Units converted
T = 310; %Temperature, k
%SpringC = 10;% bond spring constant, pN/nm
SpringC = 500;% bond spring constant, pN/um =

Tau = 0.020; %Repulsion characteristic length, um, between 20~70 nm
%Eps = 0.0005; %Nonspecific repulsion constant, dyne
Eps = 50; %Nonspecific repulsion constant, pN, semianalytical paper too large

%unltimate unknown
%H0 = 0; % the distance of the gap between cell and wall, um
%keep in mind that H0 should be very small compare to R. You don't need to
%set this as an optimization constraint, but you need to be able to tell if
%the resulted H0 is in the reasonable range.
%n_b = 0; % number of bonds, cannot <0 of course. But dont set it as an constraint, just keep
this in mind
%theta = 0; % the angle of the bonds cluster to the wall. Also keep in mind this angle should
be >0 and <90 degrees

%intermediate variable
%%hydrodynamics, from Goldman et al. 1967 paper
%%%%the Fxss is known as Fxs star, all dimensionless
%%%%Here all the Ty components are actually Tz in the semi-analytical paper
Fxss = -0.46*(R+H0)/R+2.15;
Tyss = 0.052*(R+H0)/R+0.894;
Fxts = -(8/15*log(H0/R)-0.9588);
```

```
Tyts = -(-1/10*log(H0/R)-0.1895);
Fxrs = -2/15*log(H0/R)-0.2526;
Tyrs = -(2/5*log(H0/R)-0.3817);

D=(Fxts*Tyrs+Fxrs*Tyts);

if 1<1
   disp(['Fxss = ',num2str(Fxss)]);
   disp(['Tyss = ',num2str(Tyss)]);
   disp(['Fxts = ',num2str(Fxts)]);
   disp(['Tyts = ',num2str(Tyts)]);
   disp(['Fxrs = ',num2str(Fxrs)]);
   disp(['Tyrs = ',num2str(Tyrs)]);
end


%geometrical parameters
Hmin = (log(2)*K_B*T/rC/SpringC+lambda);%*sin(theta); %!!!get unit correct and keep in mind,
H0 should be smaller than Hmin
Hmax = (log(500)*K_B*T/rC/SpringC+lambda);%*sin(theta); %!!!get unit correct and keep in
mind, H0 should be smaller than Hmax
if Hmin<H0
   Hmin=H0;
end
if Hmax<H0
   Hmax=H0;
end
Xmin = sqrt(R^2-(R-(Hmin-H0))^2); %!!!Xmin should be smaller than R
Xmax = sqrt(R^2-(R-(Hmax-H0))^2); %!!!Xmax should be smaller than R
if isreal(Xmin)==0 || isreal(Xmax)==0
disp(['H0 = ',num2str(H0)]);
disp(['Hmin = ',num2str(Hmin)]);
disp(['Hmax = ',num2str(Hmax)]);
disp(['Xmin = ',num2str(Xmin)]);
disp(['Xmax = ',num2str(Xmax)]);
end
Xmid = (Xmin+Xmax)/2;%!!!Xmid should be smaller than R but larger than H0
Hmid = R+H0-sqrt(R^2-Xmid^2);

%surface repulsive force parameters
Frep = -2*pi*R*(Eps/H0*exp(-H0/Tau)-Eps/(H0+R)*exp(-(H0+R)/Tau));%make sure the sign is
correct

%other parameters
Bondlen = Hmid/sin(theta); %stressed bond length
Bonddevlen = Bondlen-lambda; %bond deviation length.!!!Make sure this is larger than 0
Fbond = SpringC*Bonddevlen*n_b; %bond force.!!!get unit correct
```

```
Fxbond = Fbond*cos(theta);%bond force on the x direction, double check the sign with seme-analytical
%paper
Fybond = Fbond*sin(theta);%bond force in the vertical direction
Tybond = Fbond*(Xmid/tan(theta)-H0-R)*cos(theta);% torque exert on the cell.
%translational velocity
U=(shear*R*Fxrs*Tyss/2-(R+H0)*shear*Fxss*Tyrs+Fxbond*Tyrs/(6*pi*mu*R)-
Tybond*Fxrs/(8*pi*mu*R^2))/D;
%rotational velocity
Omega =-(-(R+H0)*shear/R*Fxss*Tyts-
shear*Tyss*Fxts/2+Fxbond*Tyts/(6*pi*mu*R^2)+Tybond*Fxts/(8*pi*mu*R^3))/D;
%Make sure about the sign of U, Omega, they should make sense. (U>0 and U-R*Omega also >0)
if 1<1
disp(R*Omega);
disp(U);
disp(shear*R*Fxrs*Tyss/2/D);
disp(-(R+H0)*shear*Fxss*Tyrs/D);
disp(Fxbond*Tyrs/(6*pi*mu*R)/D);
disp((-Tybond*Fxrs/(8*pi*mu*R^2))/D);
end

if 1<1
disp(Omega);
disp((R+H0)*shear/R*Fxss*Tyts/D);
disp(shear*Tyss*Fxts/2/D);
disp(-Fxbond*Tyts/(6*pi*mu*R^2)/D);
disp(-Tybond*Fxts/(8*pi*mu*R^3)/D);
end

if isreal(U)==0 || isreal(Omega)==0
   disp('Not a real number!');
end

%Following three main equations requires either some built in method or
%heuristics to solve them.
%First main equation to solve
err1_part1 = k_on*abs(U-R*Omega)*n_RT*n_LG*pi*Xmax^2-
k_r*exp(rC*Fbond/n_b/K_B/T)*n_b;
%err1_part2 = abs(k_on*abs(U-
R*Omega)*n_RT*n_LG*pi*Xmax^2)+abs(k_r*exp(rC*Fbond/n_b/K_B/T)*n_b);
%disp(['k_on*abs(U-R*Omega)*n_RT*n_LG = ',num2str(k_on*abs(U-R*Omega)*n_RT*n_LG)]);
%disp(['-k_r*exp(rC*Fbond/n_b/K_B/T)*n_b = ',num2str(-k_r*exp(rC*Fbond/n_b/K_B/T)*n_b)]);

%Second main equation to solve
err2_part1 = U*n_b-(Xmax-
Xmin)*k_r*exp(rC*Fbond/n_b/K_B/T);%U+k_on*pi*Xmax^2/n_b*n_RT*n_LG*Xmax-(Xmax-
Xmin)*k_r*exp(rC*Fbond/n_b/K_B/T);
```

```
%err2_part2 = abs(U*n_b)+(Xmax-
Xmin)*k_r*exp(rC*Fbond/n_b/K_B/T);%abs(U)+abs(k_on*pi*Xmax^2/n_b*n_RT*n_LG*Xmax)+
abs((Xmax-Xmin)*k_r*exp(rC*Fbond/n_b/K_B/T));
%disp(['U = ',num2str(U)]);
%disp(['k_on*pi*Xmax^2/n_b*n_RT*n_LG*Xmax = ',num2str(k_on/n_b*n_RT*n_LG*Xmax)]);
%disp(['-2*Xmax*k_r*exp(rC*Fbond/n_b/K_B/T) = ',num2str(-
2*Xmax*k_r*exp(rC*Fbond/n_b/K_B/T))]);
%third main equation to solve
err3_part1 = Fybond+Frep;
%err3_part2 = abs(Fybond)+abs(Frep);
%disp(['Fybond = ',num2str(Fybond)]);
%disp(['Frep = ',num2str(Frep)]);
err = (err1_part1/140)^2 + (err2_part1/14)^2 + (err3_part1/200)^2;
%disp(k_r*exp(rC*Fbond/n_b/K_B/T));
%disp(Xmax-Xmin);
%disp(k_r*exp(rC*Fbond/n_b/K_B/T)*2*Xmax);
%disp(['U-Omega*R = ',num2str(U-Omega*R)]);



%%%
```

```
r=0.1;
%bound for H0, n_b, theta
low = [0 1 pi/10];
high = [0.1 200 pi/2];

for i=1:3
   perturb_P = 1-log(iter)/log(N);
   perturb_Count = 0;
   if(unifrnd(0,1)<perturb_P)
      perturb_Count = perturb_Count+1;
      xInitial(i) = xInitial(i)+normrnd(0,r*(high(i)-low(i)));
      %reflection
      if xInitial(i)<low(i)
         xInitial(i) = 2*low(i)-xInitial(i);
         if xInitial(i)>high(i)
            xInitial(i) = high(i);
         end
      elseif xInitial(i)>high(i)
         xInitial(i) = -xInitial(i)+2*high(i);
         if xInitial<low(i)
            xInitial(i)=low(i);
         end
      end
   end
end

if perturb_Count==0
   j=unidrnd(3);
   xInitial(j) = xInitial(j)+normrnd(0,r*(high(j)-low(j)));
   %reflection
   if xInitial(j)<low(j)
      xInitial(j) = 2*low(j)-xInitial(j);
      if xInitial(j)>high(j)
         xInitial(j) = high(j);
      end
   elseif xInitial(j)>high(j)
      xInitial(j) = -xInitial(j)+2*high(j);
      if xInitial<low(j)
         xInitial(j)=low(j);
      end
   end
end
xInitial(2) = round(xInitial(2));

xNew = xInitial;

%%%%%%%%%%%%%%%%%%%%%%%%%%%%%%%%%%%%%%%%%%%%%%%%%%%%%%%%%%%%%%%%%%%%%%%%%%%%
```

```
%main executes the whole program
for i=1:5
xInitial = [0.03 20 pi/4];
[xBest,yBest,U] =DDS(xInitial,10000);
disp(xBest);
disp(yBest);
disp(U);
end
```

APPENDIX B: *IN VIVO* IMAGE PROCESSING

The thrombus growth / decay map (Figure 4.5 G-I, P-R) is plotted by superimposing adjacent microscopic pictures and find their difference. However, raw microscopic data has noise that will affect our quality of thrombus dynamic analysis. The following ImageJ macros have been used to clean up the noise and sharpen the thrombus boundaries.

```
count=30000;
for(i=0;i<1500;i++){
open("I:\\Diacovo's data\\10-13 60X HPLT\\10-13 60X HPLT"+count+".tif");
run("Make Binary");
run("Area filter...", "median=3 deriche=1 hysteresis_high=100 hysteresis_low=50");
run("Invert");
run("Close-");
run("Fill Holes");
saveAs("Tiff", "I:\\Diacovo's data\\10-13 60X HPLT\\02\\Area Outline"+count+".tif");
close();
close();
count+=1;
}
```

Once all the microscopic pictures are processed, the thrombus is shown as white and vessel wall without platelets are shown as black. These images will be further processed by Matlab code to generate thrombus decay / growth map.

```
%thrombus shape change analyser
clear all;
filenum = 20490;

count = filenum;
start = 0;
num_color=200;
total_frame = 500;
pixRes = 0.431;
fileID1 =
fopen(['I:/JohnLindsey/ThrombusData/Oct2010Data/1013.40X.HPLT2/Data/Outline4Shear/grow
',num2str(filenum),'.txt'],'w');
fileID2 =
fopen(['I:/JohnLindsey/ThrombusData/Oct2010Data/1013.40X.HPLT2/Data/Outline4Shear/off',n
um2str(filenum),'.txt'],'w');
```

```
ColorSet1=colormap(jet(num_color+1));
ColorSet2=colormap(jet(num_color+1));
I=imread(['F:\Cornell\PhD lab\project_plt_flow_thrombus\exp_data\01\Area
Outline',num2str(count),'.tif']);
Bound = size(I); %size of the image

grow = zeros(Bound(1),Bound(2));
off = zeros(Bound(1),Bound(2));
plt1 = zeros(Bound(1),Bound(2),3);
plt2 = zeros(Bound(1),Bound(2),3);

for n=1:total_frame - start

   count = count + 1;
   J=imread(['F:\Cornell\PhD lab\project_plt_flow_thrombus\exp_data\01\Area
Outline',num2str(count),'.tif']);

   for x=1:Bound(1)
      for y=1:Bound(2)
         if I(x,y)==255 && J(x,y)==0
            grow(Bound(1)+1-x,y)=grow(Bound(1)+1-x,y)+1; %turn image upside down
         elseif I(x,y)==0 && J(x,y)==255
            off(Bound(1)+1-x,y)=off(Bound(1)+1-x,y)+1;
         end
      end
   end

end

maxgrow = max(max(grow));
maxoff = max(max(off));

for x=1:Bound(1)
   for y=1:Bound(2)
      if grow(x,y)~=0 && y>140 && y<420 && x>40 && x<200    %x is line number, y is column
number!
         fprintf(fileID1,'%6.2f %6.2f %6.2f\n', y*pixRes, (Bound(1)-x+1)*pixRes,
grow(x,y));  %reverse the "x" back
      end
      if off(x,y)~=0 && y>140 && y<420 && x>40 && x<200
         fprintf(fileID2,'%6.2f %6.2f %6.2f\n', y*pixRes, (Bound(1)-x+1)*pixRes, off(x,y));
      end
      plt1(x,y,:)= ColorSet1(round(grow(x,y)/maxgrow*num_color)+1,:);
      plt2(x,y,:)= ColorSet2(round(off(x,y)/maxoff*num_color)+1,:);
   end
end
imshow(plt2);
```

```
%imwrite(plt1,'F:\Cornell\PhD lab\project_plt_flow_thrombus\exp_data\01\grow');
fclose(fileID1);
fclose(fileID2);
axis on;
axis([150 420 40 200]);
h=gca;
set(h,'XTick',[80/pixRes,100/pixRes,120/pixRes,140/pixRes,160/pixRes,180/pixRes,],'XTickLabel',
[80,100,120,140,160,180]);
set(h,'YTick',[20/pixRes,40/pixRes,60/pixRes,80/pixRes],'YTickLabel',[80, 60, 40, 20]);
xlabel('x (\mum)');
ylabel('y (\mum)');
colorbar;
```

The main idea behind this code is that, we pick up one frame and set it as a reference frame. Then for each of the following frames, we compare the color for each pixel. If it was shown as white in the reference frame but black in the later frames, it is marked as a decaying area. If it was shown as black in the reference frame but white in the later frames, it is marked as a growth area. The degree of decay or growth (color scale) for each pixel is determined by the number of later frames that shows as decay / growth at that pixel. Note that the pixel scale is ultimately changed back to the dimensional length scale.